

SPHERE/ZIMPOL high resolution polarimetric imager

I. System overview, PSF parameters, coronagraphy, and polarimetry^{*}

H. M. Schmid¹, A. Bazzon¹, R. Roelfsema², D. Mouillet^{3,4}, J. Milli⁵, F. Menard^{3,4}, D. Gisler^{6,7}, S. Hunziker¹, J. Pragt², C. Dominik⁸, A. Boccaletti⁹, C. Ginski¹⁰, L. Abe¹¹, S. Antonucci¹², H. Avenhaus^{13,1}, A. Baruffolo¹⁴, P. Baudoz⁹, J.L. Beuzit¹⁵, M. Carbillet¹¹, G. Chauvin^{3,16}, R. Claudi¹⁴, A. Costille¹⁵, J.-B. Daban¹¹, M. de Haan², S. Desidera¹⁴, K. Dohlen¹⁵, M. Downing¹⁷, E. Elswijk², N. Engler¹, M. Feldt¹³, T. Fusco^{15,18}, J. H. Girard⁵, R. Gratton¹⁴, H. Hanenburg², Th. Henning¹³, N. Hubin¹⁷, F. Joos¹, M. Kasper¹⁷, C. U. Keller¹⁰, M. Langlois^{19,15}, E. Lagarde¹¹, P. Martinez¹¹, E. Mulder², A. Pavlov¹³, L. Podio²⁰, P. Puget³, S. P. Quanz¹, F. Rigal², B. Salasnich¹⁴, J.-F. Sauvage^{15,18}, M. Schuil², R. Siebenmorgen¹⁷, E. Sissa¹⁴, F. Snik¹⁰, M. Suarez¹⁷, Ch. Thalmann¹, M. Turatto¹⁴, S. Udry²¹, A. van Duin², R. G. van Holstein¹⁰, A. Vigan¹⁵, and F. Wildi²¹

(Affiliations can be found after the references)

Received 12 July 2018 / Accepted 3 August 2018

ABSTRACT

Context. The SPHERE “planet finder” is an extreme adaptive optics (AO) instrument for high resolution and high contrast observations at the Very Large Telescope (VLT). We describe the Zurich Imaging Polarimeter (ZIMPOL), the visual focal plane subsystem of SPHERE, which pushes the limits of current AO systems to shorter wavelengths, higher spatial resolution, and much improved polarimetric performance.

Aims. We present a detailed characterization of SPHERE/ZIMPOL which should be useful for an optimal planning of observations and for improving the data reduction and calibration. We aim to provide new benchmarks for the performance of high contrast instruments, in particular for polarimetric differential imaging.

Methods. We have analyzed SPHERE/ZIMPOL point spread functions (PSFs) and measure the normalized peak surface brightness, the encircled energy, and the full width half maximum (FWHM) for different wavelengths, atmospheric conditions, star brightness, and instrument modes. Coronagraphic images are described and the peak flux attenuation and the off-axis flux transmission are determined. Simultaneous images of the coronagraphic focal plane and the pupil plane are analyzed and the suppression of the diffraction rings by the pupil stop is investigated. We compared the performance at small separation for different coronagraphs with tests for the binary α Hyi with a separation of 92 mas and a contrast of $\Delta m \approx 6^m$. For the polarimetric mode we made the instrument calibrations using zero polarization and high polarization standard stars and here we give a recipe for the absolute calibration of polarimetric data. The data show small (< 1 mas) but disturbing differential polarimetric beam shifts, which can be explained as Goos-Hänchen shifts from the inclined mirrors, and we discuss how to correct this effect. The polarimetric sensitivity is investigated with non-coronagraphic and deep, coronagraphic observations of the dust scattering around the symbiotic Mira variable R Aqr.

Results. SPHERE/ZIMPOL reaches routinely an angular resolution (FWHM) of 22–28 mas, and a normalized peak surface brightness of $SB_0 - m_{\text{star}} \approx -6.5^m \text{ arcsec}^{-2}$ for the V-, R- and I-band. The AO performance is worse for mediocre $\geq 1.0''$ seeing conditions, faint stars $m_R \geq 9^m$, or in the presence of the “low wind” effect (telescope seeing). The coronagraphs are effective in attenuating the PSF peak by factors of > 100 , and the suppression of the diffracted light improves the contrast performance by a factor of approximately two in the separation range $0.06'' - 0.20''$. The polarimetric sensitivity is $\Delta p < 0.01\%$ and the polarization zero point can be calibrated to better than $\Delta p \approx 0.1\%$. The contrast limits for differential polarimetric imaging for the 400 s I-band data of R Aqr at a separation of $\rho = 0.86''$ are for the surface brightness contrast $SB_{\text{pol}}(\rho) - m_{\text{star}} \approx 8^m \text{ arcsec}^{-2}$ and for the point source contrast $m_{\text{pol}}(\rho) - m_{\text{star}} \approx 15^m$ and much lower limits are achievable with deeper observations.

Conclusions. SPHERE/ZIMPOL achieves imaging performances in the visual range with unprecedented characteristics, in particular very high spatial resolution and very high polarimetric contrast. This instrument opens up many new research opportunities for the detailed investigation of circumstellar dust, in scattered and therefore polarized light, for the investigation of faint companions, and for the mapping of circumstellar H α emission.

Key words. instrumentation: adaptive optics – instrumentation: high angular resolution – instrumentation: polarimeters – instrumentation: detectors – planetary systems – circumstellar matter

1. Introduction

The SPHERE “planet finder” instrument has been successfully installed and commissioned in 2014 at the VLT. The main task of this instrument is the search and investigation of extra-solar planets around bright stars $m_R \lesssim 10^m$. Therefore SPHERE is optimized for high contrast and diffraction limited resolution observation in the near-IR and the visual spectral region using

an extreme adaptive optics (AO) system, stellar coronagraphs, and three focal plane instruments for differential imaging. General technical descriptions of the instrument are given in Beuzit et al. (2008), Kasper et al. (2012), and the SPHERE user manual and related technical websites¹ of the European Southern Observatory (ESO). SPHERE is a very powerful facility instrument which provides a broad suite of sophisticated instrument

^{*} Based on observations collected at La Silla and Paranal Observatories, ESO (Chile), Program ID: 60.A-9249 and 60.A-9255.

¹ www.eso.org/sci/facilities/paranal/instruments/sphere

modes for the very demanding investigation of extra-solar planetary systems. Essentially all of these modes also provide unique observing opportunities for the study of the immediate circumstellar environment of bright stars. Technical results about the on-sky performance of the SPHERE instrument are given in [Dohlen et al. \(2016\)](#), and on-sky results for the AO-system are described in [Fusco et al. \(2016\)](#) and [Milli et al. \(2017\)](#). A series of first SPHERE science papers demonstrates the performance of various observing modes of this instrument (e.g. [Vigan et al. 2016](#); [Maire et al. 2016a](#); [Zurlo et al. 2016](#); [Bonnefoy et al. 2016](#)). However, the SPHERE instrument is complex and therefore it is appropriate to give more specific descriptions on individual subsystems and this is the first of a few technical papers for the visual focal plane instrument ZIMPOL.

ZIMPOL, the Zurich Imaging Polarimeter, works in the spectral range from 500 nm to 900 nm and provides, thanks to the SPHERE AO system and visual coronagraph, high resolution ($\approx 20\text{--}30$ mas) and high contrast imaging and imaging polarimetry for the immediate surroundings ($\rho < 4$ arcsec) of bright stars. SPHERE/ZIMPOL includes a very innovative concept for high performance imaging polarimetry using a fast modulation – demodulation technique and it is tuned for very high contrast polarimetry of reflected light from planetary system. Beside this it can also be used as a high contrast imager offering angular differential imaging and simultaneous spectral differential imaging.

Previous publications on ZIMPOL describe the science goal ([Schmid et al. 2006a](#)), the expected performance ([Thalmann et al. 2008](#)), and give reports about the concept of ZIMPOL ([Gisler et al. 2004](#); [Joos 2007](#); [de Juan Ovelar et al. 2012](#)), the instrument design and component tests ([Roelfsema et al. 2010, 2011](#); [Pragt et al. 2012](#); [Bazzon et al. 2012](#); [Schmid et al. 2012](#)) and system testing ([Roelfsema et al. 2014, 2016](#)). Some early science results based on SPHERE/ZIMPOL observations are given in [Thalmann et al. \(2015\)](#), [Garufi et al. \(2016\)](#), [Kervella et al. \(2016\)](#), [Stolker et al. \(2016\)](#), [Khouri et al. \(2016\)](#), [Avenhaus et al. \(2017\)](#), [Ohnaka et al. \(2017a\)](#) and [Engler et al. \(2017\)](#). [Schmid et al. \(2017\)](#) also gives technical information about H α imaging and the flux calibration of ZIMPOL data.

Many technical aspects must be considered for carrying out well optimized observations and calibrations with an instrument like ZIMPOL, which combines diffraction-limited imaging using extreme adaptive optics, coronagraphy, and differential techniques like polarimetry, or angular and spectral differential imaging. It is not possible to cover all these topics in detail in one paper and therefore we focus on a basic technical description and on aspects which are special to SPHERE/ZIMPOL when compared to other high contrast instruments. This should serve as a starting point for potential SPHERE/ZIMPOL users to carry out well optimized observations and data analyzes for exploiting the full potential of this instrument. We plan that subsequent papers will address other aspects of SPHERE/ZIMPOL, such as astrometry, precision photometry, a detailed technical assessment of the high performance polarimetry mode and more.

This paper is organized as follows. The next section gives a brief overview on the SPHERE common path and a detailed description of the ZIMPOL subsystem, imaging properties, the ZIMPOL polarimetry, the detectors and detector calibrations, and the filters. Section 3 characterizes the “typical” point spread functions (PSFs) and describes special cases, like faint stars, poor atmospheric conditions, or particular instrumental effects. The topic of Sect. 4 is the SPHERE visual coronagraph and the comparison of coronagraphic test measurements taken with different focal plane masks. SPHERE/ZIMPOL polarimetry is described in detail in Sect. 5 including the concept for the

control of the polarimetric signal and the correction of the measurements based on calibrations of the telescope, the instrument, and the detectors. Further we discuss the polarimetric differential beamshift, a disturbing effect which is new for astronomical optics and which was not anticipated in the design of this instrument. Then, we illustrate the very good polarimetric performance of ZIMPOL with test observations of the system R Aqr. We conclude in Sect. 6 with a summary of the most outstanding technical properties of SPHERE/ZIMPOL and an outline of the new research opportunities offered by this instrument.

2. The visual channel of SPHERE

The SPHERE visual channel covers the wavelength range from 500 to 900 nm and provides observational modes for imaging, spectral differential imaging, angular differential imaging and polarimetric differential imaging. The next subsection gives a brief overview of the SPHERE common path while the visual focal plane instrument ZIMPOL is described in detail in the following subsections.

2.1. Common path and infrastructure – CPI

Figure 1 gives a simplified block diagram of those parts of the SPHERE main bench or “common path and infrastructure” (CPI) system which are relevant for visual observations. Table 1 lists the components along the beam indicating the rotating, insertable, and exchangeable components and those which are only in the beam for polarimetry (see also the colors in Fig. 1).

The heart of the SPHERE instrument is the extreme adaptive optics (AO) system, which corrects for the variable wave-front distortions introduced by the rapidly changing Earth’s atmosphere. At the same time the AO corrects also for aberrations introduced by the telescope and the SPHERE instrument ([Fusco et al. 2014](#); [Sauvage et al. 2016b](#)). The AO system needs a bright natural guide star in the center of the science field as wave front probe, preferentially with a brightness $m_R \lesssim 10^m$. The AO performance depends strongly on the atmospheric conditions and the guide star brightness ([Sauvage et al. 2016b](#)) as described in Sect. 3. Essential components of the AO system are the Shack-Hartmann wave front sensor (WFS), which measures the wave front distortions, the fast high-order deformable mirror (DM), the fast tip-tilt mirror (TTM), and the pupil tip-tilt mirror (PTTM) which correct for the measured distortions.

The CPI includes in addition an image derotator (DROT) which can be used in three different rotation modes: (i) to stabilize the sky image on the detector, (ii) to fix the orientation of the telescope pupil, or (iii) to keep the instrument polarization stabilized. The visual-infrared beam splitter (vi.BS) transmits long wavelengths $\lambda > 950$ nm to the IR science channel and reflects the short wavelengths $\lambda < 950$ nm to the wave front sensor arm and ZIMPOL. The IR channel includes the IR-coronagraph ([Boccaletti et al. 2008](#)) and two focal plane instruments, the infrared double beam imager and spectrograph IRDIS ([Dohlen et al. 2008](#); [Vigan et al. 2014](#)) and the integral field spectrograph IFS ([Claudi et al. 2008](#)).

The visual beam is further split after the visual atmospheric dispersion corrector (ADC) by one of two exchangeable beam splitters (zw.BS) which reflect part of the light to the wave front sensor arm and transmits the other part to the visual coronagraph and ZIMPOL. There is a gray beam-splitter transmitting about 79% of the light to ZIMPOL and 21% to the WFS, and a dichroic beam-splitter transmitting the wavelengths 600–680 nm to ZIMPOL and reflecting the other wavelengths within the

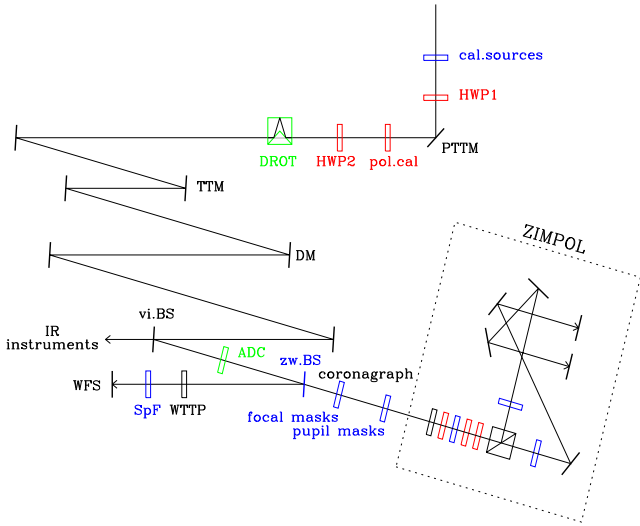


Fig. 1. Block diagram of the SPHERE common path (CPI) up to the beam splitter vi.BS and the SPHERE visual channel. The blue color indicates exchangeable components, green are rotating components, and red components are only inserted for polarimetry. The ZIMPOL box is shown in detail in Fig. 2.

500–950 nm range, or about 80% of the light depending on the color of the central star, to the WFS.

The wave front sensor arm includes a tip-tilt plate (WTTP) for the fine centering of the central AO guide star on a coronagraphic focal plane mask, or another position in the field of view within about $0.6''$ from the optical axis. In front of the WFS one can also select between a large, medium or small field mask as spatial filter to optimize the AO performance (Fusco et al. 2016).

Furthermore, the CPI includes two insertable and rotatable half-wave plates (HWP1 and HWP2) and polarimetric calibration components (pol.cal) for polarimetric imaging with ZIMPOL as will be described later in Sect. 5.2.

Different calibration light sources and components can be inserted inside SPHERE at the VLT-Nasmyth focus (Wildi et al. 2009, 2010). For the visual science channel there is a flat field source with a continuous spectrum for detector flat-fielding. This source can be combined with a mask with a grid of holes for measurements of the SPHERE/ZIMPOL image scale and distortions. In addition, there is a point source with a continuous spectrum for measurements and checks of the instrument alignment. The brightness of the sources can be adjusted with neutral density filters also located in the calibration unit.

2.2. The Zurich imaging polarimeter

A block diagram for the Zurich IMaging POLarimeter (ZIMPOL) is shown in Fig. 2 and a list of all components is given in Table 2. ZIMPOL is a two arm imager with a polarization beam splitter (BS). The ZIMPOL common path consists of a collimated beam section with an intermediate pupil just before ZIMPOL, at the position of the coronagraphic pupil mask wheel. This pupil has a diameter of 6 mm and it defines the interface between CPI and ZIMPOL. Polarimetric components can be inserted and removed in the ZIMPOL common path without changing the image focus. The following subsections describe the imaging properties of this setup, the ZIMPOL polarimetric principle, the polarimetric components, the special detector properties, and the ZIMPOL filters. Previous publications on ZIMPOL give more information about the

Table 1. Optical components of the VLT and SPHERE CPI visual path.

Abbr.	Name	r	i	e	p	Comment
<i>VLT telescope</i>						
M1,M2	Telescope	mir-	r			alt.-az. orientation
M3	Telescope mirror		r			Strong pol. effects
<i>CPI common path</i>						
–	Calibration sources		i	e		Point and flat field sources, hole grid
HWP1	Half-wave plate 1	r	i	p		Rotates M3 pol.
PTTM	Pupil tip-tilt mirror					AO, compensates M3 polarization
–	pol. calibration components		i	e	p	pol. characterization
HWP2	Half-wave plate 2	r	i	p		Polarization control and switch
DROT	Image derotator	r				Rotates image, strong pol. effects
TTM	Tip tilt mirror					AO
DM	Deformable mirror					AO
vi.BS	Beam splitter					Visual-infrared
<i>CPI visual common path</i>						
ADC	Atmospheric dispersion corrector	r				For visual
zw.BS	ZIMPOL-WFS beam splitter		e			Gray or dichroic BS
<i>Wave front sensor (WFS) arm</i>						
WTTP	WFS tip-tilt plate					Source positioning
SpF	WFS spatial filter		e			AO tuning
WFS	WFS-detector					AO tuning
<i>CPI visual coronagraph</i>						
–	Focal plane masks		e			Exchange wheel
–	Pupil masks		e			Exchange wheel

Notes. This incomplete list gives all important components for visual science observations. “Short” are abbreviations as used in this paper and Cols. 3–7 indicate whether the components are rotating (r), insertable (i), exchangeable (e), or/and only inserted for visual polarimetry (p).

opto-mechanical design (Roelfsema et al. 2010), optical alignment procedures (Pragt et al. 2012), test results at various phases of the project (Roelfsema et al. 2011, 2014, 2016), the detectors (Schmid et al. 2012), and the polarimetric calibration concept (Bazzon et al. 2012).

2.2.1. ZIMPOL imaging properties

The ZIMPOL subsystem is optimized for polarimetric imaging but provides at the same time also very good imaging capabilities. In this section we describe the imaging properties of ZIMPOL, which apply for imaging and polarimetric imaging. For polarimetry, additional components are inserted in CPI and ZIMPOL and different detector modes are used, which reduce the overall instrument throughput by about a factor 0.85 with respect to non-polarimetric imaging.

For imaging the three red polarimetric components in the ZIMPOL block diagram (Fig. 2) are removed from the beam and there remains only the shutter and filter wheel FW0 in the common path. The polarization beam splitter creates then the two camera arms 1 and 2, each equipped with its own filter

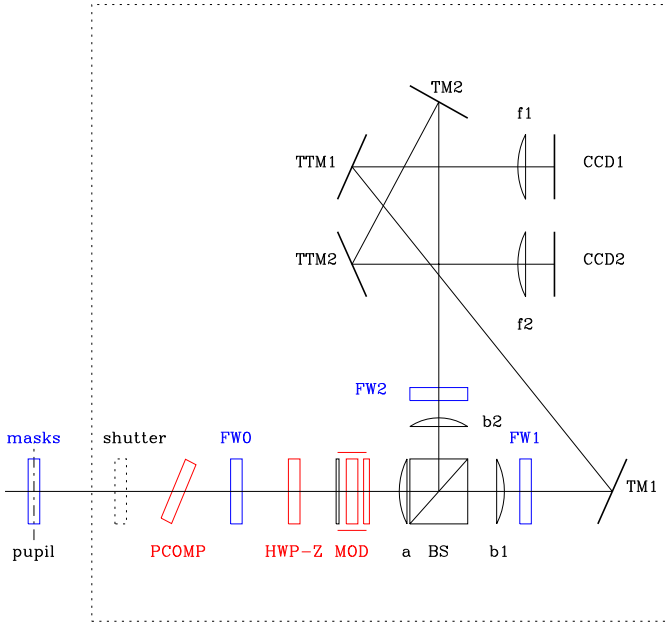


Fig. 2. Block diagram for ZIMPOL with exchangeable components plotted in blue, while red components are only inserted for polarimetry.

wheel FW1 or FW2, own detectors CCD1 or CCD2, own imaging optics (lenses b1,f1 or b2,f2), and own movable folding mirrors TM1,TTM1 or TM2,TTM2 for dithering and the selection of the detector field of view.

The beam-splitter includes on the entrance side lens “a”, a first common component of the camera optics. It is glued onto the beam splitter in order to avoid back-reflections (and ghost images) from the surfaces of the beam-splitter. Lens “a” produces together with “b1” or “b2” the converging beams with an f -ratio of 221 producing an image scale of 0.12 arcsec/mm or a pixel scale of about 3.6 mas pix^{-1} on the CCD detectors. The detectors have an active area of about $3.0 \times 3.0 \text{ cm}^2$ or about 1000×1000 pixels covering a detector field of view of about $3.6'' \times 3.6''$. There are optical image distortions and the dominant effect is an anamorphism which originates from the SPHERE common path optics located after the image derotator. This stretches for ZIMPOL the image scale expressed as mas pix^{-1} by a factor of about 1.006 in the detector row or x -direction, which is perpendicular to the CCD charge shifting direction. In field stabilized observations without field angle offset a square pixel covers an area, which is slightly elongated in east-west direction when projected onto the sky, like for the IRDIS and IFS near-IR instruments (see also Maire et al. 2016b). Detailed measurements of these distortions and the derivation of an accurate astrometric calibration for ZIMPOL will be described in Paper II (Ginski et al., in prep.).

ZIMPOL allows imaging in two channels using either a filter in the common path wheel FW0, or combining filters from the wheels FW1 in arm 1 and FW2 in arm 2 (see Sect. 2.4). Differential spectral imaging can be achieved by using different filters in FW1 and FW2. The filters in FW1 and FW2 can be combined with a neutral density filter located in FW0 in order to avoid detector saturation of bright sources.

Off-axis fields. The SPHERE/ZIMPOL optical field of view has a diameter of $8''$ (6.67 cm) and is about four times larger than the detector field of view. This $8''$ -field is defined by the wide field “WF” focal plane masks in the coronagraph. To access the whole field of view offered by SPHERE/ZIMPOL, it is possi-

Table 2. List of all components in ZIMPOL.

Abbr.	Name	r i e p	Comment
<i>ZIMPOL common path</i>			
–	Shutter		Cut transfer smear
PCOMP	Polarization compensator	r i p	Compensate DROT polarization
FW0	Filter wheel 0	e	Color filters, NDs, pol. calibration
HWPZ	Half wave plate ZIMPOL	r i p	Rotate polarization, calibrations
MOD	Modulator (FLC) and 0-HWP	i p	pol. modulation, blocking filter (BF)
BS	Polarization beam splitter		With camera lens “a”
<i>ZIMPOL arms 1 and 2</i>			
FW1/2	Filter wheels 1,2	e	Color filters, pupil lens in FW2
b1/2	Camera lenses “b”		
TM1/2	Tip-mirrors 1,2		Mask illumination
TTM1/2	Tip-tilt mirrors 1,2		Dithering, offsets
f1/2	Field lenses 1,2		Mask illumination
CCD1/2	Detectors 1,2		pol. demodulation

Notes. “Short” gives abbreviations as used in this paper. Columns 3–6 indicate whether the components are rotating (r), insertable (i), exchangeable (e), or/and only inserted for visual polarimetry (p).

ble to move the image on the detector with the tip-tilt mirrors TTM1 or TTM2 and tip mirrors TM1 or TM2 in the two arms. Field lenses f1 or f2 and tip-mirrors are required to achieve, also for off-axis fields, a perpendicular illumination of the cylindrical micro-lenses and stripe masks in front of the special ZIMPOL detectors (see Sect. 2.3). To simplify the operation of ZIMPOL the instrument software allows only identical dithering and field offsets in arm 1 and arm 2. Optimized mirror settings have been pre-defined and tested for observations of the field center and eight off-axis fields (OAF1 – OAF8). The selectable off-axis fields are shown in Fig. 3 and approximate values for the offsets are given in Table 3. The off-axis fields avoid the central star and the surrounding $\rho \lesssim 0.8''$ strong light halo. This enables long exposures with broad-band filters in the off-axis fields without saturation by light from the typically much brighter central star.

The sky region shown in Fig. 3 is the SPHERE astrometric reference field 47 Tuc = NGC 104 (Maire et al. 2016b). This field is centered on the bright asymptotic giant branch (AGB) star 2MASS J00235767 – 7205296, which is also star “MMS12” in the mid-IR study of Momany et al. (2012). Also “MMS36”, the southern star of the pair in the SE and the star “MMS11” (also 2MASS J00235692 – 7205325) just outside the field in the SW are bright AGB stars. The northern star of the SE pair is the well studied post-AGB star Cl* NGC 104 BS (BS for bright star) with spectral type B8 III, the brightest star in 47 Tuc in the V -band $V = 10.7^m$ and even more prominent in the near and far UV (e.g. Dixon et al. 1995; Schiavon et al. 2012). The catalog of McLaughlin et al. (2006) and a study of Bellini (priv. commun., see also Bellini et al. 2014) provide accurate HST astrometry of most stars visible in Fig. 3 and they can be used for the

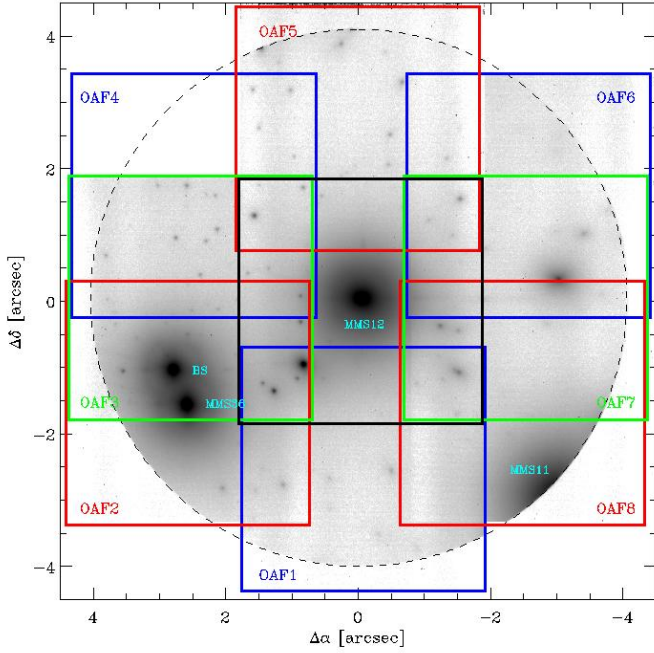


Fig. 3. Full ZIMPOL instrument field for the astrometric field 47 Tuc. The central detector field is plotted in black, while colors are used for the 8 pre-defined off-axis fields OAF1-OAF8. The off-axis fields have been shifted slightly (red to the left, blue to the right, and green up) for better visibility. No data are available for OAF4 because of an observational error.

astrometric calibrations for the central field, but also the off-axis fields of ZIMPOL.

The ZIMPOL image rotation modes. The SPHERE bench is fixed to the VLT Nasmyth platform A of UT3 and the sky image rotates in the telescope focus (“tf”) or the entrance focus of the instrument like

$$\theta_{\text{tf}}(t) = \theta_{\text{para}}(t) + a(t) \quad (1)$$

where θ_{para} is the parallactic angle and a the telescope altitude. The field orientation on the detector is defined by the image rotation introduced by DROT.

For the ZIMPOL imaging mode one can choose between field stabilized and pupil stabilized observations. In the first case the sky image is fixed and N_{CCD} , the north direction on the CCD-detector after applying image flips in the data preprocessing, is given by

$$N_{\text{CCD}} = \theta_0 - \delta\theta, \quad (2)$$

where the angle N_{CCD} is measured from the vertical or y-direction in counter-clockwise direction. There is a small rotational offset $\theta_0 \approx 2^\circ$, which is not exactly identical for CCD1 and CCD2, and which can be accurately determined with astrometric calibrations (Ginsky et al., in prep.). The term $\delta\theta$ stands for the user defined field orientation angle offset (see Fig. 22).

In pupil stabilized mode the telescope pupil is stabilized on the detector and the field rotates in step with the parallactic angle. This may introduce image smearing for long integrations, if the rotation during t_{DIT} is too large.

For polarimetric imaging one can choose between static derotator mode, called P1, and field stabilized mode P2. In P1 mode the derotator is fixed and the field rotates on the CCD as

$$N_{\text{CCD}}(t) = \theta_{\text{para}}(t) + a(t) + \theta_0 \quad (3)$$

Table 3. Approximate offsets for the centers of the off-axis fields (OAF).

Field	Offset in pixels		Offset in arcsec		On sky
	Δx	Δy	$\Delta \alpha$	$\Delta \delta$	
Center	0	0	0	0	
OAF1	0	-715	0.00''	-2.57''	S
OAF2	-715	-428	+2.57''	-1.54''	E-SE
OAF3	-715	0	+2.57''	0.00''	E
OAF4	-715	+428	+2.57''	+1.54''	E-NE
OAF5	0	+715	0.00''	+2.57''	N
OAF6	+715	+428	-2.57''	+1.54''	W-NW
OAF7	+715	0	-2.57''	0.00''	W
OAF8	+715	-428	-2.57''	-1.54''	W-SW

Notes. Pixel offsets Δx and Δy refer to preprocessed images with image flips applied to cam1 and cam2 images. Columns 4–6 give the on-sky offsets for the right ascension $\Delta \alpha$ and declination $\Delta \delta$ for field stabilized observations taken without field position angle offset as shown in Fig. 3. The actual offsets deviate by about ± 3 pixels or $\pm 0.01''$ from the given design values.

but also the telescope pupil moves with $a(t)$. The advantage of this mode is an accurate calibration of the telescope polarization, because derotator and all following components (except for the atmospheric dispersion corrector) are in a fixed orientation. The rotation law for P2 is identical to the field stabilized mode in imaging.

2.2.2. The ZIMPOL principle

Strong, variable speckles from the bright star are the main problem for high contrast imaging from the ground. ZIMPOL is optimized for high precision imaging polarimetry under such conditions because the speckle noise can be strongly reduced with an imaging polarimeter based on a fast modulation-demodulation technique. A polarization modulator and a polarizer (or a polarization beam splitter) convert the fractional polarization signal into a fractional modulation of the intensity signal, which is then measured by a masked, demodulating imaging detector as shown schematically in Fig. 4.

A polarimetric modulation with a frequency of about 1 kHz is sufficient to “freeze” the speckle variations introduced by the atmospheric turbulence in the differential polarimetric measurement. This requirement is realized in SPHERE/ZIMPOL with a modulation using a ferro-electric liquid crystal (FLC) retarder and CCD array detectors for the demodulation. On the CCD “every second row” is masked so that photo-charges created in the open rows during one half of the modulation cycle are shifted for the second half of the cycle to the next masked row, which is used as temporary buffer. The charge shifting is synchronized with the modulator switching, so that two images, the “even-row” and the “odd-row” subframes, with opposite linear polarization modes I_{\perp} and I_{\parallel} are built up. Photo-electrons can be collected during hundreds or thousands of modulation cycles before the detector is read out. The difference of the two images is proportional to the polarization flux and the sum proportional to the intensity

$$P^Z = I_{\perp} - I_{\parallel} \quad \text{and} \quad I = I_{\perp} + I_{\parallel}. \quad (4)$$

Important advantages of the ZIMPOL technique are:

- the images for opposite polarization states are created essentially simultaneously because the modulation is faster than the speckle variations and instrument drifts,

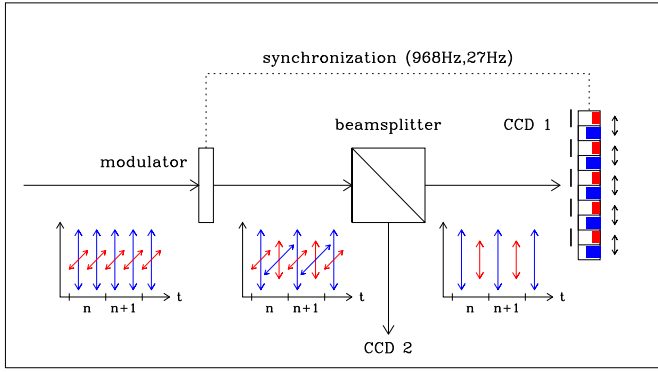


Fig. 4. ZIMPOL principle: The modulator switches in one cycle n the polarization direction between I_{\perp} and I_{\parallel} . The polarization beam splitter selects for each channel only one polarization mode so that a polarization signal is converted into an intensity modulation. The masked CCDs demodulate the signal with charge-shifting, which is synchronized with the modulator.

- allows a fast modulation without high frame rates so that the read-out noise is low,
- both images are recorded with the same pixels, reducing significantly flatfielding requirements and alignment issues for the difference image,
- differential aberrations between the two images with opposite polarization are very small.

ZIMPOL was initially developed for solar applications (Povel et al. 1990; Povel 1995) and it proved to be an extremely sensitive technique for polarimetric imaging of the Sun (e.g. Stenflo 1996; Stenflo & Keller 1997; Gandorfer & Povel 1997). For SPHERE, the ZIMPOL concept was adapted for a higher transmission, longer integration times and broad band capabilities with the development of a new type of achromatic polarization modulator (Gisler et al. 2003, 2004), a CCD detector with more pixels, and a stripe mask equipped with a cylindrical micro-lens array to reduce the photon loss on the stripe mask (Schmid et al. 2012).

ZIMPOL is a single beam technique which could also be used with a polarizer, but then 50% of the light is lost. With a polarization beam splitter all light is used and the same polarimetric information is encoded in both channels. The two channels can be combined but they can also be used as separate but simultaneous measurements, for example by using different filters in the two arms.

2.2.3. ZIMPOL polarimetric setup

This section describes the properties of the polarimetric components in ZIMPOL while Sect. 5.2 explains how they are used to obtain well calibrated polarization data. ZIMPOL has three polarimetric components, the ferro-electric liquid crystal (FLC) modulator assembly, the polarization compensator (PCOMP) and a half-wave plate (HWPZ) which are only inserted for polarimetric observations (indicated in red in Fig. 2). Further polarimetric components are the polarization beam splitter and the polarimetric calibration components in FW0. The other key elements for polarimetry are the demodulating CCD detectors described in the next section.

PCOMP and HWPZ. The polarization compensator plate (PCOMP) is required to reduce the instrument polarization of about 2–3% introduced by the DROT (derotator) mirrors in CPI. A low instrument polarization is important for a good charge trap

compensation and for reducing the impact of non-linearity of the detectors on the achievable polarization sensitivity. PCOMP is an uncoated, inclined glass plate (fused silica $n = 1.45\text{--}1.46$), where the two surfaces deflect more I_{\perp} than I_{\parallel} so that a linear polarization of the incoming beam $p^i = (I_{\perp}^i - I_{\parallel}^i)/(I_{\perp}^i + I_{\parallel}^i)$ can be reduced for the transmitted beam $p^t = p^i - \Delta p$, if the inclined plate has a perpendicular orientation $\theta_{\text{PCOMP}} = \theta_{\text{pol}} + 90^\circ$. The polarimetric compensation depends on the inclination angle of the plate, according to the Fresnel formulae (e.g. Born & Wolf 1999; Collett 1992). The PCOMP orientation rotates in step with DROT and the inclination can be adjusted. In the commissioning a good compensation for the entire wavelength range and all DROT orientations was found for $i_{\text{PCOMP}} = 25^\circ$. For this angle the two surfaces deflect together about $I_{\perp}^t = 0.089I_{\perp}^i$ and $I_{\parallel}^t = 0.051I_{\parallel}^i$. For small polarization $p^i < 5\%$ the total transmission is $I^t \approx 0.93I^i$ and the polarization in the transmitted beam is reduced according to $p^t \approx p^i - 2.0\%$

ZIMPOL has two DROT-modes for polarimetry, P1-mode with fixed DROT and a rotating sky field on the detector, and P2-mode with rotating DROT and fixed field on the detector. In P1-mode, DROT and PCOMP are both fixed and in P2 they rotate synchronously. In P2-mode an additional achromatic half-wave plate (HWPZ) must be introduced, to rotate the polarization to be measured, which passes the DROT as I_{\perp} and I_{\parallel} , into the I_{\perp} and I_{\parallel} orientation of the polarimeter. For this, also HWPZ must be on a rotational stage and its orientation is $\theta_{\text{HWPZ}} = \theta_{\text{DROT}}/2$.

ZIMPOL measures the linear polarization $P^Z = I_{\perp} - I_{\parallel}$ perpendicular and parallel to the SPHERE bench only. HWP2 and DROT in the common path and HWPZ within ZIMPOL are responsible for the correct rotation of the sky polarization into the ZIMPOL system. The achromatic half-wave plates are made of quartz and MgF₂ retarders in optical contact².

The FLC modulator. The ferro-electric liquid crystal (FLC) polarization modulator is a key component in ZIMPOL. An FLC retarder is a zero order half wave plate where the orientation of the optical axis can be switched by about 45° by changing the sign of the applied voltage through the FLC layer. A fast switch time in the range of $50 \mu\text{s}$ is required to achieve a good efficiency for a modulation cycle frequency on the order 1 kHz. The selected FLC retarder achieves this fast switching only when the operation temperature is in the range $20^\circ\text{--}30^\circ$ Celsius. Also the switching angle depends slightly on temperature (Gandorfer 1999; Gisler et al. 2003). Because the FLC retarder has to be warmer than the rest of the SPHERE instrument ($0^\circ\text{--}15^\circ\text{C}$) it is thermally insulated in a vacuum housing to avoid air turbulence in the instrument.

The FLC retarder is a half wave plate only at the nominal wavelength λ_0 because the retardance varies roughly like $1/\lambda$ and therefore the modulation efficiency depends strongly on wavelength. In order to cover the broad wavelength range of ZIMPOL, a combined design with a static zero order half wave plate (0-HWP) is used which reduces significantly the chromatic dependencies of the modulator (Gisler et al. 2004; Bazzon et al. 2012). The zero-order half wave plate is placed on the exit window of the FLC modulator housing. The entrance window includes an out-of-band blocking filter as described in Sect. 2.4.

Polarization beam splitter. The polarization beam splitter is a cube made of two 90° -prisms of Flint-glass in optical contact. The transmitted beam consists of more than 99.9% of I_{\parallel} , while the reflected beam consists of about 97% of I_{\perp} and 3% of I_{\parallel} light. The polarimetric efficiency of the ZIMPOL arm 2 is therefore about $\epsilon_{\text{arm2}} = (I_{\perp} - I_{\parallel})/(I_{\perp} + I_{\parallel}) \approx 94\%$ or about 6% lower than

² From Bernhard Halle Nachfl.

for arm 1 while the total intensity throughput is 6% higher than for arm 1.

The polarization beam splitter has a lens “a” glued to the first surface. Together with lenses “b1” and “b2” in the two arms they form the camera lenses. Component “a” is added to the beam-splitter to reduce the impact of back-reflections from the flat beam-splitter surfaces into the collimated beam where subsequent reflections could produce disturbing ghost images.

Polarimetric calibration components. The filter wheel FW0 includes three polarization calibration components: a linear polarizer, a quarter wave plate, and a circular polarizer which are described in Bazzon et al. (2012). The linear polarizer produces essentially a 100% polarized illumination of ZIMPOL which is used to determine and calibrate the modulation efficiency ϵ_{mod} as described in Sect. 2.3.3.

The quarter wave plate and the circular polarizer are used for polarization cross-talk measurements and other instrument tests. Identical polarization calibration components like for ZIMPOL are also available in the SPHERE common path (cal.pol in Fig. 1) and together they allow a detailed characterization of the instrument polarization of the entire SPHERE/ZIMPOL visual channel as outlined in Bazzon et al. (2012).

2.3. ZIMPOL detectors

The ZIMPOL CCD detector properties are quite special because of the demodulation functionality required for the polarimetric mode. This section gives a brief description of detector properties and the resulting observational data, while more details are given in Schmid et al. (2012).

The detectors are two back-illuminated, frame transfer CCDs with an imaging area of $2\text{k} \times 2\text{k}$ and $15\ \mu\text{m} \times 15\ \mu\text{m}$ pixels. The CCDs are operated like $1\text{k} \times 1\text{k}$ pixel frame transfer CCDs with 2×2 pixel binning providing an effective pixel size of $30\ \mu\text{m} \times 30\ \mu\text{m}$. In the following a “pixel” always means this $30\ \mu\text{m}$ binned pixel. The quantum efficiencies of the (bare) CCDs are about 0.95, 0.90 and 0.65 at $\lambda = 600\ \text{nm}$, $700\ \text{nm}$ and $800\ \text{nm}$ respectively, while the photo-response non-uniformity is $\leq 2\%$ up to $800\ \text{nm}$ as measured with $5\ \text{nm}$ band widths. For longer wavelengths fringing is visible, which becomes dominant for $\lambda > 750\ \text{nm}$, but remains for $\Delta\lambda = 5\ \text{nm}$ at a level $< 4\%$ up to $900\ \text{nm}$.

In front of the CCD imaging area is a stripe mask and a cylindrical micro-lens array as illustrated in Fig. 5. There is a substrate with a photo-lithographic mask on the backside with 512 stripes and a width of $40\ \mu\text{m}$ which are separated by gaps of $20\ \mu\text{m}$. On the front side are an equal number of cylindrical micro-lenses with a width of $60\ \mu\text{m}$ which focus the light through the gaps onto the CCD. The stripes and micro-lenses assembly are fixed about $10\ \mu\text{m}$ above the CCD and they are aligned with the pixel rows of the detector.

On one detector there are 512 open rows with 1024 pixel each separated by one masked row. In polarimetric mode the photo-charges created in the illuminated rows are shifted up and down in synchronization with the polarimetric modulation and the final frame consists of an “even rows” subframe I_e for one polarization state I_{\perp} , and an “odd rows” subframe I_o for the opposite polarization state I_{\parallel} with 1024×512 pixels each.

In imaging mode there is no charge shifting and the final frame consists of an “illuminated rows” subframe with 1024×512 pixels with the scientifically relevant data and a “covered rows” subframe with some residual signal from light or photo-charges which diffused from the open rows into the covered rows.

Figure 6 shows small sections of two raw $H\alpha$ frames of the central R Aqr binary taken in polarimetric and imaging mode

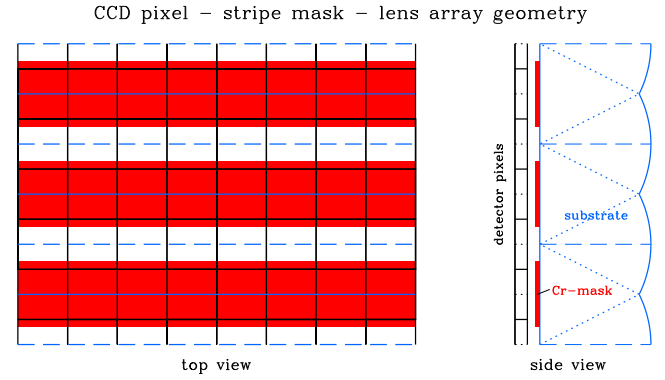


Fig. 5. Schematic setup of a small section of the ZIMPOL detector assembly with the stripe mask (red), the cylindrical micro lens array with the dashed focus line (blue) and the detector pixels (black).

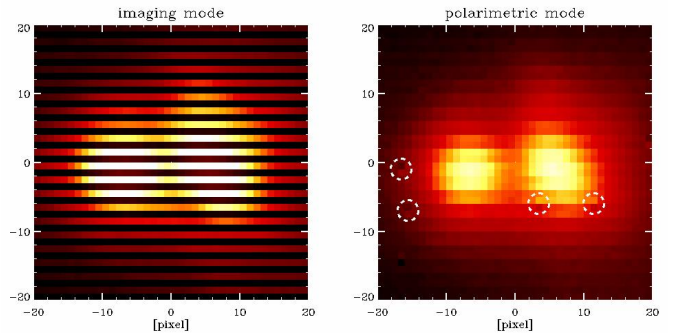


Fig. 6. Raw counts for the central 40×40 pixel regions of the $H\alpha$ images for the central R Aqr binary, separation 45 mas, taken in imaging mode (left) and in polarimetric mode (right). The dotted circles in the polarimetric data indicate spurious charge shifting effects.

(from Schmid et al. 2017). In imaging mode, there is a large illumination difference between the open rows and covered rows. The entire image is illuminated in polarimetry despite the stripe mask because of the charge shifting

The extracted subframes (even/odd or illuminated/covered rows) have an unequal dimension with twice the number of pixels in the row direction. The raw frames can be converted into a 512×512 pixel square format by a two pixel binning in row direction or into a 1024×1024 pixel square format by inserting everywhere between two adjacent rows one additional row with a flux conserving linear interpolation in column direction.

The pixel scale for even/odd or the illuminated/covered subframes are about $3.6\ \text{mas}$ in row direction and $7.2\ \text{mas}$ in column direction. The two pixel or Nyquist sampling in column direction is therefore $14.4\ \text{mas}$ and this corresponds to the diffraction limit of the VLT telescope λ/D at a wavelength of $570\ \text{nm}$. However, the spatial resolution achieved with ZIMPOL is typically above $20\ \text{mas}$ because of telescope and instrument vibrations, optical aberrations and other effects, so that the pixel sampling in column direction is also adequate for the shortest wavelength filter V_S ($532\ \text{nm}$). Nonetheless, it can be beneficial for the data analysis to arrange interesting structures of the target along the better sampled row direction, like the close binary in Fig. 6.

2.3.1. Detector modes

Three detector modes are fully characterized and tested for ZIMPOL, one for imaging and two for imaging polarimetry.

Table 4. Parameters for the ZIMPOL imaging and polarimetric detector modes.

Parameter	Unit	Imaging	Polarimetry	
			Fast	Slow
min. DIT $t_{\text{DIT}}^{\text{min}}$	s	1.1	1.1	10
Transfer time t_{ft}	ms	56	56	74
max. frame rate	Hz	0.86	0.86	0.1
Read out freq.	kpix s ⁻¹	625	625	100
Pixel gain	e ⁻ ADU ⁻¹	10.5	10.5	1.5
Read out noise	e ⁻ pix ⁻¹	20	20	3
Well depth	ke ⁻ pix ⁻¹	670	670	100
Dark current	e ⁻ (s pix) ⁻¹	0.2	0.2	0.015
Bias level	ct pix ⁻¹	≈1000	≈1000	≈1000
Polarimetry				
mod. freq. ν_{mod}	Hz		967.5	26.97
Row shift time	μs		54.7	72.3

Important parameters for these modes are given in Table 4. The imaging and the fast polarimetry modes are conceived for high contrast observations of bright stars and the slow polarimetry mode for longer integrations of images with lower illumination levels.

The two ZIMPOL detectors are controlled for all detector modes strictly in parallel. The CCDs are operated as frame transfer devices where read-out of a frame in the shielded read-out area occurs during the integration (and demodulation in polarimetric mode) of the next frame in the imaging area (Schmid et al. 2012). Therefore, the shortest possible integration $t_{\text{DIT}}^{\text{min}}$ is essentially the read-out time for one frame. After the integration a frame is shifted with a fast frame transfer from the image area to the read-out area and a new cycle of integration and read-out starts. The fast frame transfer introduces a small detector overhead of t_{ft} per frame and a smearing of the image which can be easily recognized as trails in column direction in short integrations of bright or saturated point sources (see Fig. 8). ZIMPOL includes a fast shutter to suppress the frame transfer smearing but it has been disabled because of technical problems. The ZIMPOL design does not require a shutter for the basic instrument-break modes.

Table 4 lists the electronic parameters for the different CCD modes, like read-out noise (RON), dark current (DC), and pixel gain. RON and DC need to be measured regularly for the calibration of the science data. The two CCDs are read out each by two read-out registers, one for the left half and the other for the right half of one detector. Each read-out register has a slightly different bias level which can vary by a few counts from frame to frame if the device is run with high frame rates. For this reason, the read-out registers provide for each half row also 25 pre-scan and 41 overscan pixel readings for each frame to correct properly the bias level in the data reduction. The raw frame format resulting from this read-out scheme is described in Schmid et al. (2012).

The standard imaging detector mode provides fast read-out and a high pixel gain of 10.5 e⁻ ADU⁻¹. The read-out noise is about 2 ADU pix⁻¹, but because of the high gain this corresponds to a rather large RON ≈ 20 e⁻. Therefore, the standard imaging mode is not ideal for low flux observations and a low RON imaging mode for faint targets should be considered as a possible future detector upgrade. At the moment one can use the slow polarimetry mode as low-RON imaging mode.

A key feature of the polarimetric detector modes is the charge up and down shifting with a cycle period of $P_{\text{mod}} = 1/\nu_{\text{mod}} = 1.03$ ms for fast or $P_{\text{mod}} = 37$ ms for slow modulation.

Fast modulation is designed to search for polarized sources, for example planets or disks, near (<0.3'') bright stars with short integration times (≈1–5 s), high gain, and a deep full well capacity for collecting many photo-electrons per pixel (>10⁵) for high precision polarimetry. The modulation between I_{\perp} and I_{\parallel} is faster than the typical atmospheric coherence time $\tau_0 \approx 2 - 5$ ms for medium and good seeing conditions (≤1'') at the VLT and therefore it is possible to suppress the speckle noise and reach a polarimetric sensitivity level at the photon noise limit of up to 10⁻⁵. Such a performance can only be reached if ≈10¹⁰ photo-electrons can be collected per spatial resolution element with a diameter of about 28 mas, or a synthetic aperture with ≈50 pix² per detector what requires $n > 1000$ well exposed frames. Therefore, the fast modulation mode is tuned for short detector integration times $t_{\text{DIT}} < 10$ s and high exposure levels >1000 e⁻ pix⁻¹ for which the high read-out noise RON ≈ 20 e⁻ pix⁻¹ is not limiting the performance. The fast modulation mode produces a fixed bias pattern consisting of two pixel columns with special bias level values because the read-out of a pixel row must be interrupted to avoid interference with the simultaneous charge shifting in the image area. The pattern can be removed with a standard bias subtraction procedure (see Schmid et al. 2012).

The slow modulation mode is conceived and useful for polarimetry of sources around fainter stars or with narrow filters. This mode provides a slow modulation, but allows long integration times ≥10 s and delivers data with low RON ≈ 2–3 e⁻ pix⁻¹ appropriate for low flux levels.

2.3.2. Charge traps in polarimetric imaging

The up and down shifting of charges during the on-chip demodulation causes single pixel effects due to charge traps. This anticipated problem was minimized with the selection of CCDs with a charge transfer efficiency of better than 99.9995%. A charge trap can hold for example one electron during a down shift and then release it in the following up-shift. In this way a trap can dig after 1000 shifts a hole of 1000 e⁻ in the subframe of one modulation state, e.g. I_{\perp} , and produce a corresponding spike in the I_{\parallel} subframe. A few examples are marked in the polarimetric frame of Fig. 6. This problem is solved with a phase switching in which the charge shifting is reversed in every second frame with respect to the polarization modulation. With such a double phase measurements one can construct a double difference

$$p^Z = \frac{(I_o(z) - I_e(z)) - (I_o(\pi) - I_e(\pi))}{2}, \quad (5)$$

for which the charge trap effects are cancelled or at least strongly reduced in the polarization signal (Gisler et al. 2004; Schmid et al. 2012). I_o and I_e are the counts registered in the odd and even detector rows for either the zero (z) or π phase shifts between modulation and demodulation. In ZIMPOL, the alternating phase shifts are implemented automatically for polarimetric detector integrations and therefore only even number of frames can be taken per exposure. The charge trap effects increase with the number of modulation cycle and they are therefore small for short integrations t_{DIT} and slow modulation mode. Unfortunately, the charge trap effects are not corrected for the intensity signal $I = I_{\perp} + I_{\parallel}$ obtained with polarimetric imaging, and the affected pixels must be treated and cleaned like ‘‘bad’’ detector pixels.

2.3.3. The polarimetric modulation-demodulation efficiency

The ZIMPOL modulation-demodulation efficiency ϵ_{mod} is regularly measured with a standard calibration procedure (`p_cal_modeff`). This calibration takes fully polarized $P = I_{\perp} = I^{100}$ ($I_{\parallel} = 0$) flat field illumination using the calibration lamp in front of SPHERE and the polarizer in the ZIMPOL filter wheel FW0. The calibration measures either the mean fractional polarization $\epsilon = \langle P^Z/I \rangle$ or a 2-dimensional efficiency frame

$$\epsilon(x, y) = P^Z(x, y)/I^{100}(x, y).$$

The efficiency ϵ_{mod} is less than one because of several static and temporal effects which depend on many factors, mainly on the modulation frequency and the detector arm, but also on wavelengths (or filter) and on the location on the detector.

On the masked CCD, there is a leakage of photons and newly created photo-charges from the e.g. I_{\perp} -subframe in the illuminated pixel rows to the adjacent covered pixel rows of the I_{\parallel} subframe, of about $\delta_{\text{static}} \approx 5\%$. This reduces the efficiency by the factor $\epsilon_{\text{static}} = 1 - 2\delta_{\text{static}} \approx 0.9$. The effect is slightly field dependent because the alignment of the stripe mask with the pixel rows, and therefore the leakage to the covered rows, is not exactly equal everywhere on the detector.

The polarization beam splitter is essentially perfect for the transmitted light in arm1, while about $\delta_{\text{arm2}} \approx 3\%$ of the “wrong” I_{\parallel} intensity is deflected together with I_{\perp} into arm2. This reduces the relative efficiency of arm2 by $\epsilon_{\text{arm2}} = (1 - \delta_{\text{arm2}})/(1 + \delta_{\text{arm2}}) \approx 0.94$.

For fast modulation a temporal efficiency loss occurs because a finite time of about $75 \mu\text{s}$ is required for the FLC modulation switch and the CCD line shift. This reduces the modulation-demodulation efficiency of ZIMPOL by about 10% or $\epsilon_{\text{temp}} \approx 0.9$ for the fast modulation mode. For slow modulation the temporal effect can be neglected.

It results a ZIMPOL overall polarimetric efficiency of about $\epsilon_{\text{mod}} \approx \epsilon_{\text{temp}}\epsilon_{\text{static}} \approx 0.8$ for fast modulation polarimetry and $\epsilon_{\text{mod}} \approx \epsilon_{\text{static}} \approx 0.9$ for slow modulation polarimetry with arm1. For arm2 an additional factor of $\epsilon_{\text{arm2}} \approx 0.95$ needs to be included (see [Bazzon et al. 2012](#); [Schmid et al. 2012](#), for further details).

The fast frame transfer (with open shutter) causes also a reduction of the measured efficiency for the measured fractional polarization P^Z/I . During the frame transfer the detector is still illuminated and the intensity $I_{\perp}/2 + I_{\parallel}/2$ is added during the frame transfer time t_{ft} to both, the I_{\perp} - and I_{\parallel} -subframes. This reduces for a polarized flat-field illumination, or a full frame aperture measurement like for a standard star, the fractional polarization P^Z/I by

$$\epsilon_{\text{ft}} = t_{\text{DIT}}/(t_{\text{DIT}} + t_{\text{ft}}). \quad (6)$$

The frame transfer effect is stronger for short integration times in fast modulation. The factor is $\epsilon_{\text{ft}} = 0.973, 0.986,$ and 0.995 for integration times of $t_{\text{DIT}} = 2, 4,$ and 8 s (and $t_{\text{ft}} = 56$ ms). For slow polarimetry with $t_{\text{ft}} = 74$ ms there is $\epsilon_{\text{ft}} = 0.993$ for $t_{\text{DIT}}^{\text{min}} = 10$ s and higher for longer integrations.

Table 5 gives the mean values from many calibrations taken throughout the year 2015 for $\epsilon_{\text{ft}}\epsilon_{\text{mod}} = P^Z/I$, while ϵ_{mod} are the efficiencies corrected for the transfer smearing according to Eq. (6). The calibrations show clearly the ϵ_{mod} -differences between cam1 and cam2 and between fast and slow modulation in particular with the ratios given in the last column and the bottom row. The N_R data taken with $t_{\text{DIT}} = 4, 2,$ and 1.1 s illustrate well the ϵ_{ft} dependence. The efficiency ϵ_{mod} shows also a small dependence on wavelength. The efficiencies ϵ_{mod} given

Table 5. Calibration measurements taken during the year 2015 for the modulation – demodulation efficiencies $\epsilon_{\text{ft}}\epsilon_{\text{mod}}$ and ϵ_{mod} in various filters.

Filter	t_{DIT} (s)	n	$\epsilon_{\text{ft}}\epsilon_{\text{mod}}$		ϵ_{mod}		Ratio $\frac{\text{cam1}}{\text{cam2}}$
			cam1	cam2	cam1	cam2	
Fast modulation							
V	8	9	0.772	0.748	<i>0.778</i>	<i>0.753</i>	1.032
R_PRIM	2	3	0.805	0.747	0.828	0.768	
N_R	4	8	0.818	0.751	<i>0.829</i>	<i>0.761</i>	1.089
N_R	2	4	0.808	0.744	0.831	0.765	
N_R	1.1	1	0.794	0.730	0.834	0.767	
B_Ha	10	1	0.824	0.778	0.829	0.782	
VBB	1.1	2	0.783	0.744	0.823	0.782	
TiO717	8	1	0.827		0.833		
Cnt847	8	1		0.783		0.788	
Cnt820	8	2	0.807	0.767	0.813	0.772	
N_I	4	8	0.802	0.774	<i>0.813</i>	<i>0.785</i>	1.036
I_PRIM	2	2	0.802	0.769	0.824	0.791	
Slow modulation							
V	10	6	0.848	0.821	<i>0.854</i>	<i>0.827</i>	1.033
N_R	10	7	0.904	0.831	<i>0.911</i>	<i>0.837</i>	1.088
N_I	10	1	0.894	0.862	<i>0.900</i>	<i>0.868</i>	1.037
Cnt820	10	4	0.890	0.844	0.897	0.850	
			$\epsilon_{\text{mod}}(\text{fast})/\epsilon_{\text{mod}}(\text{slow})$		0.908	0.908	

Notes. The third column indicates the number of calibrations used for the mean value given in the following four columns. Recommended values for the V, R, and I bands are highlighted in italics, while the last column gives the corresponding cam1/cam2 ratios and the bottom row the fast to slow modulation for these filters. The scatter for multiple calibrations taken with the same setup is $\sigma_{\epsilon} \approx 0.003\text{--}0.005$.

in italics are recommended values for a particular camera, modulation mode, and filter. The statistical uncertainties in the ϵ_{mod} calibrations are less than $\sigma < 0.005$ as derived from sets of four or more measurements taken during 2015 with the same instrument configuration. Thus, the ϵ_{mod} calibrations are very stable for a given configuration and the obtained values or calibration frames are valid for a month typically and possibly even longer.

The degradation of the polarization flux because of the non-perfect (<1) modulation-demodulation efficiency of ZIMPOL is corrected with a calibration frame $\epsilon_{\text{mod}}(x, y)$ according to

$$P_{\text{cl}}^Z(x, y) = P^Z(x, y)/\epsilon_{\text{mod}}(x, y), \quad (7)$$

which we call polarimetric correction “c1”. This type of correction considers also the field dependent detector effects but might also introduce pixel noise from the calibration frame if not corrected. For not very high signal to noise data $P/\Delta P < 50$, it is good enough to correct the $P^Z(x, y)$ just with a mean value $\langle \epsilon_{\text{mod}} \rangle$ as given in Table 5. For the derivation of the fractional polarization P^Z/I in a large aperture one needs also to account for the frame transfer illumination by using $\epsilon_{\text{mod}}\epsilon_{\text{ft}}$.

2.4. ZIMPOL filters

The pass bands of the available ZIMPOL color filters are shown in Fig. 7 and listed in Table 6 with central wavelengths λ_c , filter widths $\Delta\lambda$ (FWHM), their location in the filter wheels, and whether they can be combined with the dichroic beam splitter or with one of the two coronagraphic four-quadrant phase masks 4QPM1 or 4QPM2 (see Sect. 4). Table 6 includes also the calibration and test components in the filter wheels.

The ZIMPOL filters were selected based on several technical and scientific requirements:

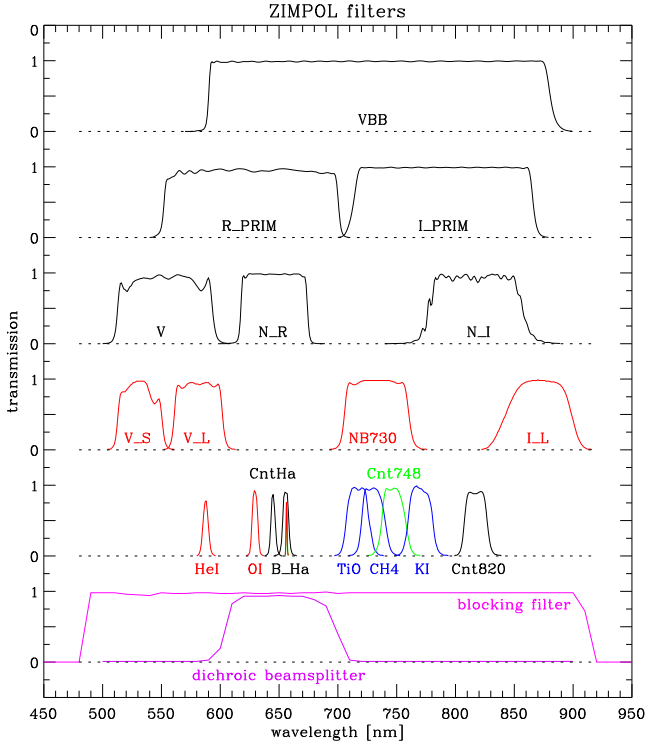


Fig. 7. Transmission curves for the ZIMPOL color filters, the blocking filter and the dichroic beamsplitter. Black curves are used for filters located in FW1 and FW2, red for filters in FW0, blue are filters in FW1 only, and green filters in FW2 only.

For *imaging*, all pass band filters can be used. The filters in FW1 and FW2 can be combined with one of the three neutral density filters located in FW0 to avoid image saturation. One can use the same filter type in FW1 and FW2 to optimize the sensitivity in that pass band or one can also use simultaneously two different filters in FW1 and FW2. The latter mode provides spectral differential imaging, e.g. combining an H α filter with the continuum filter CntHa. Alternatively, using different filters provides an efficient way to get angular differential imaging with large field rotation in two pass bands simultaneously, e.g. R_PRIM and I_PRIM, during one single meridian passage of a target.

When combining different filters in FW1 and FW2 it needs to be considered that the detector integration times are equal in both channels. Broad-band filters combined with narrow band filters can therefore cause strongly different illumination levels on the two detectors.

The filters in FW1 and FW2 are recommended for polarimetry, because they are located after the polarization beam-splitter and the polarization is encoded as intensity modulation. Therefore, polarization dependent pass bands and other polarization effects of the filters do not affect the polarization measurements. Only for these filters a modulation-demodulation efficiency ϵ_{mod} can be determined, because this calibration requires the polarizer located in FW0. Polarimetry using the neutral density filters or the color filters in FW0 is also possible but with an increased polarimetric calibration uncertainty. More work is required to characterize accurately such non-optimal polarimetric modes.

Different filters can be used in FW1 and FW2 simultaneously for ZIMPOL polarimetry, because each arm provides a full polarization measurement. Thus one can perform a combination of simultaneous spectral and polarimetric differential imaging with ZIMPOL.

Table 6. Pass-band filters, neutral density filters, and calibration components available in the filter wheels FW0, FW1 and FW2 of ZIMPOL.

Component	λ_c (nm)	$\Delta\lambda$ (nm)	Wheel FWx			Dichr. BS ^a	4QPM ^b 1/2
			0	1	2		
Open			+	+	+	y	
Broadband filters							
VBB	735	290		+	+		
R_PRIM	626	149		+	+		
I_PRIM	790	153		+	+		
V	554	81		+	+		
N_R	646	57		+	+	y	1
N_I	817	81		+	+		2
Narrowband filters							
V_S	532	37	+				
V_L	582	41	+				
NB730	733	55	+				
I_L	871	56	+				
TiO717	716.8	19.7		+			
CH4_727	730.3	20.5		+			
Cnt748	747.4	20.6			+		
KI	770.2	21.1		+			
Cnt820	817.3	19.8		+	+		2
Line filters							
HeI	588.0	5.4	+				
OI_630	629.5	5.4	+			y	1
CntHa	644.9	4.1		+	+	y	1
B_Ha	655.6	5.5		+	+	y	1
N_Ha	656.9	1.0	+			y	1
Ha_NB	656.9	1.0			+	y	1
Neutral density filters ^c							
ND1	500–900		+			y	
ND2	500–900		+			y	
ND4	500–900		+			y	
Calibration components							
Polarizer				+		+	
Quarter wave plate				+		+	
Circular polarizer				+		+	
Pupil imaging lens						+	+

Notes. ^(a) This column indicates components (y = yes), which can be used together with the dichroic beam splitter. ^(b) This column marks the recommended color filters to be used with 4QPM1 (indicated by 1) or 4QPM2 (indicated by 2). ^(c) The neutral density (ND) filters attenuate the throughput by about a factor $\approx 10^{-1}$ for ND1, $\approx 10^{-2}$ for ND2, and $\approx 10^{-4}$ for ND4.

There are some instrument configurations which can only be combined with certain filters. Observations with the dichroic beam-splitter between ZIMPOL and WFS provide more photons for the WFS and is therefore particularly beneficial for faint stars. This mode must use the filters N_R, B_Ha, N_Ha, NB_Ha, CntHa, and OI_630, which have their pass bands in the transmission window of the dichroic BS plate (Table 6, Col. 7). The R-band four quadrant phase mask coronagraph 4QPM1 has its central working wavelength at 650 nm and is also designed for these filters. The I-band 4QPM2 with central wavelength 820 nm requires the filters Cnt820 or N_I for good results (Table 6, Col. 8).

The following list gives important scientific criteria which were considered for the selection of the different filters:

- V, N_R and N_I broad band filters for imaging and polarimetry of stars and circumstellar dust,
- RI (or VBB for very broad band), R_PRIM, and I_PRIM broad band filters for demanding high contrast observation where a high photon rate is beneficial for the detection,
- TiO_717, CH4_727, KI, Cnt748 and Cnt820 for narrow band imaging, spectral differential imaging and polarimetry of cool stars, substellar objects and solar system objects,
- B_Ha, N_Ha and CntHa for imaging, spectral differential imaging, and polarimetry of circumstellar H α emission,

- V_S, V_L, 730_NB, I_L for better coverage of the ZIMPOL spectral range with intermediate band filters,
- OI_630 and HeI as additional line filters for the imaging of circumstellar emission,
- N_R, the H α filters B_Ha, N_Ha (NB_Ha), CntHa, and OI_630 in combination with the dichroic beam splitter for imaging, differential imaging and polarimetry of fainter targets $R \gtrsim 9$ mag, where the AO performance profits from the higher photon throughput to the wave front sensor.

Photometric instrument throughput. The total instrument throughput for each filter, or the photometric zero points, should be determined for flux measurements. This value depends on the used system configuration (polarimetry, imaging, ND-filters, etc.), and some preliminary values are given in Schmid et al. (2017). However, for many applications one can use an unsaturated image of the central bright star, for example taken with a ND-filter, as photometric reference for the flux calibration of a faint circumstellar source.

Blocking filter. A problem of the pass band filters is their insufficient blocking of the transmission (often not less than 0.001) for wavelengths outside the ZIMPOL range $\lambda < 500$ nm and $\lambda > 900$ nm. This can be particularly harmful for coronagraphic observations, where radiation from the central, bright source is displaced for wavelengths outside the ZIMPOL spectral range, because the atmospheric dispersion corrector is not designed to correct for these wavelengths. For coronagraphic images some of the central star radiation, e.g. the blue light (420 – 480 nm), might not fall onto the focal plane mask. This would create a point like signal slightly outside the mask despite an out-of-band attenuation of $ND \approx 3$ of the color filter. For this reason a blocking filter is added on the “free” position of the modulator slider for imaging, and one is added to the entrance window of the modulator vacuum housing for polarimetry.

3. The AO corrected point spread function

The PSF obtained with SPHERE/ZIMPOL are complex and depend on wavelengths, atmospheric conditions, star brightness and observing modes. This section describes characteristic PSF parameters for many different cases.

3.1. Two-dimensional PSF structure

Figure 8 shows the averaged PSFs of HD 183143 in the V-band and the N_I band for 48s of integration each taken on 2015-09-18, the N_I-frames about 2 min after the V-frames. These are “typical” PSFs for a bright star and for stable and good atmospheric conditions.

The polarimetric mode P1 with derotator fixed was used, and the PSF is displayed in the orientation of the detectors with x and y in row and column directions, respectively. The corresponding polarization images for the V-band PSF are discussed in Sect. 5.5.

Prominent PSF features in Fig. 8 are the strong speckle ring at a spatial separation corresponding roughly to the AO control radius of $r_{AO} = 20 \lambda/D$ up to which the AO corrects the “seeing” speckles. This corresponds to $\rho_{AO} \approx 0.3''$ for the V-band and $\rho_{AO} \approx 0.45''$ for the N_I-band. Dashed rings indicate azimuthal cuts through the PSF, which are shown in Fig. 9. Strong quasi-static speckles from the AO system, marked with “s”, are always present left and right from the PSF peak on the speckle ring near $r = 80$ pix for V and $r = 120$ pix for N_I. Another feature of the PSF are the diffraction pattern of the four spiders holding the M2 telescope mirror and two of the four appear particularly

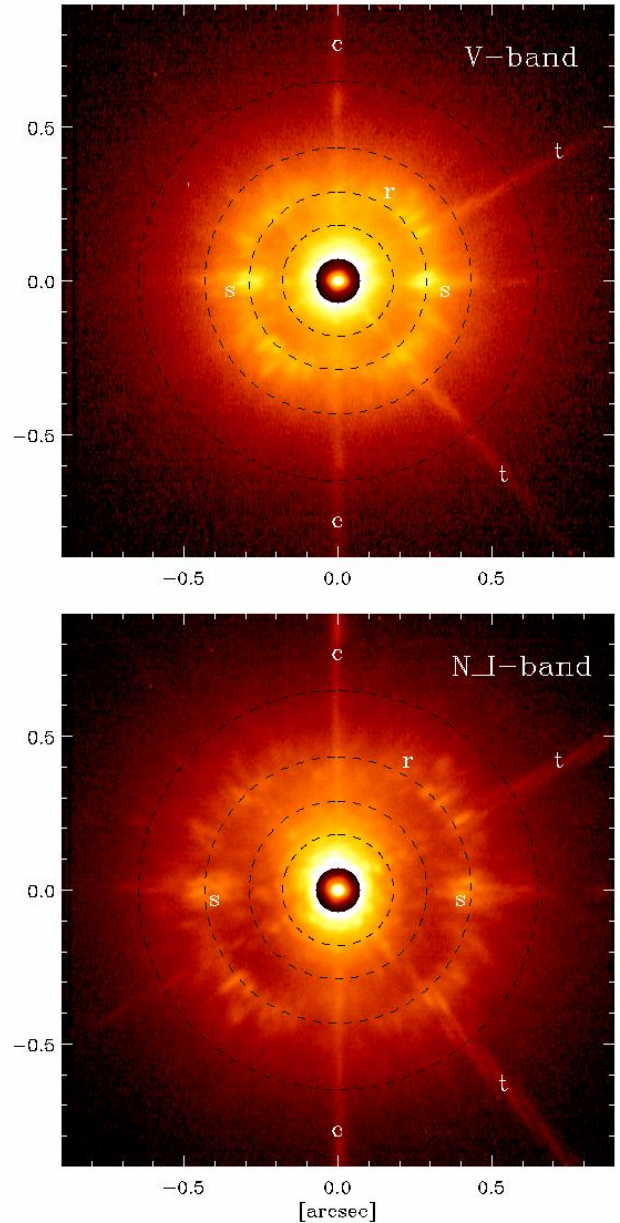


Fig. 8. Normalized PSFs of HD 183143 for the V-band (top) and the N_I-band (bottom) with the color scale reduced by a factor of 100 for the central peak within $r < 20$ pixels. Marked PSF features are the speckle ring near the AO control radius (r), strong fixed speckles from the AO system (s), two telescope M2 spider features (t), and the CCD frame transfer trail of the PSF peak (c). The dashed rings illustrate the location of the azimuthal cuts shown in Fig. 9.

bright in Fig. 9. The vertical line through the PSF peak is the frame transfer trail, which is caused by the illumination of the detector during the fast frame transfer. The trail is particularly strong for non-coronagraphic observations of bright stars with short integrations (see Eq. (6)).

Figure 9 gives averaged radial profiles and azimuthal cuts of the PSF for a more quantitative description. The PSFs in Figs. 8 and 9 are given in units of ct_{n6} where the counts are normalized to 10^6 counts within a round aperture with a diameter of $3''$. The normalization of the surface brightness SB [mag arcsec^{-2}] of a PSF to the total stellar flux m_{star} [mag] defines a normalized surface brightness or a surface brightness contrast C_{SB}

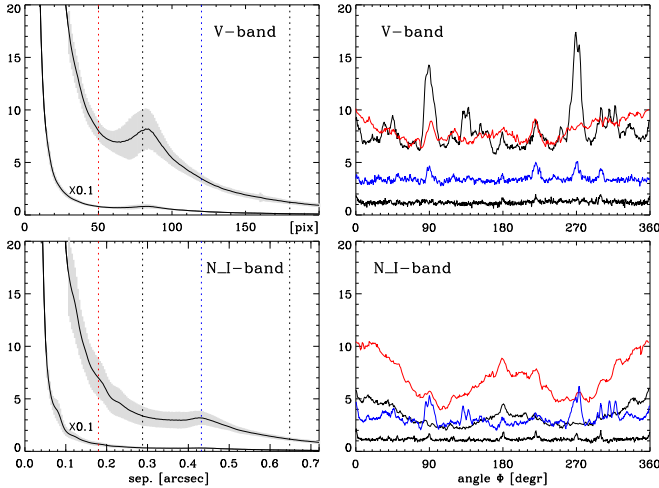


Fig. 9. Azimuthally averaged radial profiles $ct_{n6}(\rho)$ (left) and azimuthal profiles $ct_{n6}(r, \phi)$ for $r = 50, 80, 120$ and 180 pix (right) corresponding to $\rho = 0.18''$, $0.29''$, $0.43''$, and $0.65''$, respectively for the PSFs of HD 183143 shown in Fig. 8. Also indicated as gray shading are the standard deviations of the azimuthal points $\sigma(ct_{n6}(r, \phi))$. The location of the azimuthal cuts are indicated in the $ct_{n6}(r)$ -panels and in Fig. 8.

[mag arcsec⁻²] according to:

$$C_{SB}(x, y) = SB(x, y) - m_{star}. \quad (8)$$

This translates, for the applied PSF normalization of 10^6 ct in the $3''$ -aperture, to the following normalized surface brightness conversion between ct_{n6} [pix⁻¹] and mag arcsec⁻²

$$C_{SB}(x, y) = -2.5^m \log(ct_{n6}(x, y)) + 2.78^m, \quad (9)$$

using $-2.5^m \log(77160/10^6) = +2.78^m$ because one arcsec² contains 77160 pixels on one ZIMPOL detector. Thus, a PSF peak surface brightness of $ct_{n6}(r = 0) = 5000$ ct pix⁻¹ corresponds to a normalized surface brightness of $C_{SB}(0) = -6.47$ mag arcsec⁻². A signal of 1 ct_{n6} for example from a faint companion with a point source contrast of about $\Delta m \approx 9.25^m$, is at the level to be visible for $r \gtrsim 80$ pix in the normalized images and cuts shown in Figs. 8 and 9 except for the regions of the speckle ring.

The radial PSF profiles in Fig. 9 show the azimuthal mean with the standard deviation $\pm\sigma$ indicated in gray. Four radii were selected to show the azimuthal profiles $ct_{n6}(r, \phi)$ of the PSF as function of position angle ϕ measured counterclockwise from top. The innermost ring profiles $r = 50$ pix show a sine-like pattern, especially for the N_I band, with two maxima and minima within 360° . They originate from the slightly elongated base of the very strong $ct_{n6}(0) \approx 5000$ ct pix⁻¹ PSF peak (see also Fig. 11). Such PSF extensions are often present and they can be caused by a dominant wind direction.

The speckle rings at $r \approx 80$ pix in the V-band and at $r \approx 120$ pix for the N_R band produce very strong noise features on small angular scales. The strongest speckles are at 90° and 270° degrees from the AO system as already discussed above (Fig. 8). Speckles are weaker inside the speckle ring and outside they are hardly recognizable besides the faint traces from the spiders at $\phi = 220^\circ$ and 300° and the frame-transfer trail at 0° and 180° . Because of the location of the speckle rings the N_I-band observations would be much more sensitive in the radial range $0.2''$ – $0.4''$ than V-band observations. On the other side a faint target at a separation between $\rho = 0.4''$ – $0.5''$ might be easier to detect

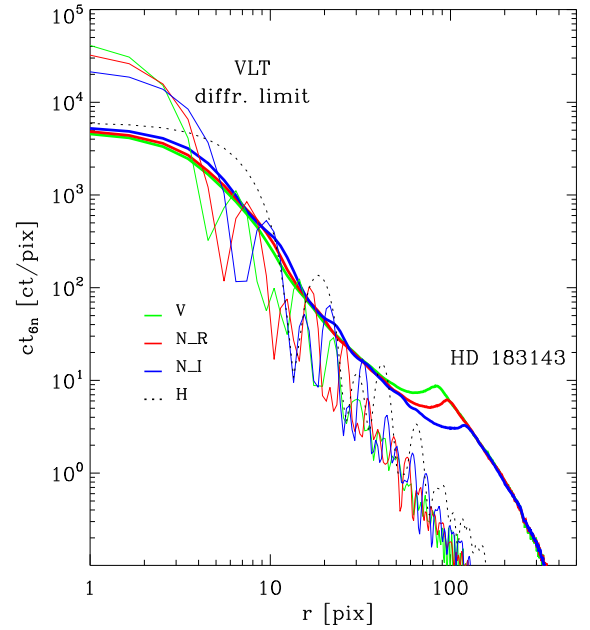


Fig. 10. Flux normalized PSFs $ct_{n6}(r)$ for HD 183143 (thick profiles) and the calculated diffraction limited PSF of the VLT (thin profile) for the filters V ($\lambda = 545$ nm), N_R (645 nm), N_I (817 nm), and including the H-band ($1.62 \mu\text{m}$) for the VLT. One pixel is 3.6 mas.

(assuming gray color distributions) just outside the speckle ring in the V-band than on the speckle ring in I-band.

The dominant noise sources are the distortions close to the center, the strong speckles further outside, and the read-out noise outside of the control ring. The read-out noise regime can be pushed outwards easily with a stronger frame illumination, where the PSF peak is saturated or close to saturation, or with coronagraphic observations.

3.2. Parameters for the radial PSF

To simplify our discussion we focus on the radial profiles of the PSF keeping in mind the significant deviations from rotational symmetry discussed above (Figs. 8 and 9). We use as basis for this brief overview the polarimetric standard star data from the ESO archive taken in polarimetric mode in the V, N_R, N_I band filter, which are regularly obtained by ESO staff as part of the SPHERE instrument calibration plan. In addition we include a few special PSF cases. As a starting point, we have selected the data of HD 183143 from Sept. 18, 2015 (Figs. 8 and 9) as typical examples of SPHERE/ZIMPOL PSFs for the V, N_R and N_I-band taken under good atmospheric conditions.

PSF wavelength dependence. Figure 10 compares the flux normalized radial profiles $ct_{n6}(r)$, with equally normalized diffraction limited profiles $f(r)/f_{3\text{dia}}$ calculated for the VLT with an 8.2 m primary mirror and a 1.1 m central obscuration by the secondary mirror and where $f_{3\text{dia}}$ is the total flux within an aperture with a diameter of $3''$. Also shown is the H-band ($1.62 \mu\text{m}$) diffraction profile. For each filter $f(r)$ is the mean PSF for several wavelengths equally distributed over the filter range to account for the filter widths.

The normalized peak flux $ct_{n6}(0)$ for HD 183143 (Fig. 10) are roughly at the same level for all filters. The most prominent difference between the PSFs is the wavelength dependence of the radius of the local maximum associated with the speckle ring. Contrary to the observed profiles the peak flux of the normalized VLT diffraction PSFs depend strongly on wavelength. For the

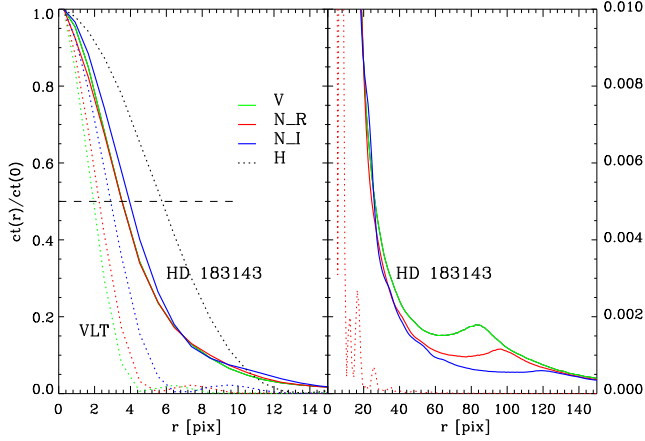


Fig. 11. Same PSFs for HD 183143 and the VLT diffraction limit as in Fig. 10 but normalized to the peak flux. The dashed line in the *left panel* marks the half width at half maximum of the profiles. The dotted curves are the calculated diffraction limited profiles. The flux scale in the *right panel* is 100 times lower.

pixel size of $3.6 \times 3.6 \text{ mas}^2$ there is $f(0)/f_{3\text{dia}} = 5.13\%$, 3.80% , and 2.36% for the V, N_R, and N_I filters, respectively (see bottom lines in Table 7).

We use the normalized peak flux $ct_{n6}(0)$ as key parameter to compare the PSF quality of different SPHERE/ZIMPOL observations. This value can be determined easily and under good atmospheric conditions similar values in the range 0.4–1.0% are obtained for different wavelengths.

For a comparison with the performance of other instruments one should translate the peak flux into a Strehl ratio. An approximate Strehl ratio S_0 can be calculated with the relation

$$S_0 = \frac{ct_{n6}(0)}{f(0)/f_{3\text{dia}}}.$$

One should note, that a lower Strehl ratio at shorter wavelengths is not equivalent with a lower normalized peak flux because the diffraction peak depends strongly on wavelength, like $f(0)/f_{3\text{dia}} \propto 1/\lambda^2$.

The approximate Strehl ratio S_0 provides a useful parameter for a simple assessment of the SPHERE/ZIMPOL system PSF. However, the S_0 value does not describe well the SPHERE AO performance, because there exist instrumental effects which degrade the PSF peak which are not related to the adaptive optics (as discussed in Schmid et al. 2017). A more sophisticated AO characterization should be based on the analysis of the Fourier transform of the aberrated image as described in Sauvage et al. (2007). Such an analysis yields for the N_I-filter PSF of HD 183143 an AO Strehl ratio of 33% instead of the 23% resulting from the values given in Table 7. The difference can be explained by a residual background at low spatial frequencies caused for example by instrumental stray light, not corrected frame transfer smearing, and other effects.

Figure 11 shows the peak normalized PSF of HD 183143 for the three filter on a linear scale. The PSF full width at half maximum (FWHM) are significantly larger, by about 2–3 pixels or 7–11 mas, when compared to the diffraction limited profile (Table 7). Different effects contribute to this degradation like small pointing drifts, residual PSF jitter because of telescope and instrument vibrations, residuals from the atmospheric dispersion correction and other uncorrected optical aberrations, cross-talks between detector pixels, and possibly more. Also shown in this

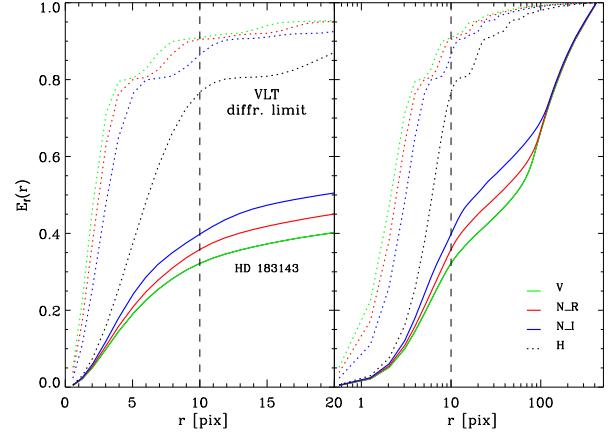


Fig. 12. Profiles for the normalized encircled flux $E_f(r)$ for the same PSFs of HD 183143 and the VLT diffraction as in Fig. 10. The dashed lines illustrate the parameter E_{f10} .

plot are the maxima of the speckle rings. The mean profiles can be misleading when considering the strong azimuthal dependence discussed in Fig. 9.

The profiles of the normalized encircled flux $E_f(r)$ shown in Fig. 12 is another way to characterize the PSFs. This plot illustrates that only about 20% of the total PSF flux is encircled in an aperture with $r = 5 \text{ pix}$ (18 mas), or about 30% for $r = 10 \text{ pix}$. The encircled flux is an important parameter for flux determinations using synthetic apertures. We select as characteristic parameter the halo and background corrected encircled flux E_{f10} for an aperture radius of $r = 10 \text{ pix}$, using the mean flux value $\langle ct_{n6}(r = 11) \rangle$ of the pixel ring with $r = 11 \text{ pix}$ as background and halo level, which is subtracted from all 317 pixels i within the aperture $r_i \leq 10 \text{ pix}$

$$E_{f10} = \frac{1}{10^6} \sum_{r_i \leq 10} [ct_{n6}(x_i, y_i) - \langle ct_{n6}(r = 11) \rangle]. \quad (10)$$

This type of encircled energy measurement is also applicable to the PSF peak of faint companions, for which it is not possible to measure the outer part of the PSF. For high contrast measurements we need E_{f10} , or encircled energies for other apertures with small radii, to derive the flux contrast between central star and faint companion. The measured E_{f10} -values for HD 183143 and other test cases are given in Table 7.

3.3. PSF variations

The PSFs obtained with SPHERE/ZIMPOL show a large diversity depending on atmospheric conditions, central star brightness, AO performance, and instrumental mode, and a few typical cases are discussed in this subsection. Table 7 lists for the analyzed profiles the measured PSF values for the normalized peak flux $ct_{n6}(0)$, the encircled energy E_{f10} , and full width at half maximum FWHM. Also given are atmospheric and instrument parameters taken from the ESO data file headers. Seeing and coherence time τ_0 are measured for the vertical direction with the DIM-MASS systems.

Atmospheric conditions. The PSF of SPHERE/ZIMPOL changes often strongly within one night and under instable conditions even from frame to frame. Figure 13 compares for bright standard stars the typical or “good” PSFs of HD 183143 for the V-band and the N_I band with the “excellent” PSFs of observations of HD 161096 and the “bad” PSFs of HD 129502. These

Table 7. PSF characteristics for three typical standard stars and several special cases.

Star Name	m_R (mag)	Date Airmass	Atmosphere			Instrument mode			PSF parameters		
			Seeing ($''$)	τ_0 (ms)	v_{wind} (m s^{-1})	Mode ^a $\nu(\text{AO})/\text{SpF}$	Filter	$n_{\text{DIT}} \times t_{\text{DIT}}$ (s)	$ct_{\text{th6}}(0)/10^6$ (%)	E_{f10} (%)	$FWHM$ (mas)
standard stars											
HD 183143	5.74	15-09-18	0.73	8.3	5.2	P1 pol.	V	12×4	0.486	28.1	25.4
“good”		1.72				1.2 kHz/S	N_R	12×4	0.533	29.8	25.4
							N_I	12×4	0.548	32.4	28.4
HD 129502	3.48	15-04-19	1.20	1.4	2.2	P1 pol.	V	16×2	0.148	14.7	43.8
“bad”		1.06				1.2 kHz/M	N_R	8×4	0.389	20.2	25.3
							N_I	16×2	0.369	18.1	27.7
HD 161096	1.96	15-04-28	0.88	4.6	5.7	P1 pol.	V	16×2	0.733	36.5	22.6
“excellent”		1.20				1.2 kHz/S	N_R	16×2	0.919	43.5	22.5
							N_I	16×2	0.842	41.5	25.3
special cases											
HD 142527	8.3	17-06-01	0.65	11.6	1.5	P2 pol.	VBB	1×3	0.196	35.1	53.8
“low wind effect”		1.05				600 Hz/M					
MMS 12	10.5	14-10-11	1.40	2.1	3.8	imaging	I_PRIM	3×40	0.039	7.0	53.1
“faint”		1.49				300 Hz/L					
R Aqr	8.8 ^b	14-10-11	0.83	2.8	13.6	P2 pol.	V	8×10	0.091	10.5	34.1
“red source”		1.13				1.2 kHz/M	Cnt820	20×1.2	0.541	41.0	28.0
α Eri	0.49	14-10-13	1.40	1.60	3.0	imaging	CntHa	50×0.01	1.02	48.2	19.3
“snap shot”		1.25				1.2 kHz/S					
α Hya	2.55	14-10-10	0.83	2.8	13.6	ima	R_PRIM	10×1.1	0.798	40.5	20.5
“coro test source”		1.36				1.2 kHz/M	I_PRIM	10×1.1	0.781	46.5	23.8
						VLT diff. limit	V		5.13	91.0	14.2
							N_R		3.80	90.6	16.8
							N_I		2.36	86.7	21.0
							H		0.583	76.3	41.6

Notes. The last four lines give the PSF parameters for the calculated, diffraction limited PSFs for the VLT. ^(a) $\nu(\text{AO})$ is the AO loop frequency and SpF the used spatial filter (S = small, M = medium, L = large) for the WFS ^(b) brightness in other bands is $m_V = 11.4^m$ and $m_I = 4.4^m$ (Schmid et al. 2017).

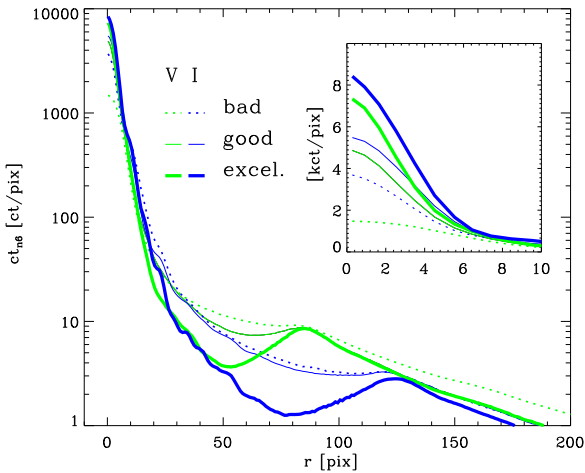


Fig. 13. Normalized radial profiles ct_{6m} for V- and N_I-band observations of HD 161096 with “excellent”, for HD 183143 with “good”, and HD 129502 with “bad” quality PSFs.

three examples represent quite well the much larger data set of bright standard stars available in the ESO archive. These archive data show an overall correlation between good PSFs parameters and long atmospheric coherence time scales $\tau_0 \geq 3$ ms or good seeing $\leq 0.9''$ and bad PSFs for short time scales $\tau_0 \leq 2$ ms or mediocre seeing $\geq 1.0''$. This is roughly in agreement with the study of Milli et al. (2017) on SPHERE PSF properties in the near IR. Bad atmospheric conditions as for the observations of HD 129501, affect much more the short-wavelength V-band

profile. Other effects, for example the high airmass for the observations of HD 183143, play also a role.

Let us consider in more detail the contrast characteristics of the three N_I profiles bad, good, and excellent in Fig. 13 and Table 7. Normalized peak fluxes and encircled fluxes scale roughly like 0.7 : 1.0 : 1.4 between bad : good : excellent conditions. The normalized mean flux level at $r = 80$ pix is much lower ≈ 1.5 ct for the “excellent” PSF, and ≈ 5 ct for the “good” and “bad” PSF. The speckle noise is measured as standard deviation of fluxes in apertures at $r = 80$ pix ($0.29''$) as illustrated for the case of α Hyi B in Fig. 21a. This yields the 5- σ raw contrasts for the faint point source detection at $\rho = 0.29''$ of about $8 \times 10^{-4} : 4 \times 10^{-4} : 2.3 \times 10^{-4}$ for the bad : good : excellent PSFs discussed here.

This rough estimate does not consider differential imaging techniques for speckle noise suppression, which may change the picture. In any case, there exist dramatic differences of factors 2–4 in the SPHERE/ZIMPOL contrast performance for bad, good or excellent atmospheric conditions which are of great importance when defining the seeing requirements for observations of a particular object.

Low wind effect. The PSF of HD 142527 in Fig. 14a is an extreme example for the so called low wind effect, which leads to multiple PSF peaks in the center. This is explained in Sauvage et al. (2016a) by a discontinuity in the wave front phase in the pupil plane at the location of the mirror M2 telescope spiders. These spiders are cold and cause a temperature difference between the air in upwind and downwind direction. Such phase offsets are not easily recognized by the Shack-Hartmann WFS and therefore different PSF peaks result. This effect is only

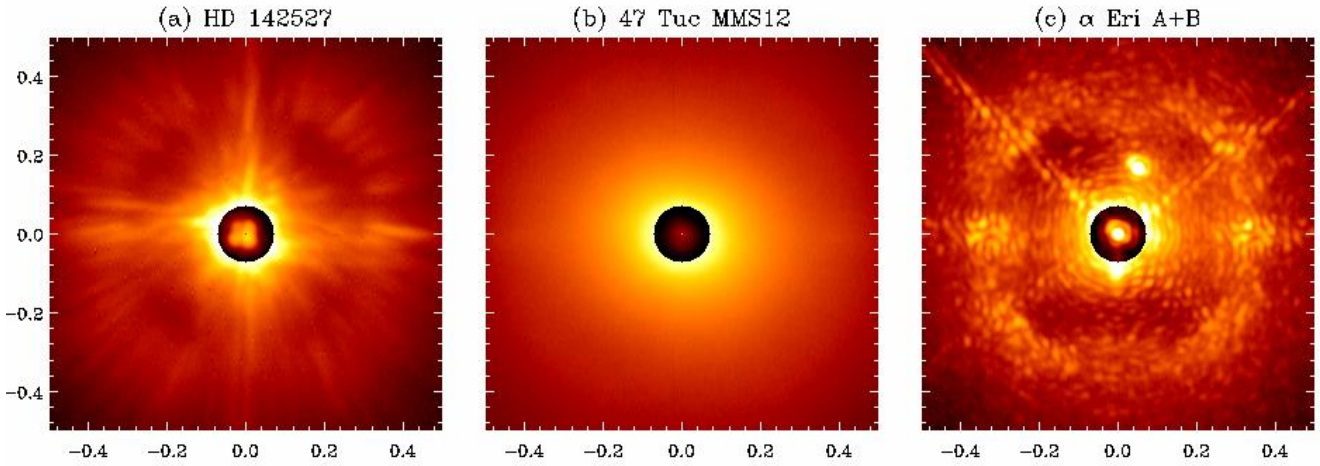


Fig. 14. Normalized PSFs for special cases: *Panel a:* VBB-filter image of HD 142527 as example for the low wind effect, *panel b:* faint star 47 Tuc MMS12 in I_PRIM, and *panel c:* a 10 ms snap-shot image of α Eri A and B in the line filter CntHa. The color scale is reduced by a factor of 100 for the PSF center within $\rho < 0.072''$. Axes are in arcsec.

observed when the wind is particularly slow, $\lesssim 2 \text{ m s}^{-1}$, so that the heat exchange between spider and air induces a substantial temperature difference. The atmospheric conditions for the observation of HD 142527 were in principle excellent with a very good seeing of $0.65''$ and a long coherence time of 11.5 ms, but a wind speed of only 1.5 m s^{-1} (Table 7). The FWHM is 53 mas for the multiple peaked PSF and the relative peak flux $ct_{n6}(0)$ is a factor 2.5–4.0 lower than for other PSFs taken under sub-arcsecond seeing conditions.

Still relatively high is the encircled energy $E_{f10} = 35\%$, which is comparable to “good” atmospheric conditions. Thus the low wind effect splits the central PSF peak and degrades the resolution, but at larger separation the $E_f(r)$ -profile is not much affected. This means that the sensitivity for high contrast imaging of extended circumstellar scattering regions is not strongly degraded by the low wind effect, apart from the reduced spatial resolution. For example, the ZIMPOL observations of the protoplanetary disk around TW Hya described by van Boekel et al. (2017) suffered from the low wind effect, but despite this the quality of the resulting disk images is good and certainly competitive with near-IR observations from other AO instruments (Akiyama et al. 2015; Rapson et al. 2015).

Central star brightness and color. The AO performance degrades for faint stars, because of the lack of photons for accurate measurements and corrections of the wave front distortions. In addition the WFS shares the photons in the “visual” range 500 – 900 nm with the ZIMPOL science channel. The gray beamsplitter (zw.BS) reflects only 21% of the light to the WFS and therefore the AO performance degrades significantly for stars fainter than about $R \approx 8^m$ (see Sauvage et al. 2016b). This limit is relaxed to about $R = 9.2^m$, if the dichroic beamsplitter is used instead of the gray beam splitter, but then the useful spectral range for ZIMPOL is reduced to the N_R-filter and the line filters B_Ha, N_Ha, CntHa and OI (see Fig. 7). For faint central stars there are means to optimize the AO system with longer integrations with the WFS camera, running with reduced AO-loop frequencies of 600 Hz or 300 Hz instead of 1200 Hz, and the use of a large spatial filter in the WFS arm (see Sauvage et al. 2016b). A mirror instead of a beam splitter is used for infrared science observations and therefore more light reaches the WFS and the corresponding limit is about $R \approx 10.0^m$.

Figure 14b shows as example for a faint star the central regions of 47 Tuc MMS12, the central star of the astrometric field from Fig. 3. This star has only $R = 10.5^m$ and was observed with the gray beam splitter under mediocre atmospheric conditions at high airmass and therefore the resulting PSF is strongly downgraded. When compared to the N_I band PSF of the bright HD 129502, which was observed under similar seeing conditions, then the faint star in 47 Tuc MMS12 has a 10 \times lower normalized peak flux (or Strehl ratio), 3 \times lower encircled flux E_{f10} , and a 2 \times enhanced FWHM (Table 7). Figure 3 demonstrates that the resulting image can still be useful, but the broad and extended PSF is strongly reducing the spatial resolution and the contrast performance, and produces a much higher read-out noise limit for faint stars.

The AO-correction may also depend on the color of the central star. A strong wavelength dependence of the PSF parameters is reported by Schmid et al. (2017) for the Mira variable R Aqr with very red colors $V - I = 7^m$. The normalized peak counts $ct_{nb}(0)$ show a strong wavelength dependence with 0.54% for the I-band but only 0.09% for the V-band (Table 7). The explanation is most likely, that the WFS “sees” essentially only I-band light, because of the very red color of the star, and therefore the AO-system performs less good in the V-band.

PSF structure and instrument mode. A few special instrumental effects are noticeable in the PSFs shown in Fig. 14a and c.

Figure 14a shows the PSF of the star HD 142527 taken with the VBB filter with a filter widths of $\Delta\lambda = 290 \text{ nm}$ for a central wavelength of $\lambda_c = 735 \text{ nm}$ or $\lambda_c/\Delta\lambda = 2.53$. In this case the speckles are strongly extended radially. This has the disadvantage that the ring of bright speckles is very broad, but on the other side the flux of an individual speckle is distributed over many pixels and therefore the elongated speckles are less prominent, and they can be distinguished more easily from a faint point source companion.

The star α Eri A with its fainter companion α Eri B were taken during the SPHERE commissioning with the narrow line filter CntHa with a very short integration of 10 ms using the “snap shot” engineering mode of the ZIMPOL detector, and a single 10 ms exposure is shown in Fig. 14c. For our data we measure for the companion a relative separation of $175 \pm 4 \text{ mas}$, a sky position angle of $-19.5^\circ \pm 2.0^\circ$, and a flux ratio of about

$f_B/f_A = 0.014$. This position measured by us for 2014-10-13 (2014.78) coincides with the location for epoch 2007.75 in the partial orbit measured by Kervella et al. (2008), indicating an orbital period of about 7.0 ± 0.1 yr for the α Eri binary. Because of the narrow filter and the very short integration the speckles are strong and point like because there is no or only little radial and temporal smearing, respectively. For averaged PSFs or PSFs taken with long integration times like in Fig. 8, the pattern of the strongly variable speckles will average out and only strong quasi-static speckles remain clearly visible. We note, that the PSF parameters given in Table 7 are derived from averaged PSFs of n_{DIT} -images where the PSF of each image was re-centered individually before adding it to the others.

The PSF peak for α Eri is very narrow, because slow instrumental drifts and vibrations with frequencies < 100 Hz do not broaden the PSF peak in very short integration. Further, there is no spectral dispersion because the line filter CntHa produces essentially monochromatic images. For these reasons, the PSF of α Eri has a *FWHM* of ≈ 19 mas, which is about 1 pixel better than for the observations taken under “excellent” conditions or 2 pixels better than for “good” conditions (Table 7).

Not corrected instrumental vibrations can also be recognized in the frame transfer trails of a bright source. These trails wiggle left and right with a scatter of $\sigma \approx 1$ –2 pix from the mean position and one such excursion extends over about 200 pixels in vertical direction corresponding to a time scale of 10 ms during the frame transfer. This residual PSF jitter explains partly the discrepancy of 2–3 pix between observed widths of the PSF peak and the nominal width of a diffraction limited PSF profile.

Lucky imaging and speckle suppression techniques can be optimized with a careful selection of instrument and observing parameters, which enhance or reduce the speckle variations between frames or which modify the geometric appearance of speckles (e.g. Law et al. 2009; Brandner et al. 2016). It is beyond the scope of this paper to investigate further such techniques apart from pointing out that ZIMPOL offers a broad range of instrument modes which can be exploited.

4. Coronagraphy

Coronagraphy is a powerful tool to suppress the light of a bright object for the search of faint sources at small separation (Malbet 1996; Sivaramakrishnan et al. 2001). The basic concept of the SPHERE visual coronagraph is a classical Lyot coronagraph where the focal plane mask stops the light of the bright star and the pupil mask stops the diffracted light from the telescope and the coronagraph in a pupil plane further downstream. SPHERE has a focal plane exchange wheel with 16 positions equipped with 7 round focal plane masks, 2 monochromatic four quadrant phase masks (4QPM), two open field stops (see Table 8), and 4 empty positions. There is also an exchange wheel with 8 positions for pupil stops (Table 9).

The *F*-ratio of the coronagraph is $F\# = 30$ and the pupil size in the collimated beam is 6 mm in diameter. The focal plane masks serve also as field stop for ZIMPOL defining either a circular “wide field” (WF) with a radius of $\rho = 4''$ or a “narrow field” (NF) of $1'' \times 1''$ for a very fast, windowed detector read-out mode for polarimetry, which was not commissioned yet.

We use the stellar system α Hyi (HR 591, HIP 9236) as a test target for the on-sky characterization of the SPHERE visual coronagraphs. α Hyi is a bright $m_V = 2.9^m$, nearby (22 pc), F0 star and was used as test target in the commissioning. It turned out to have a nearby companion which is ideal for the characterization of the SPHERE visual coronagraph. α Hyi B is not

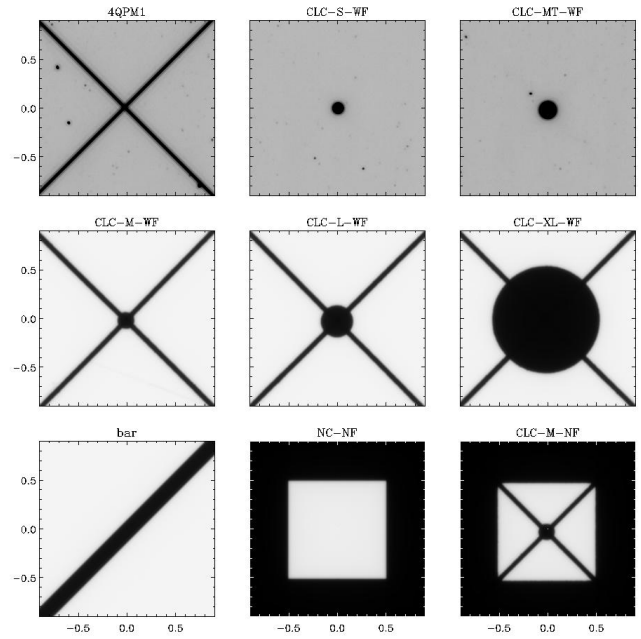


Fig. 15. Images of the central part ($1.8'' \times 1.8''$) of focal plane masks available in the visual coronagraph of SPHERE. The masks in the *top row* are deposited on a plate and the gray scale is enhanced to show the frequency of dust features on the masks.

in the SIMBAD data base but the Hipparcos catalog gives for α Hyi a binary orbit for the astrometric photo-center motion with an orbital period of $P = 606$ days and a semi-major axis of 21.7 mas. On 2014-10-10 we measure a separation of 91 ± 3 mas and a position angle of $-19^\circ \pm 2^\circ$. The companion is about $5.8^m \pm 0.2^m$ and $6.5^m \pm 0.2^m$ fainter than the primary in the I_PRIM and R_PRIM bands, respectively (see Table 10).

The atmospheric conditions for our coronagraph tests were photometric, with an atmospheric coherence time of about $\tau_0 \approx 2.8$ ms and a seeing of roughly $0.83''$ (see Table 7).

4.1. Coronagraphic focal plane masks

Figure 15 shows images of the central region ($1.8'' \times 1.8''$) of nine focal plane masks obtained with flat-field lamp illuminations. For non-coronagraphic observations, the clear field stop NC_WF (or NC_NF for window mode) are used. Non-coronagraphic observations can also be obtained by offsetting the star from the mask, but then a shadow from the coronagraph will be present in the image and the pupil stop is still in place. Such “offset PSFs” taken before or after coronagraphic observations are very useful for the flux calibration and the PSF characterization.

Several Lyot coronagraphs with different spot sizes are available. Small spots, suitable for small inner working angles, are made of a metallic coating deposited on transparent plates with the disadvantage that dust particles on the plate are visible in the recorded images. In Fig. 15 the gray scale for CLC_S_WF, CLC_MT_WF (and 4QPM1) is enhanced to illustrate the frequency of such dust features as seen for our tests in Oct. 2014.

Larger coronagraphic spots are suspended with thin wires. Dust are no problem for these masks but the suspension spiders, which have a full width of $40 \mu\text{m} = 34$ mas, can be an important issue for the observing strategy and the data reduction.

The coronagraphic attenuation of the PSF of α Hyi for the small CLC-S-WF, medium CLC-M-WF, large CLC-L-WF, and extra large CLC-XL-WF Lyot spots are shown for the I_PRIM

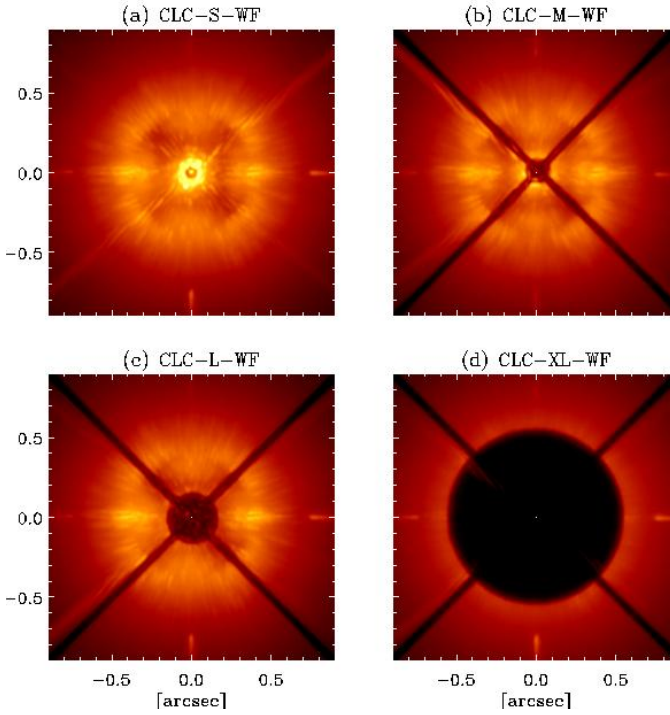


Fig. 16. Coronagraphic images of α Hyi ($1.8'' \times 1.8''$) for the I_PRIM-filter taken with the *panel a*: small S, *panel b*: medium M, *panel c*: large L, and *panel d*: extra-large XL focal plane masks of SPHERE. All images are normalized ct_{n6} relative to the non-coronagraphic PSF and displayed with the same color scale.

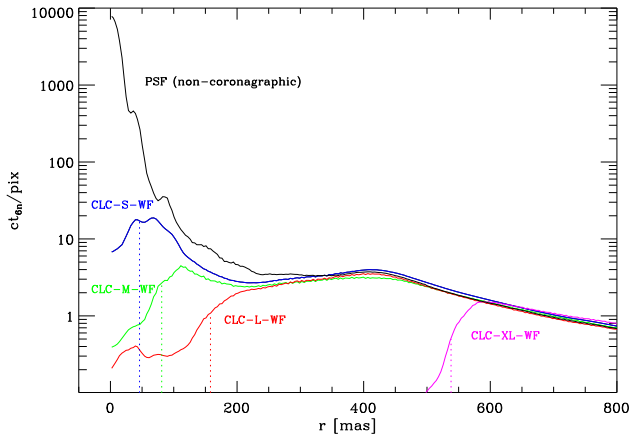


Fig. 17. Normalized radial profiles $ct_{n6}(r)$ for the I_PRIM coronagraphic images in Fig. 16 of α Hyi taken with the small S (blue), medium M (green), large L (red), and extra-large XL (magenta) focal plane stops. Also plotted is the non-coronagraphic PSF profile. The dotted lines indicate the nominal mask radii.

filter data in Fig. 16 as coronagraphic images and in Fig. 17 as azimuthally averaged radial profiles. These coronagraphic data were taken simultaneously in the I_PRIM filter for cam1 and the R_PRIM filter for cam2 using the pupil stopB1_2. Figure 17 includes a stellar PSF taken with the star offset by 550 mas from the mask spot and using the neutral density filter ND2 to avoid heavy saturation. The non-coronagraphic PSF was normalized to 10^6 ct for an aperture with a diameter of $3''$ and all the coronagraphic profiles were scaled to this ct_{n6} -normalization considering the exposure times and the attenuation of the neutral

Table 8. Focal plane masks in the SPHERE visual coronagraph.

Name	p	ρ (mas)	Remark	$\max(ct_{n6})$	
				R_PRIM	I_PRIM
NC_WF			Clear	7983	7813
NC_NF			Clear		
CLC_S_WF	+	46.5		72	52
CLC_M_WF		77.5		26	13
CLC_MT_WF	+	77.5	astrom. mask		
CLC_L_WF		155		31	11
CLC_XL_WF		538		7.5	2.7
CLC_S_NF	+	46.5	Not tested		
CLC_M_NF		77.5	Not tested		
4QPM1	+		$\lambda_0 = 666$ nm		
4QPM2	+		$\lambda_0 = 823$ nm		
Bar			$w = 155$ mas		

Notes. The first column gives the mask name where NC stands for no coronagraph, CLC for classical Lyot coronagraph, 4QPM for four quadrant phase mask, WF for wide field (radius $\rho = 4''$), NF for narrow field ($1'' \times 1''$). Masks on plates p are indicated in the second column and ρ is the mask radius in μm and converted to mas using the scale $0.86 \text{ mas } \mu\text{m}^{-1}$. The last two columns give the maximum normalized counts for the α Hyi tests (Fig. 16) for the R_PRIM and I_PRIM filters, respectively.

density filter ND2 (about a factor 130 for R_PRIM and 105 for I_PRIM) used for the non-coronagraphic observations. The two last columns in Table 8 give the maximum counts of the ct_{n6} -normalized images.

Depending on the spot size different features of the PSF are attenuated. The smallest mask CLC-S-WF reduces the flux peak by about a factor $R_{\text{coro}} \approx 110\text{--}150$, which corresponds to the ratio of the $\max(ct_{n6})$ -counts between off-mask PSF and coronagraphic image given in Table 8. This mask leaves a ring of strong residuals at a separation of about 60 mas just outside the coronagraphic spot. The next larger mask CLC-MT-WF ($\rho = 81$ mas) attenuates the central peak completely $R_{\text{coro}} \approx 300\text{--}600$, and the flux just outside the mask rim is comparable to the strong features in the speckle ring at $\rho \approx 0.3''\text{--}0.4''$. For CLC-L-WF the speckles in the speckle ring are the strongest emission features, while for CLC-XL-WF also all bright speckles in the ring are hidden and the coronagraphic attenuation reaches $R_{\text{coro}} \approx 1000\text{--}3000$.

Very useful for the determination of the stellar position in the coronagraphic images, in particular for the large focal plane masks, are the interference features from the DM at $\rho \approx 0.6''\text{--}0.9''$ above, below, left and right from the hidden star. They are essentially grating spectra of the central star created by the chessboard pattern from the DM actuators which can be recognized in the pupil image (see Fig. 19).

Another focal plane mask in the visual coronagraph is the astrometric mask CLC-MT-WF, which has a Lyot spot with a transmission of about 0.1%, so that the central star can be seen in the science image as a faint emission peak inside the spot shadow. This is very useful for astrometric measurements of circumstellar sources. This mask has no suspension wires which is an advantage when compared to CLC-M-WF. In addition, the mask has a Cartesian grid of smaller spots spaced by $1''$ for the astrometric location of sources observed in off-axis settings where the central star is outside the detector field of view. A central spot is often also visible for the small opaque mask CLC_S_WF, but this spot is produced by diffraction and should not be trusted for astrometric purposes.

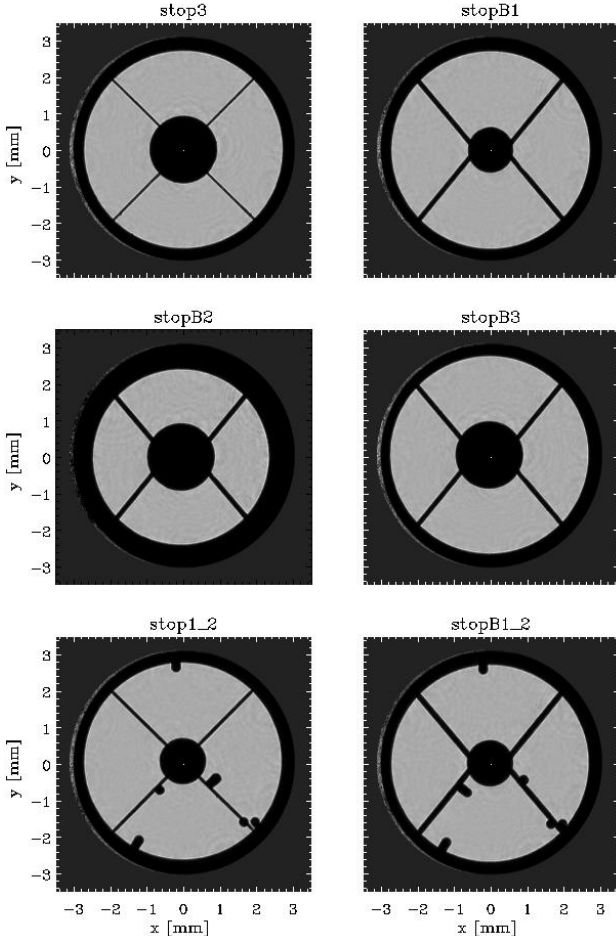


Fig. 18. Pupil stop images for the SPHERE visual coronagraph taken with the internal point source and the pupil imaging lens.

The four quadrant phase masks (4QPM) have a geometry as shown in Fig. 15 (top left). The plates produce a phase shift of π through a small optical path difference in the left and right quadrants with respect to the upper and lower quadrants introducing a destructive interference at the interfaces and a particularly efficient nulling for the central crossing (Rouan et al. 2000). The simple, monochromatic 4QPM used in ZIMPOL are designed for one wavelength λ_0 and the attenuation is less efficient for wavelengths away from λ_0 (Riaud et al. 2003). 4QPM1 with $\lambda_0 = 666$ nm is designed for the N_R-band filter the H α line filters B_Ha, N_Ha and CntHa. The 4QPM2 with $\lambda_0 = 820$ nm is foreseen for the N_I filter and the narrow band filter Cnt820.

The bar mask could be useful for the search of faint objects near a small separation ($\rho < 2.5''$) binary star. The orientation of the binary can be aligned with the bar in field stabilized mode with an offset of the field position angle. We have not tested the performance of this mask.

4.2. Pupil plane stops

An important part of classical Lyot coronagraphs and 4QPMs are pupil plane stops which suppress the light diffracted by the sharp edges of the telescope pupil and the coronagraphic mask in the focal plane (e.g. Sivaramakrishnan et al. 2001). In the coronagraph pupil the diffracted light is located in two bright rings, one just outside the central M2-mirror obstruction and one along the outer pupil edge. In the coronagraphic image the pupil masks reduce efficiently the strong inner diffraction rings and this effect

Table 9. Geometric parameters for the telescope pupil, the intermediate pupil, and the pupil stop masks in the SPHERE visual coronagraph.

	d_{in} (mm)	d_{out} (mm)	w_{spid} (mm)	geom.	T_{geom}
Telescope	1148	8200	41	VLT	
coro. pupil	<i>0.896</i>	<i>5.97</i>	<i>0.037</i>	VLT	
pupil stops					
Clear	–	6.60	–	–	100%
stop3	1.80	5.40	0.036	diag.	72.9%
stopB1	1.20	5.41	0.110	VLT	75.5%
stopB2	1.81	4.79	0.107	VLT	53.5%
stopB3	1.81	5.40	0.106	VLT	70.9%
STOP1_2	1.2 ^a	5.4 ^a	<i>0.084</i>	diag.+b	74.8%
STOPB1_2	1.2 ^a	5.4 ^a	<i>0.18</i>	VLT+b	72.6%
SAM ^a				7 holes	

Notes. The columns indicate the pupil or stop name, the diameter d_{in} and d_{out} of the inner stop and the outer edge, the width w_{spid} and the geometry of the spider arms, and the geometric transmission T_{geom} . Roman fonts give design values or values measured for the mechanical components, while italic fonts are values measured from pupil images; ^(a) The sparse aperture mask is described in Cheetham et al. (2016) and was not tested by us.

is quantified in the following for a test with the SPHERE visual coronagraph. In addition, a pupil stop can also suppress the cross-shaped pattern from the VLT M2-mirror spider and the “unfocused” light from bad actuators of the deformable mirror (DM).

With ZIMPOL, the pupil plane can be imaged with cam2 using a pupil lens located in FW2, while cam1 takes simultaneously a focal plane (PSF) image. Images of the stops of the SPHERE visual channel are shown in Fig. 18, while Table 9 lists geometric parameters of the components. The indicated geometric transmission T_{geom} is derived from the pupil images and corresponds to the open area of the pupil stop with respect to the geometry of the telescope aperture as imaged in the coronagraphic pupil plane (=100%).

There are two basic types of pupil stops, simple masks which cover only the diffraction rings along the pupil rims for observing modes without pupil stabilization (stop3 and stop1_2) and pupil masks which hide in addition the telescope spiders for pupil stabilized observations (stopB1, stopB2, stopB3 and stopB1_2). Because of the bad actuators of the deformable mirror, special stops with blockers for the scattered light from these actuators located close to the pupil rim or spiders were manufactured (stop1_2 and stopB1_2). Different inner and outer stop diameters allow an optimization for high throughput (stopB1, stop1_2, stopB1_2), for a good rejection of the diffracted light (stopB2), or for an intermediate case (stop3, stopB3). The masks stop1_2 and stopB1_2 were used in 2015 as default masks.

The effect of the stopB1_2 for a coronagraphic image taken with CLC_S_WF is demonstrated in Figs. 19 and 20 for the close binary α Hyi using filter NB_730 in FW0 and the pupil stabilized imaging mode. The panels in Fig. 19 show in (a) the pupil image Φ_{no_stop} without stop and in (c) Φ with pupil stop, while panels (b) and (d) show the corresponding coronagraphic images f_{no_stop} and f , respectively, where the faint companion B is located below and slightly left of the center in these pupil-stabilized, non-derotated images. The bottom panels of Fig. 19 show the differences of the two pupil images $\Phi_{no_stop} - \Phi$ and the difference for the corresponding PSFs images $c \cdot f_{no_stop} - f$, where the scaling factor $c = 0.68$ accounts for the reduced

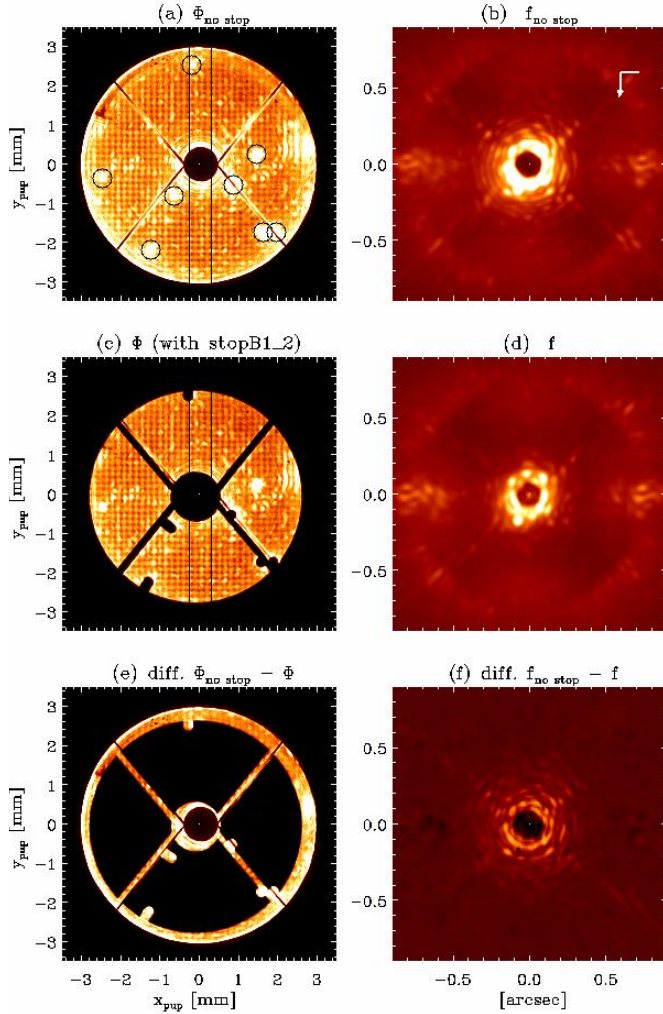


Fig. 19. Images of the pupil plane (*left*) and the center of the focal plane (*right*) for a coronagraphic observation of α Hyi with the focal plane mask CLC-S-WF without pupil stop (*top row*) and with pupil stop (*middle row*). The *bottom panels* are the differences of the two upper panels.

off-axis flux transmission because of the geometric attenuation by the pupil stop.

The vertical cross section through the pupil and the radial PSF profiles plotted in Fig. 20 allow a more quantitative assessment of the different features in the pupil plane and the focal plane. The profiles $\Phi(0, y)$ show clearly the contribution of the extra light in the diffraction rings at $y \approx \pm 0.4$ mm and ± 3 mm above the average level of about 1300 ct pix^{-1} . The relative contribution of the diffracted light is about $\Phi_{\text{diff}}/\Phi_{\text{no_stop}} = 5.0\%$, while the contribution of the 8 brightest maxima caused by bad actuators is $\Phi_{\text{dead}}/\Phi_{\text{no_stop}} = 1.5\%$. In addition there is also scattered light outside the pupil $r > 3$ mm and inside the central hole $r < 0.4$ mm which accounts for about $\Phi_{\text{scatt}}/\Phi_{\text{no_stop}} = 2.5\%$ of the total light in the pupil.

The pupil stop covers the diffracted light at the inner and outer pupil edges, most of the dead actuator peaks, and the scattered light inside and outside the telescope aperture. Beside this, the stop has a geometric transmission of $T_{\text{geom}} = 72.6\%$ of the telescope aperture. An approximate relation for the ratio of transmitted light with and without pupil stop is therefore

$$\frac{\Phi}{\Phi_{\text{no_stop}}} \approx \left(1 - \frac{\Phi_{\text{diff}}}{\Phi_{\text{no_stop}}} - \frac{\Phi_{\text{dead}}}{\Phi_{\text{no_stop}}} - \frac{\Phi_{\text{scatt}}}{\Phi_{\text{no_stop}}}\right) \cdot T_{\text{geom}} \approx 0.91 T_{\text{geom}}.$$

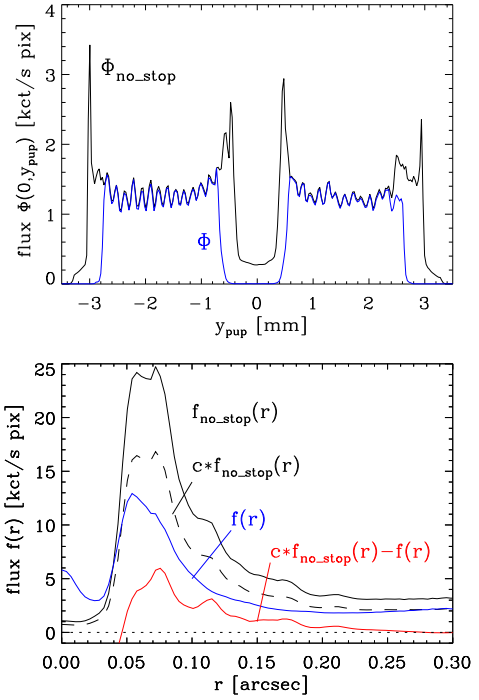


Fig. 20. Vertical pupil intensity profiles Φ (*top*) and mean radial profiles $f(r)$ (*bottom*) for the coronagraphic observation (CLC_S_WF) of α Hyi without pupil stop (black) and with stopB1_2 (blue). The red curve in the *bottom panel* shows the diffracted light in the focal plane which are suppressed by the pupil stop.

The alignment of the pupil stop in Fig. 19 is offset by about 0.13 mm toward the left and slightly downwards. For this reason the telescope spiders on the upper left and lower right are not hidden by the pupil mask spiders. Fortunately, the misalignment is sufficiently small, so that the special light blockers still attenuate the unfocused light from the dead actuators. The noticed small misalignment is certainly not ideal, but also not devastating because the telescope spiders are not an important flux feature ($< 1\%$) in the pupil.

Important is the attenuation of the diffracted light in the pupil for the reduction of the diffraction rings in the final coronagraphic science image. Because of the diffraction suppression the faint component B of α Hyi is much better visible in the coronagraphic image taken with pupil stop. Figure 20 compares the radial profiles for the coronagraphic images with $f(r)$ and without pupil stop $f_{\text{no_stop}}(r)$. This comparison has to consider the reduced effective telescope aperture and therefore throughput $c = T_{\text{geom}} = 0.726$ because of the geometric attenuation of the stopB1_2. The difference $c \cdot f_{\text{no_stop}}(r) - f(r)$ (red curve in Fig. 20) illustrates the suppression of the diffracted light from the central star by the pupil stop. The effect is particularly large in the radial range $\rho \approx 0.06'' - 0.20''$. The level of light in the coronagraphic image is reduced by factors ≈ 0.63 and 0.55 at the diffraction ring peak separation of 76 mas and 115 mas, respectively, and ≈ 0.71 for the minimum at 94 mas. Thus the effect is very significant near the coronagraphic mask.

The gain in the contrast performance is not only a function of the residual coronagraphic flux $f(r)$, but also on the speckle noise near the coronagraphic mask. It is difficult to give a general “gain value” for a coronagraphic system, because the speckles depend so much on the observing conditions. For the one case investigated here for α Hyi, the gain in S/N for the measurement of the companion at $\rho = 0.091''$ is thanks to the suppression

Table 10. Measurements of the flux ratio f_B/f_A and the $(S/N)_B$ of α Hyi A and B, using different coronagraphic configurations of SPHERE/ZIMPOL.

Instrument configuration		f_B/f_A	$(S/N)_B$	Figs.
Coro / Angle,	Filter, $n_{\text{DIT}} \times t_{\text{DIT}}[\text{s}]$	(10^{-3})		
Test A: CLC-S-WF without / with pupil stop, pupil stabilized				
Without stop	NB730 10 × 8	^a	5.2	19
With stop	NB730 10 × 8	^a	9.7	19
Test B: different coronagraphic configurations				
off coro, ND2 ^b	I-PRIM 10 × 1.1	5.6	4.8	21
CLC-S-WF	I-PRIM 10 × 3	5.3	12.2	21
CLC-MT-WF	I-PRIM 10 × 3	4.0	11.6	21
4QPM2	N_I 20 × 3	^a	10.3	21
4QPM2	Cnt820 20 × 3	^a	9.1	
off coro, ND2 ^b	R-PRIM 10 × 1.1	2.7	3.5	
CLC-S-WF	R-PRIM 10 × 3	3.2	8.2	
CLC-MT-WF	R-PRIM 10 × 3	2.6	8.0	
Test C: different rotation angles with CLC-S-WF				
0°	I-PRIM 20 × 3	5.3	12.2	
60°	I-PRIM 20 × 3	3.7	5.2	
120°	I-PRIM 20 × 3	5.3	10.0	
mean	I-PRIM	4.7 ± 0.8	10.0	
median-subtr.	I-PRIM	3.6 ^c	15.9	
0°	R-PRIM 20 × 3	2.7	5.8	22
60°	R-PRIM 20 × 3	2.1	3.3	22
120°	R-PRIM 20 × 3	3.1	4.6	22
Mean	R-PRIM	2.6 ± 0.5	4.6	22
median-subtr.	R-PRIM	1.6 ^c	10.5	22

Notes. Commissioning data taken on 2014-10-10 between UT 7:40 and 8:50; ^(a) no f_A flux available; ^(b) PSF parameters for this test are given in Table 7 and they are representative for all α Hyi data; ^(c) flux ratio affected by self-subtraction.

of the diffracted light by stopB1_2 a factor of ≈ 1.9 higher than without stop as listed in Table 10 under test A.

4.3. Coronagraphic performance at small inner working angle.

Of great interest is a comparison of the different coronagraphs for the detection and flux measurements of the faint companion to α Hyi separated by 91 mas. Figure 21 shows the innermost region of the images obtained with (a) the small CLC-S-WF mask ($\rho = 46.5$ mas), (b) the medium CLC-MT-WF mask ($\rho = 77.5$ mas), (c) the four quadrant phase mask 4QPM2, and (d) with non-coronagraphic observations. Apart from the mask, the instrument configuration for (a) and (b) is identical. For the non-coronagraphic image the primary star is offset from the focal plane mask (CLC-S-WF) by 550 mas and a ND2-filter is inserted in FW0 to avoid heavy saturation. These three data sets were taken with the I_PRIM filter for cam1 (shown in Fig. 21) and the R_PRIM filter for cam2. For the 4QPM2 images the N_I filter for cam1 and the cnt820 filter for cam2 are used which match the wavelength of the phase mask.

In all these images the faint B component can be recognized, at least if its position is known. As illustrated in Fig. 21(a), the flux f_B is measured in the black aperture with a radius of $r = 7$ pixels, subtracting the background level derived from the mean counts in the surrounding pixel ring with $7 < r < 8$ pix. This result is then corrected by the mean flux in the eleven white (“empty”) apertures at the same separation to account for a possible systematic effect introduced for example by diffraction rings. The standard deviation for the empty apertures is used as

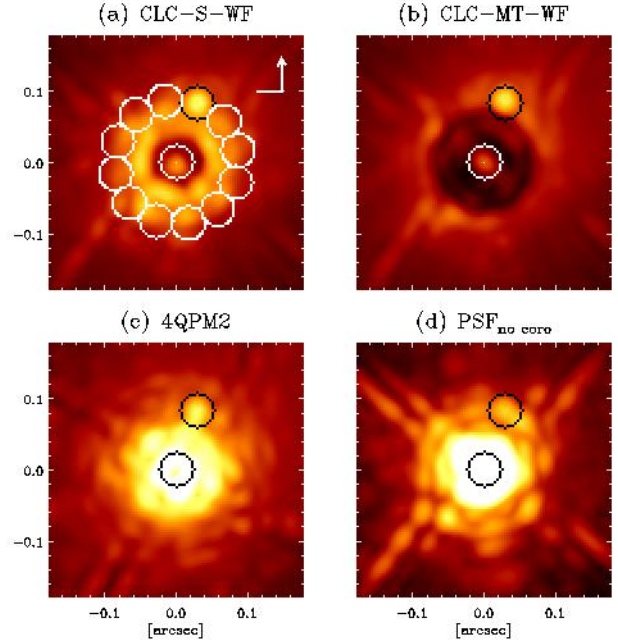


Fig. 21. α Hyi A and B observed in the I_PRIM filter with panel a: small and panel b: medium MT classical Lyot coronagraph, panel d: without coronagraph, while (panel c) was taken in the N_I band filter. and the four quadrant phase mask 4QPM2. The circles are flux apertures for component A (center), component B at $\rho = 91$ mas (black), while (panel a) shows also the concentric comparison apertures. North is up and east to the left.

uncertainty σ_B , and for the signal-to-noise ratio $S/N = f_B/\sigma_B$ given in Table 10. The flux of B is given as ratio f_B/f_A , where f_A is the flux of the primary measured in the non-coronagraphic PSF, scaled with the transmission of the ND2-filter $T_{\text{ND2}} = 0.95\%$, for I_PRIM and 0.73% for R_PRIM.

The measured contrasts f_B/f_A in Table 10 show a clear trend with wavelength, because the faint companion is redder than the primary star. For a given filter, similar ratios f_B/f_A are obtained for the different coronagraphs or instrument configurations and the $(S/N)_B$ -values give a rough measure of the contrast performance. However, because atmospheric seeing conditions and therefore AO performance are variable one should not give too much value on individual measurements.

Table 10 compares under test B the coronagraphic detection performance of CLC-S-WF, CLC-MT-WF, and 4QPM2. For all three coronagraphs the $(S/N)_B$ is about 2.0–2.5 times higher than for non-coronagraphic images taken at the same wavelength. This confirms the results of the coronagraphic test A, which shows that a significant fraction of the diffracted light is suppressed at small separations by the coronagraph.

Overall, the coronagraphic tests B show, that a faint companion at $0.091''$ separation with a contrast $f_B/f_A \approx 0.002 - 0.005$, which is hardly or not visible in non-coronagraphic observations, is clearly detected if a small or medium Lyot coronagraph, or a 4QPM is used.

4.4. High contrast observations and image rotation

Field rotation is a very powerful strategy in high contrast imaging to correct for quasi-static instrumental features in the PSF of the central star. With so-called “roll subtraction” of two or several images taken with different sky orientations the stellar light can be significantly reduced and the companion becomes more

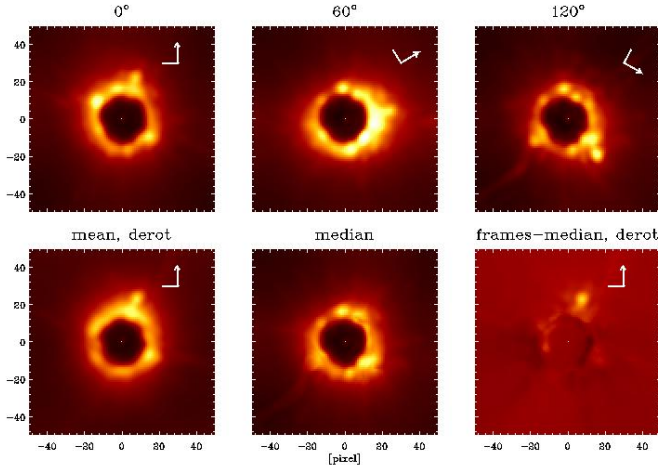


Fig. 22. Coronagraphic images of α Hya taken in the R_PRIM filter, the CLC-S-WF coronagraph and with image rotation 0° , 60° , and 120° (upper row). The lower row shows the mean of the derotated images (left), the median of non-derotated image (middle), and the mean of the rotated difference between non-derotated image and non-derotated median (right) as result of a simple roll-angle angular differential imaging procedure.

apparent (Schneider et al. 2003). Even higher contrast levels can be achieved with angular differential imaging which is based on a large number of frames taken with continuous field rotation, where for each image or image section a reference PSF is subtracted, which is derived from appropriately selected frames (Marois et al. 2006; Lafrenière et al. 2007), or a PSF fitting procedure (Amara & Quanz 2012; Soummer et al. 2012).

Figure 22 shows a very simple test for roll subtraction with SPHERE/ZIMPOL, based on three coronagraphic frames of α Hya taken in field stabilized mode with the different field orientation angles $\delta\theta = 0^\circ$, 60° , and 120° (see Fig. 22). The individual frames show quite strong variations in the relative companion flux f_B/f_A and signal-to-noise $(S/N)_B$ (Table 10, Test C), which are caused by atmospheric changes and the fact that f_A was taken from a non-simultaneous measurement for the f_B/f_A ratio. Derotating and averaging the frames taken with $\delta\theta = 0^\circ$, 60° , and 120° does not enhance much the $(S/N)_B$, most likely because the static noise features from the instrument are added to the mean in three different orientations. Nonetheless, the mean flux ratio f_B/f_A are good flux ratios for the α Hya system in the I_PRIM and R_PRIM band, because these are means based on a total of three minutes of observations.

Roll-subtraction is more efficient in enhancing the contrast performance than simple averaging. For field-stabilized observations, the telescope pupil rotates and therefore the effects fixed to the telescope, like the spider pattern, are not corrected. However, the orientation of the AO system and the coronagraph as seen by the detector remains unchanged in SPHERE/ZIMPOL because the derotator is located further upstream. Figure 22 shows the median image of the three frames taken with $\delta\theta = 0^\circ$, 60° , and 120° , which is then subtracted from all three individual frames and the resulting residual frames are derotated and averaged. Of course, the subtraction of a median image from only 3 frames is only a very basic procedure and the derived flux ratios suffer from self-subtraction effects (Table 10, Test C). However, this example shows that the final S/N-ratio is roughly doubled with respect to an individual image and it reveals in coronagraphic images of SPHERE/ZIMPOL quite a lot of fixed instrumental structures from the AO-system

and the coronagraph, which can be removed with image rotation.

This kind of simple roll-subtraction can be achieved with only several, for example five exposures taken at different field position angles within a few minutes. Much more telescope time is required for higher contrast observations using the field rotation in pupil stabilized mode or fixed derotator mode, because one needs to stay on target for a time of the order of an hour to achieve a sufficient sky rotation for an efficient ADI data reduction.

5. SPHERE/ZIMPOL imaging polarimetry

ZIMPOL-polarimetry is a powerful differential imaging technique for high contrast observations, because the opposite polarization directions are measured simultaneously and with the same detector pixel, that is through almost the same optical path yielding images that are close to identical for an unpolarized source. Therefore, the PSF of a bright, unpolarized central star, including the variable residual AO speckles, is strongly suppressed in the differential signal, and a weak circumstellar polarization signal may become visible in the polarimetric images.

5.1. Intrinsic polarimetric signal from the sky target

The SPHERE/ZIMPOL polarimetric imaging mode determines the linear polarization of a target at each point in the field of view (α, δ) described by the Stokes parameters,

$$Q(\alpha, \delta) = I_0(\alpha, \delta) - I_{90}(\alpha, \delta) \quad \text{and} \quad (11)$$

$$U(\alpha, \delta) = I_{45}(\alpha, \delta) - I_{135}(\alpha, \delta), \quad (12)$$

where the indices of I give the sky orientation for the electric field vector of the photons wave measured from North over East. The polarimetric images Q or U are vector components, unlike the intensity image I , and their signal can contain regions with positive and negative values. Therefore, the measured net signal depends on the spatial resolution of the data, and strong cancellation can occur, if the intrinsic $+Q$ and $-Q$ quadrant pattern from circumstellar scattering is not well resolved (see e.g. Schmid et al. 2006b). A quantitative polarimetric measurement should always consider these cancellation effects because of the limited spatial resolution.

Every polarimetric frame provides also a Stokes I -image or intensity frame which can be reduced and analyzed like “normal” imaging. The intensity is simply the sum of the intensity components, either

$$I_Q(\alpha, \delta) = I_0(\alpha, \delta) + I_{90}(\alpha, \delta) \quad \text{or} \quad (13)$$

$$I_U(\alpha, \delta) = I_{45}(\alpha, \delta) + I_{135}(\alpha, \delta). \quad (14)$$

For a perfect instrument $I_Q = I_U = I$ and any deviations from this equality is a spurious measuring effect.

The ZIMPOL I_Q - and I_U -frames obtained in polarimetric mode contain in principle the same information like the frames taken in imaging mode. The polarimetric I_Q and I_U have some properties which can be beneficial for certain science applications, like:

- a lower read-out noise for the slow polarimetry mode which is particularly suitable for faint sources,
- more accurate absolute and differential (2-channel) photometry, because the photometric throughput depends on instrument polarization effects which are controlled in

polarimetric observations. This is an obvious problem for an Nasmyth instrument, where the Al-coated VLT M3 mirror introduces in the ZIMPOL spectral range about 4% of polarization and where channel splitting is done with a polarization beam splitter.

Other features of the polarimetric mode can be disturbing for high contrast intensity imaging or other high performance applications, in particular:

- the presence of more detector pixel faults, caused by the charge shifting over pixels with non-optimal charge transfer efficiency, requires a more sophisticated observing strategy and data reduction for bad pixel cleaning,
- no pupil-stabilized polarimetry for angular differential imaging (ADI) – instead there exists a static DROT-mode optimized for polarimetry. This provides a rotating field for ADI, but also the pupil is rotating with a rotation rate different to the field and therefore instrument features fixed to the pupil are less well suppressed,
- a reduced throughput ($\approx -15\%$) because of the additional polarimetric components in the beam,
- the presence of a few additional ghost features caused by the polarimetric components.

These drawbacks might be minor when considering that polarimetry provides intensity imaging with comparable quality to “standard” imaging for many applications but delivers in addition a high performance polarization measurement “for free”. Therefore, it is always worthwhile to consider using the polarimetric ZIMPOL mode for intensity imaging and profit from the additional scientific information from the polarimetric signal.

The normalized Stokes parameters Q/I and U/I are important parameters for the characterization of astronomical sources, but also for the determination of instrumental polarization effects from the telescope and the instrument. In SPHERE/ZIMPOL the instrumental polarization is to first order field-independent and lower than $p_{\text{inst}} = (Q_{\text{inst}}^2 + U_{\text{inst}}^2)^{1/2}/I < 1.0\%$ as measured with zero polarization calibration stars (see next sections). In many science cases the central star can be a useful zero polarization calibration source for a correction of the instrumental polarization assuming $Q_{\text{star}}/I = U_{\text{star}}/I = 0$. This is achieved by applying a re-normalization, ensuring that $I_0 = I_{90}$ and $I_{45} = I_{135}$ to the data. If the polarization of the central star is indeed zero then the residual polarization might be produced by a circumstellar polarization component Q_{cs} and U_{cs} . Such self-calibration procedures were often successfully applied to high contrast imaging polarimetry to disentangle the signal of a circumstellar polarization source from the instrumental polarization (e.g. Quanz et al. 2011; Avenhaus et al. 2014). This procedure corrects also for the interstellar polarization produced by the dust along the line of sight. However, an accurate polarimetric measurement remains an issue for self-calibrated data without a detailed assessment of the instrumental polarization effects.

For a weak circumstellar emission of scattered light it is often much easier to measure the differential polarization signal Q_{cs} and U_{cs} than the intrinsic intensity I_{cs} . The measured intensity near a bright star is composed of an intrinsic circumstellar component $I_{\text{cs}}(\alpha, \delta)$ and a dominating and strongly variable component $I_{\text{star}}(\alpha, \delta, t)$ from the halo of the central star

$$I(\alpha, \delta, t) \approx I_{\text{star}}(\alpha, \delta, t) + I_{\text{cs}}(\alpha, \delta). \quad (15)$$

Often, there is $I_{\text{cs}}(\alpha, \delta) \ll I_{\text{star}}(\alpha, \delta)$ and therefore I_{cs} cannot be determined while the differential polarization Q_{cs} and U_{cs} can still be measured. Without $I_{\text{cs}}(\alpha, \delta)$, it is not possible to derive the

fractional polarization $Q_{\text{cs}}(\alpha, \delta)/I_{\text{cs}}(\alpha, \delta)$ and $U_{\text{cs}}(\alpha, \delta)/I_{\text{cs}}(\alpha, \delta)$. For these cases, one can use the polarized surface brightness contrasts $Q_{\text{cs}}(\alpha, \delta)/I_{\text{star}}$ and $U_{\text{cs}}(\alpha, \delta)/I_{\text{star}}$ which relate the measured circumstellar Stokes signals to the total flux of the central star as measured in a large aperture, for example with a diameter of $3''$.

The Stokes fluxes Q and U , and the corresponding fractional Stokes parameters Q/I and U/I or contrast values Q/I_{star} and U/I_{star} , are the two components of a vector quantity, where the linearly polarized flux $P(\alpha, \delta)$, or the corresponding fractional polarization $p(\alpha, \delta)$, is the length of the vector and the polarization position angle $\theta(\alpha, \delta)$ its orientation (measured from N over E):

$$P(\alpha, \delta) = \sqrt{Q^2(\alpha, \delta) + U^2(\alpha, \delta)}, \quad (16)$$

$$\theta(\alpha, \delta) = 0.5 \cdot \text{atan} \left(\frac{U(\alpha, \delta)}{Q(\alpha, \delta)} \right). \quad (17)$$

The polarized flux P and the polarization angle θ are well defined quantities, if the polarization signal P is significantly larger than the noise. For weak Q or U signals the individual pixel values will have positive or negative signs because of the noise in the data. According to the definition of the polarized flux P in Eq. (16) the Q^2 and U^2 terms count “negative noise values” like positive values and a net polarization results even if the mean Q - or U -signals are zero (e.g. Clarke et al. 1983). Therefore, one should use the individual Stokes Q - and U -values and images for the measurement of a weak polarization signal. The determination of the polarized flux P , the fractional polarization $p = P/I$, or the polarization contrast $C_p = P_{\text{cs}}/I_{\text{star}}$ needs to take the bias effect of noisy data into account. For centro-symmetric linear polarization patterns, as expected for example for nearly centro-symmetric and optically thin circumstellar scattering, it can be very useful to define radial or azimuthal Stokes parameters with respect to the central object as proxy for the polarized flux, e.g. $Q_\phi \approx P$, as described in Schmid et al. (2006b).

5.2. Control of the polarimetric signal

ZIMPOL measures according to Sect. 2.2.2 the differential polarimetric signal $P_Z(x, y) = I_\perp(x, y) - I_\parallel(x, y)$ (Eq. (4)) at the position of the polarization modulator. This signal includes the polarization from the sky target, but also the polarization effects introduced by the telescope and the SPHERE/ZIMPOL instrument. The system concept needs to control the polarization, so that the initial sky target signal can be reconstructed from the measurements taken with different HWP2 orientations i

$$P_{i=1,2,\dots}^Z(x, y) \rightarrow Q(\alpha, \delta) \text{ and } U(\alpha, \delta) \quad (18)$$

using appropriate calibrations.

The polarimetric concept of SPHERE/ZIMPOL is complex, because the instrument is fixed to the VLT Nasmyth platform. The strongly inclined M3 mirror of the telescope introduces already at the telescope focus a strong telescope polarization $I \rightarrow Q$ and polarization cross talks $U \leftrightarrow V$ (see Tinbergen 2007). In addition there is an image derotator in SPHERE, which introduces similarly strong polarization effects.

For this reason, SPHERE/ZIMPOL uses an innovative concept which compensates and controls the instrumental polarization of the telescope and instrument with four steps.

1. The M3 mirror of the VLT UT3 telescope has an incidence angle of 45° and an Al-coating which produces in the 500–900 nm range a polarization of about 3–5% and a strong $U \rightarrow V$ polarization cross talk. This polarization is

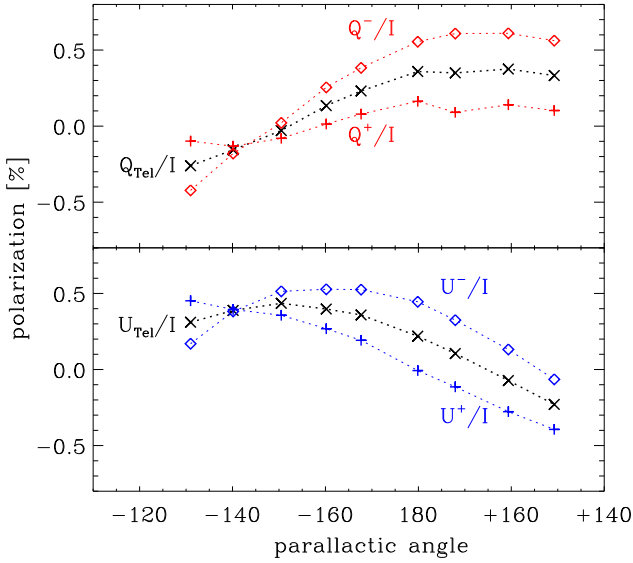


Fig. 23. Residual telescope polarization $q_{\text{tel}} = Q_{\text{tel}}/I$ and $u_{\text{tel}} = U_{\text{tel}}/I$ as function of parallactic angle for the unpolarized star ϵ Eri in the VBB filter. Also shown are the measurements q^+ , q^- , u^+ , and u^- of a polarimetric cycle, which include instrument polarization component $\pm p_{\text{SZ}}$ for the P2-mode and a field position angle offset of 60° .

compensated with the rotatable, achromatic half-wave plate HWP1 and the following first mirror (PTTM) which has also an incidence angle of 45° and a similar Al-coating. HWP1 has an altitude a dependent orientation $\theta_{\text{HWP1}} = a/2 + 45^\circ$, which switches the M3 polarization effects into a direction, like for a M3 mirror pointing in zenith direction. The following PTTM mirror acts then like a crossed mirror and compensates the M3 polarization effects to significantly smaller values, for the three components M3-HWP1-PTTM (Joos 2007). Figure 23 shows for the unpolarized star ϵ Eri the residual fractional telescope polarization $q_{\text{tel}} = Q_{\text{tel}}/I$ and $u_{\text{tel}} = U_{\text{tel}}/I$ after M3-HWP1-PTTM. Hereafter, we call this also the telescope polarization because it is fixed to the telescope and therefore changes with the parallactic angle θ_{para} . The telescope polarization can be corrected with calibrations of zero polarization standard stars (see Sect. 5.3.1). A polarization compensation with a crossed-mirror was already described by Cox (1976) for an instrument fixed to the telescope tube, while Martinez Pillet & Sanchez Almeida (1991) included also a rotating half-wave plate for narrow-band applications with a Coudé-focus instrument for solar physics. SPHERE/ZIMPOL introduces now this approach for broad-band, high contrast imaging polarimetry for an Nasmyth instrument at a stellar telescope (see also Tinbergen 2007).

2. The fractional Stokes parameters for the instrument polarization of SPHERE/ZIMPOL q_{SZ} and u_{SZ} includes all components after the PTTM in CPI (Fig. 1) up to the ZIMPOL polarization modulator. This polarization is compensated with a measuring procedure, where HWP2 is used as Q^+ , Q^- , or U^+ , U^- polarization switch by applying to the HWP2 position angle an offset cycle of 0° and 45° , or 22.5° and 67.5° , respectively. The 45° offset, or Q^- switch, reverses the sign of the target and telescope polarization $Q + q_{\text{tel}}I$, with respect to the Q^+ offset position, while the polarization effects introduced by the following components $q_{\text{SZ}}I$ and $u_{\text{SZ}}I$ are unchanged. Subtracting the Q^- from the Q^+ measurement cancels q_{SZ} after HWP2 and only $Q + q_{\text{tel}}I$

remains

$$\begin{aligned} Q^+ - Q^- &= [(Q + q_{\text{tel}}I) + q_{\text{SZ}}I] - [-(Q + q_{\text{tel}}I) + q_{\text{SZ}}I] \\ &= 2(Q + q_{\text{tel}}I). \end{aligned} \quad (19)$$

and similar for the U polarization component. The polarization switch is a well known technique to compensate instrumental polarization to first order (e.g. Appenzeller 1968; Kemp & Barbour 1981; Scarrott et al. 1983) and Fig. 23 gives an example for SPHERE/ZIMPOL for the unpolarized star ϵ Eri with an intrinsic polarization Q/I and $U/I < 0.001$ (Tinbergen 1979). It is important to locate the HWP-switch as early as possible in the beam for keeping the non-compensated instrumental polarization q_{tel} and u_{tel} introduced in front of the switch simple and easy to determine.

3. The derotator DROT in SPHERE, a three mirror system with inclinations angles of 55° , 10° , and 55° , is a very critical component for polarimetric measurements because it introduces an instrument polarization (diattenuation) $I \rightarrow Q$ of $m_{21} \approx 0.03$, and strongly wavelength dependent polarization cross talks $U \leftrightarrow V$, which can be larger than $|m_{34}| > 0.5$. To minimize the cross talk effects the linear polarization direction to be measured by ZIMPOL is rotated by HWP2 into the I_\perp and I_\parallel orientation θ_{DROT} . This requires, that the HWP2 tracking law considers the rotation of e.g. the I_0 sky orientation, compensates at the same time for the rotation effect of HWP1, and rotates the I_0 direction into the I_\perp orientation of DROT depending on the derotator law. DROT can either be in a fixed orientation for P1-mode, $\theta_{\text{DROT}} = 90^\circ$ or it moves like $\theta_{\text{DROT}} = 0.5(\text{alt} - \theta_{\text{para}})$ to stabilize the image on the detector in P2-mode. In these relation one must consider the 180° angle periodicity of θ_{DROT} for the image orientation.
 4. The derotator polarization of about $p_{\text{DROT}} \approx 3\%$ is corrected with the polarization compensator PCOMP, an uncoated, co-rotating, inclined glass plate in ZIMPOL. This plate deflects more of the I_\perp -component than the I_\parallel -component, so that $I_\perp - I_\parallel$ is reduced in the transmitted beam (Sect. 2.2.3). For an inclination of 25° , the current value used for PCOMP, the derotator polarization and other minor contributions from other components are reduced to about 0.3%.
- In field-stabilized polarimetric imaging, or P2-mode, DROT is not aligned with the orientation θ_Z of the ZIMPOL polarimeter. Therefore, a rotatable half-wave plate within ZIMPOL (HWPZ), with an orientation $\theta_{\text{HWPZ}} = \theta_{\text{DROT}}/2$, is used to switch the polarization to be measured into the θ_Z -orientation. For P1-mode, the directions of θ_{DROT} and θ_Z are identical and therefore HWPZ is not in the beam. The instrument polarization is essentially the same for the Q and U measurements, or $q_{\text{SZ}} \approx u_{\text{SZ}}$. (see Fig. 23), because the control of the polarization directions is the same after HWP2. Typical values are $|q_{\text{SZ}}|, |u_{\text{SZ}}| \lesssim 0.3\%$ for e.g. the V, N_R, N_I, or VBB-filters.

5.3. Calibrations for the polarimetric measurements

The polarimetric measuring strategy includes four calibration steps:

- c1 is the correction for the ZIMPOL modulation-demodulation efficiency ϵ_{mod} as described in Sect. 2.3.3 (Table 5). For the determination of the fractional polarization in a large aperture also the frame transfer effect or ϵ_{ft} (Eq. (6)) needs to be considered. The calibration factors ϵ_{mod} are obtained with a fully polarized illumination using the internal flat field source and the polarizer in FW0.

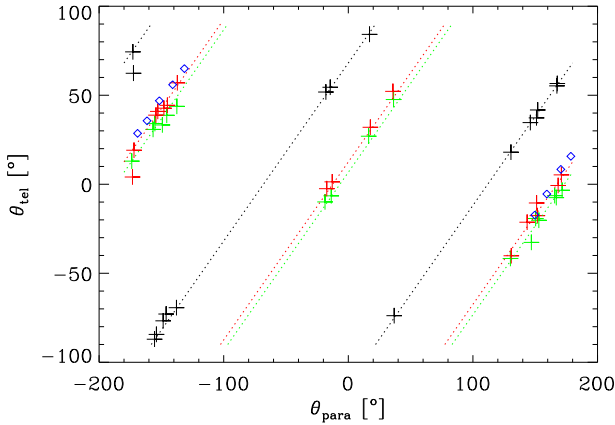


Fig. 24. Telescope polarization angle θ_{tel} as function of the parallactic angle for zero-polarization standard stars measured in the filters V (green), N_R (red), and N_I (black) with dotted lines for the best fits according to Eq. (20). Blue diamonds are the VBB-filter data from Fig. 23.

- c2 is the subtraction of the telescope polarization which depends on pointing direction and filter. The telescope polarization p_{tel} and θ_{tel} is determined with zero-polarization standard star calibrations.
- c3 is a small correction for the polarization efficiency loss of the telescope mirrors M1 and M2 and that part (residual polarization cross talk) of the M3-HWP1-PTTM configuration, which is not included in the modulation-demodulation efficiency calibration ϵ_{mod} . The effect is small with a correction factor close to one, which can be checked with high-polarization standard star calibrations.
- c4 is a position angle offset correction for the effective HWP2 plate orientation to adjust the measured Q , U parameters to the North direction on sky. This polarization angle offset δ_{SZ} depends slightly on wavelengths and is also calibrated with the high-polarization standard stars.

The calibrations c1 and c2 are very important for all quantitative polarimetric measurements. The corrections or adjustments c3 for ϵ_{opt} and c4 for δ_{SZ} are only relevant for high signal-to-noise polarimetry $S/N = p/\Delta p \gtrsim 20$. However, all calibrations are essential for checking the proper working of the instrument and one should be alarmed if unexpected calibration results are obtained.

5.3.1. Calibration of the telescope polarization

The “residual” telescope polarization is regularly measured with zero-polarization standard stars ($p_{0\text{pol}} \ll 0.1\%$), as part of the ESO SPHERE instrument calibration plan. We use bright, nearby, single solar type stars, preferentially from the lists of [Serkowski et al. \(1974\)](#) or [Tinbergen \(1979\)](#). These measurements consist typically of one full polarimetric cycle for each of the three filters V, N_R, and N_I in FW1 and FW2. Often ND-filters are used in FW0 in order to avoid saturation. All these calibration data are available in the ESO archive.

For the analysis the measurements are bias subtracted and corrected for the modulation-demodulation efficiencies ϵ_{mod} and the frame transfer effect ϵ_{ft} . Integrated fluxes Q , U and I_Q , I_U are determined for synthetic apertures and fractional telescope polarization parameters $q_{\text{tel}} = Q/I_Q$, $u_{\text{tel}} = U/I_U$, p_{tel} and the position angle θ_{tel} is calculated.

We have analyzed all useful zero-polarization standard star calibrations from 2015, which include 17 measurements for each

Table 11. Residual telescope polarization p_{tel} and θ_{tel} for the filters V, N_R, and N_I as measured from the standard star measurements taken in 2015 and the VBB filter measurements of ϵ Eri (Figs. 23 and 24).

Filter (F)	λ_c (nm)	n_{cal}	p_{tel} (%)	σ_p (%)	δ_{tel} (°)	σ_δ (°)
Zero-polarization standard stars						
V	554	17	0.57	± 0.03	6.7	± 3.2
N_R	646	17	0.55	± 0.04	12.6	± 3.6
N_I	817	17	0.42	± 0.04	68.1	± 3.8
ζ Tuc						
V_S	532	1	0.53		5.8	
V	554	1	0.52		7.8	
V_L	582	1	0.49		11.1	
N_R	646	1	0.53		10.1	
NB730	733	1	0.46		16.9	
N_I	817	1	0.44		71.5	
I_L	871	1	0.52		72.1	
ϵ Eri						
VBB	735	9	0.41	± 0.02	16.7	± 1.6

of the three filters V, N_R, and N_I. The derived telescope polarization values are in the range $p_{\text{tel}} = 0.4 - 0.6\%$ with a scatter of only $\sigma_p \approx 0.04\%$ for a given filter. As shown in Fig. 24 the polarization position angle θ_{tel} is proportional to the parallactic angle θ_{para} with a wavelength dependent offset $\delta_{\text{tel}}(\lambda_c)$

$$\theta_{\text{tel}}(\theta_{\text{para}}, \lambda_c) = \theta_{\text{para}} + \delta_{\text{tel}}(\lambda_c), \quad (20)$$

where one must consider the 180° polarization angle periodicity. Table 11 lists for the zero-polarization standard stars the mean polarization p_{tel} and standard deviation σ_p , and the mean position angle offset δ and σ_θ from the best fit (Eq. (20)) also plotted in Fig. 24. The correlation between θ_{tel} and θ_{para} is expected because the compensation of the M3 mirror polarization with the HWP1 – PTTM combination yields residuals which are to first order fixed to the telescope pupil. This effect is also nicely seen in Fig. 23 for the long data series of the unpolarized star ϵ Eri taken in Nov. 2016.

Table 11 gives additional measurements for the wavelength dependence of $p_{\text{tel}}(\lambda_c)$, $\delta_{\text{tel}}(\lambda_c)$ based on multifilter data of ζ Tuc (HR 77) taken during SPHERE commissioning in Oct. 2014. The color dependence of p_{tel} and δ_{tel} can be explained by differences in the M3 and PTTM mirror coatings and some deviations of HWP1 from a perfect, broad-band half wave plate. The strong rotation of δ_{tel} in the I-band is probably related to the well known reflectivity minimum of Al-coatings in this wavelength range. One might expect a slow temporal evolution of the telescope polarization because of the aging of the mirror coatings and perhaps a sudden change associated with the M1 and M3 telescope mirror re-coating, which took place in April 2017.

Measurements of the fractional polarization Q_{c1}/I and U_{c1}/I of standard stars, can now be corrected for the telescope polarization according to

$$Q_{c2}/I = Q_{c1}/I - p_{\text{tel}} \cos(2(\theta_{\text{para}} + \delta_{\text{tel}})) \quad (21)$$

$$U_{c2}/I = U_{c1}/I - p_{\text{tel}} \sin(2(\theta_{\text{para}} + \delta_{\text{tel}})). \quad (22)$$

The parameters p_{tel} and δ_{tel} from Table 11 can be used for all observations from 2015 and possibly also for later observations. One should notice that the corrected values Q_{c1}/I and U_{c1}/I for the standard star polarization parameters derived in large apertures must use the factors $\epsilon_{\text{mod}}\epsilon_{\text{ft}}$ including the frame transfer smearing effect (Table 5).

Table 12. Measured and corrected polarization p_c [%] and θ_c [°] of high-polarization standard stars and comparisons with literature values p_ℓ, θ_ℓ .

	V		N_R		N_I	
	$p_{c,\ell}$	$\theta_{c,\ell}$	$p_{c,\ell}$	$\theta_{c,\ell}$	$p_{c,\ell}$	$\theta_{c,\ell}$
HD 79186, nobs = 1						
meas	2.75	51.1	2.58	52.1	2.18	52.5
lit [1]	2.59	47.7	2.40	48.4		(48.4)
$p_c/p_\ell, \Delta\theta_{c-\ell}$	1.06	+3.4	1.07	+3.7		(+4.1)
HD 98143, nobs = 2						
meas	7.90	135.6	7.95	137.1	7.29	137.1
lit [2]	8.03	133	8.04	130	7.10	130
$p_c/p_\ell, \Delta\theta_{c-\ell}$	0.98	+2.6	0.99	+7.1	1.03	+7.1
HD 111613, nobs = 1						
meas	3.20	79.1	3.08	84.0	2.77	86.8
lit [1]	3.10	81.1	3.10	80.4		(80.4)
$p_c/p_\ell, \Delta\theta_{c-\ell}$	1.03	-2.0	0.99	+3.6		(+6.4)
HD 147084, nobs = 1						
meas			4.37	36.1		
lit [1,3,4]	4.15	31.7	4.44	32.2	4.40	31.5
$p_c/p_\ell, \Delta\theta_{c-\ell}$			0.98	+3.9		
HD 154445, nobs = 2						
meas	3.60	91.6	3.47	94.7	2.98	96.1
lit [1,3,4]	3.72	89.9	3.63	89.5	3.29	90.5
$p_c/p_\ell, \Delta\theta_{c-\ell}$	0.97	+1.7	0.96	+5.2	0.91	+5.6
HD 183143, nobs = 4						
meas	5.45	1.1	5.41	2.6	4.78	4.8
lit [1,3,4]	6.15	179.2	5.81	178.9	5.36	179.0
$p_c/p_\ell, \Delta\theta_{c-\ell}$	0.89	+1.9	0.93	+3.7	0.89	+5.8
<i>mean values</i>						
$\langle p_c/p_\ell \rangle$	0.99		0.99		0.94	
$\langle \Delta\theta_{c-\ell} \rangle$		+1.5		+4.5		+5.8
$\sigma [\pm]$	0.07	2.1	0.05	1.4	0.08	1.1

Notes. The data are corrected for the modulation efficiency ϵ_{mod} , the frame transfer smearing ϵ_{ft} and the telescope polarization. Literature values: 1: *Serkowski et al. (1975)* for V- and R-band, $\theta(R)$ adopted also for $\theta(I)$; 2: *Whittet et al. (1992)*; 3: *Hsu & Breger (1982)* with $0.75 \mu\text{m}$ band values extrapolated to N_I-band ($0.82 \mu\text{m}$); 4: *Bailey & Hough (1982)*.

5.3.2. Calibration of the polarization angle and efficiency

Also high-polarization standard star measurements are taken regularly in the V, N_R, and N_I filter as part of the ZIMPOL calibration plan. These data provide an independent test for the corrections c1 and c2. For our analysis all well illuminated high polarization standard star calibrations from 2015 are included. The measurements and data reduction of high-polarization stars are identical to the zero-polarization standards described above.

Table 12 lists the obtained polarization values for the standard stars, after applying corrections c1 and c2, and compares them to literature values. Figure 25 shows the data for the N_R-filter in the $Q/I - U/I$ -plane with black symbols for c1 corrected values, and red symbols with the additional telescope correction c2 applied. The literature values are given in blue. Also shown are the 17 N_R zero-polarization standard star data from the previous section located on a ring with radius $r \approx 0.5\%$, and the telescope corrected red points are clustered near the zero point with a small scatter of $\sigma_p = 0.12\%$. A similar pattern of black points surrounding the telescope corrected red values is also present for the high-polarization standard HD 183143.

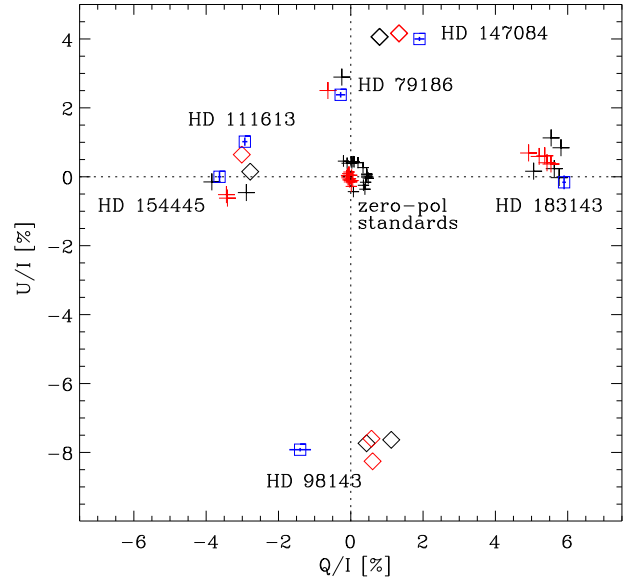


Fig. 25. Polarization of high polarization standard stars for the N_R filter: black symbols give efficiency or c1 corrected values while red symbols are also corrected for the telescope polarization (c2-correction). For individual targets, either plus-signs or diamonds are used in order to avoid confusion. Corresponding literature values are plotted as blue squares with error bars. Also included are the zero-polarization standard stars from the previous subsection.

The derived polarizations (red symbols in Fig. 25) for the high-polarization stars are slightly offset or rotated in counter-clockwise direction when compared to the literature values of high polarization stars. This is summarized in Table 12, which compares for all three filter V, N_R and N_I the ratio p_c/p_ℓ between the measured polarization p_c and the literature value p_ℓ , and the difference $\Delta\theta_{c-\ell} = \theta_c - \theta_\ell$ between the derived polarization angle θ_c and the corresponding literature value θ_ℓ . The measurements were first corrected for the modulation efficiency and frame transfer smearing $\epsilon_{\text{mod}}\epsilon_{\text{ft}}$ (Eq. (7)) and the telescope polarization (Eqs. (21) and (22)). The bottom rows give as final result for each filter the average ratio $\langle p_c/p_\ell \rangle$ and the average angle difference $\langle \Delta\theta_{c-\ell} \rangle$ for the ZIMPOL V, N_R, and N_I filters. The average ratios $\langle p_c/p_\ell \rangle$ are compatible with 1, while $\langle \Delta\theta_{c-\ell} \rangle$ indicates at least for the N_R and N_I filters significant polarization angle offsets δ_{SZ} for SPHERE/ZIMPOL.

The results of the high polarization standard star measurements should be considered as preliminary values. For HD 183143 it is clearly visible, that the scatter of $\sigma_p = 0.52\%$ for the red corrected points in Fig. 25 is significantly larger than the $\sigma_p = 0.12\%$ for the zero-polarization standard stars.

Several effects contribute to this enhanced scatter in the high polarization standard star data. First, there could be instrumental cross talk effects $Q \rightarrow U, V$ or $U \rightarrow Q, V$, which may depend on instrument configuration, and become apparent for objects like HD 183143 with a high linear polarization $p_{\text{star}} \approx 5\%$. Because these cross talks scale with p , they are much smaller for the zero-polarization standard stars. Second, the standard star measurements could be improved. They are not taken in a homogeneous way and would require a study on its own to minimize systematic measuring effects, e.g. differences between strongly and weakly illuminated data. Third, the polarization of the high polarization standard stars could be variable, and HD 183143 is apparently such a case (*Hsu & Breger 1982*). Achieving a smaller uncertainty $\Delta p < 0.5\%$ in absolute polarimetric measurements of high polarization target with ZIMPOL is certainly possible

but requires but requires an extensive analysis of data from well suited calibration targets which is beyond the scope of this paper.

We summarize here briefly the status of bright high polarization standard stars suitable for the calibration of ZIMPOL observations. Only the more northern $\delta > -30^\circ$ objects HD 147084 and HD 154445 were established as good calibration stars by Hsu & Breger (1982), and their values are in good agreement $\Delta p \approx \pm 0.1\%$, $\Delta\theta \approx \pm 1^\circ$ with Bailey & Hough (1982), and Serkowski et al. (1975). As mentioned above HD 183143 is known to show some polarimetric variability (Hsu & Breger 1982) and the same is true for several other high polarization standard stars (Bastien et al. 1988, 2007). The situation is even worse for the southern Milky Way $\delta < -30^\circ$, because there exist essentially no well established bright high polarization standard stars suitable for SPHERE/ZIMPOL. The used objects HD 79186, HD 98143, and HD 111613 have been measured polarimetrically (Serkowski et al. 1975; Whittet et al. 1992), but the accuracy of the published values is unclear and the absence or the level of polarimetric variability has not been investigated.

5.3.3. Recommended polarimetric correction formulae

The full correction of the measured Q and U signals of a science target requires two steps: first the corrections $c1$ for the modulation efficiency ϵ_{mod} , $c2$ for the telescope polarization, and $c3$ for a small efficiency loss because of the optical components:

$$Q_{c3} = \left(\frac{1}{\epsilon_{\text{mod}}} Q - I p_{\text{tel}}(\lambda_c) \cos(2(\theta_{\text{para}} + \delta_{\text{tel}}(\lambda_c))) \right) \frac{1}{\epsilon_{\text{opt}}}, \quad (23)$$

$$U_{c3} = \left(\frac{1}{\epsilon_{\text{mod}}} U - I p_{\text{tel}}(\lambda_c) \sin(2(\theta_{\text{para}} + \delta_{\text{tel}}(\lambda_c))) \right) \frac{1}{\epsilon_{\text{opt}}}. \quad (24)$$

Note, that the polarization flux parameters Q and U are not affected by the intensity dilution during the frame transfer, and therefore ϵ_{ft} is not considered.

In a second step the obtained values Q_{c3} and U_{c3} are then rotated ‘‘polarimetrically’’ to correct for the polarization angle offset of a few degrees,

$$Q_{c4} = Q_{c3} \cos(2\delta_{\text{SZ}}) + U_{c3} \sin(2\delta_{\text{SZ}}), \quad (25)$$

$$U_{c4} = U_{c3} \cos(2\delta_{\text{SZ}}) - Q_{c3} \sin(2\delta_{\text{SZ}}). \quad (26)$$

Most important are the corrections $c1$ and $c2$ for the modulation efficiency $\epsilon_{\text{mod}} = 0.75 - 0.91$, which depends on instrument parameters, and the additive telescope polarization $\Delta(Q/I), \Delta(U/I) \approx -0.6$ to $+0.6\%$. The corresponding parameters ϵ_{mod} are given in Table 5 and $p_{\text{tel}}(\lambda_c)$ and $\delta(\lambda_c)$ for the telescope polarization are listed in Table 11. The corrections $c3$ and $c4$ for the optical efficiency ϵ_{opt} and the position angle offset δ_{SZ} are only important for strongly polarized objects $Q/I, U/I \gtrsim 2\%$ which can be measured with a high polarimetric signal-to-noise $S/N = \Delta p/p \gtrsim 20$. The value ϵ_{opt} and $\delta_{\text{SZ}}(\lambda)$ have not been determined yet with high precision and we recommend a value of $\epsilon_{\text{opt}} = 1/\langle p_c/p_\ell \rangle = 0.98^{+0.02}_{-0.06}$ and $\delta_{\text{SZ}}(\lambda) = \langle \Delta\theta_{c-\ell} \rangle$ according to Table 12.

We think that SPHERE/ZIMPOL provides a substantial progress in quantitative polarimetry for AO assisted, high resolution observations because the instrument polarization effects are well controlled and calibrated with accurate standard star measurements. Therefore, quantitative measurements can also be obtained for weak, non-axisymmetric and other demanding targets. Infrared instruments, like SPHERE/IRDIS (Langlois et al. 2014; van Holstein et al. 2010) and GPI (Perrin et al. 2015) provide also calibrated polarization measurements so that

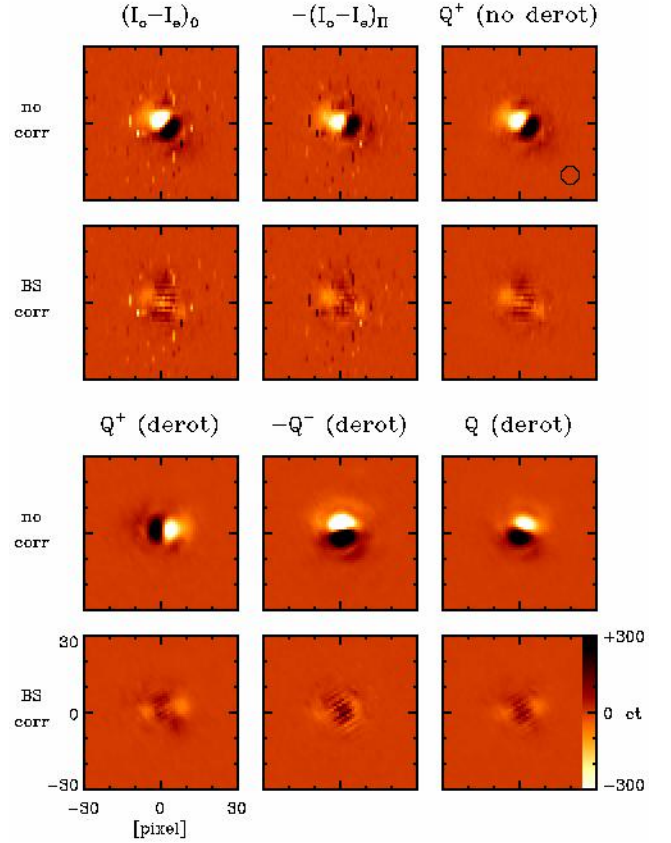


Fig. 26. Observed polarimetric beamshift for a stellar PSF of α Cen B taken in June 2016 with the VBB and ND4 filters: The *first row* shows two consecutive polarization frames $(I_o - I_e)_0$ and $(I_o - I_e)_\pi$ taken with opposite, zero and pi demodulation phase shifts and the resulting, charge-trap corrected, Q^+ -frame. The *third row* illustrates the beamshift for the derotated Q^+ , Q^- , and the final ‘‘science’’ Q -image. The *second* and *bottom rows* show the same but with the beamshifts corrected between the odd-row I_o and even-row I_e sub-frames.

the diagnostic potential of multi-wavelength polarimetry can be exploited.

5.4. Differential polarimetric beam shifts

An important requirement for the performance of a high-contrast, differential polarimetric imager are small aberrations between the measured I_\perp and I_\parallel images. In ZIMPOL, these two polarization modes are registered with the same detector pixels between I_\perp and I_\parallel can be produced by non-perfect half-wave plates and this was considered in the ZIMPOL design. During instrument tests small beam shifts from the modulator assembly were measured, but they were less than 0.1 pixels (< 0.4 mas) and considered to be acceptable (see Roelfsema et al. 2010).

Unfortunately, we detected after the integration of ZIMPOL into SPHERE a substantially larger and unexpected beam shifts of up to 0.3 pixels (or ≈ 1 mas) between I_\perp and I_\parallel caused by the inclined mirrors in CPI. These differential polarimetric beam shifts are apparent in Q or U images as systematic positive and negative features on opposite sides of a stellar PSF (see Fig. 26) and this affects the speckle suppression capabilities of the polarimetric mode. This subsection outlines the origin of this effect, illustrates the impact, and gives a recipe for correcting the effect.

5.4.1. Polarization aberrations from inclined mirrors

Extensive SPHERE/ZIMPOL testing showed that the main contributions to the differential polarimetric beam shifts are caused by the strongly inclined mirrors M3 of the telescope, the 45° pupil tip-tilt mirror (PTTM), and the image derotator mirrors, while the half wave plates are at most minor contributors.

PSF shifts between I_{\perp} and I_{\parallel} are introduced by inclined metallic mirrors because the Fresnel coefficients for the phase shift are different for I_{\perp} and I_{\parallel} as described by Breckinridge et al. (2015) in a comprehensive analysis of polarimetric aberrations of telescopes. The same type of beam shifts causing deviations from the law of geometric optics on sub-wavelength scales are also known in optics as Goos-Hähnchen (GH) and Imbert-Fedorov shifts (e.g. Aiello et al. 2009; Bliokh & Aiello 2013). These shifts are not well known for astronomical instruments, because the spatial resolution or/and polarimetric sensitivity of previous instruments did not achieve the SPHERE/ZIMPOL performance. Therefore, we describe here the dominant effect and provide a simple calculation for the expected PSF shift.

A beamshift between the two polarization components I_{\perp} and I_{\parallel} reflected from an inclined surface was first described by Goos & Hänchen (1947). The reflected I_{\perp} and I_{\parallel} components are shifted as expected for slightly offset “effective” mirror surfaces for the I_{\perp} and I_{\parallel} components. This is illustrated in Fig. 27 with a simplified ray model for the principal beam (solid black, blue and red line with arrows) for two hugely exaggerated offsets for the “effective” mirror surfaces. The induced beam displacements are attributed to the phase shifts ϕ introduced in the reflection, which depend on inclination angle θ . As shown by Artmann (1948) with an angular spectrum decomposition and interference for a spatially limited beam, the incidence angles of the incoming wave sections vary around the incidence angle θ_0 and therefore the waves receive an angle dependent phase shift in the reflection. This explains a spatial Goos-Hähnchen shift Δ , which is proportional to the phase shift gradient $d\phi/d\theta$

$$\Delta_{\perp,\parallel} = -\frac{\lambda}{2\pi} \frac{d\phi_{\perp,\parallel}}{d\theta} \Big|_{\theta_0}. \quad (27)$$

For metallic mirrors, positive and negative shifts are introduced for I_{\perp} and I_{\parallel} , respectively, because $d\phi_{\perp}/d\theta$ and $d\phi_{\parallel}/d\theta$ have opposite signs. There exists also a transverse beam-shift, called spatial Imbert-Fedorov shift (e.g. Bliokh & Aiello 2013), which is also of some importance. The so-called angular shifts, another type of the beam-shifts caused by the angle dependent reflectivity of metallic mirrors, are not relevant for the image position in a focussed beam. It is beyond the scope of this paper to describe here in detail all these effects.

The beam shift can also be explained for a “macroscopic” view of the converging beam of a Nasmyth telescope with an inclined mirror M3 as sketched for the propagation of the wavefronts in Fig. 27, and described in more detail in Breckinridge et al. (2015). In this case, the angles of incidence θ on M3 are different, $45^\circ + \epsilon$ and $45^\circ - \epsilon$, for the “left” and “right” sections of the incoming spherical wave fronts in Fig. 27. Consequently, also the phase shift introduced by the reflection is different $\phi(45^\circ + \epsilon)$ and $\phi(45^\circ - \epsilon)$, so that the interfering spherical wave sections converge along a slightly different angle, when compared to the angle predicted by geometric optics. When neglecting higher order terms, then the estimated focal point shift is about

$$\Theta_{\perp,\parallel} \approx \frac{\lambda}{2\pi} \frac{d\phi_{\perp,\parallel}}{d\theta} \Big|_{\theta_0} \frac{1}{F\#} \frac{1}{D} = \frac{\lambda}{2\pi} \frac{d\phi_{\perp,\parallel}}{d\theta} \Big|_{\theta_0} \frac{1}{f}, \quad (28)$$

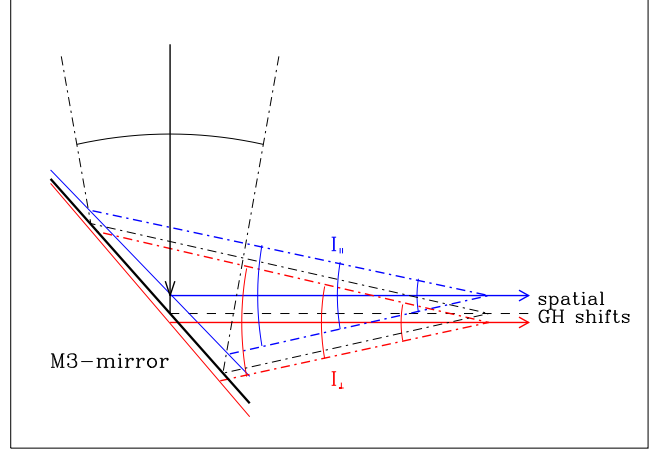


Fig. 27. Schematic and simplified illustration of the polarimetric beam shift effects for the M3 Nasmyth mirror. The incoming beam and the expected reflection according to geometric optics are plotted in black. The beam and wavefront displacements for I_{\perp} and I_{\parallel} caused by the phase shifts, with the corresponding “effective” mirror surface location and tilts, are hugely exaggerated and drawn in red and blue respectively.

where $F\# = f/D$ is the F -ratio for the converging or diverging beam, and $1/F\#$ the corresponding angular spread for the focused beam. Because the phase shifts gradients $d\phi/d\theta$ are different and have even different signs for I_{\perp} and I_{\parallel} for metallic surfaces also positive and negative focal point shifts Θ_{\perp} and Θ_{\parallel} result (Fig. 27). The focal point shifts are proportional to the inverse of the focal length f and therefore the focus displacement expressed in nm in the focal plane does not depend on the telescope size and is just given (to first order) by the phase shift gradient of the mirror coating for the incidence angle θ_0

$$\Delta_{\perp,\parallel} = f \cdot \Theta_{\perp,\parallel} = \frac{\lambda}{2\pi} \frac{d\phi_{\perp,\parallel}}{d\theta} \Big|_{\theta_0}.$$

This is the same result as in Eq. (27), because both, a narrow beam and a macroscopic telescope beam are made of an angular spectrum of plane-parallel wavefronts impinging onto an inclined mirror.

The PSF-shifts $\Delta_{\perp,\parallel}$ do not depend on the F -ratio, the focal lengths, or the aperture diameter of the focussed beam, but only on θ_0 and the mirror surface. For an Al-mirror and $\lambda = 800$ nm the phase shift gradients is in units of wavelength per radian

$$\frac{d\phi_{\perp}}{d\theta} \Big|_{45^\circ} = 0.151 \quad \text{and} \quad \frac{d\phi_{\parallel}}{d\theta} \Big|_{45^\circ} = -0.299.$$

Multiplication with $\lambda/2\pi$ yields then the PSF-shifts 19.2 nm and -38.1 nm in the focal plane, respectively, and the differential PSF shift of

$$\Delta_{\perp} - \Delta_{\parallel} = 57.3 \text{ nm}.$$

For a telescope with the focal length of the VLT ($f = 120$ m) this differential PSF shift in the focal plane corresponding to an angle shift of $\Theta_{\perp} - \Theta_{\parallel} = 0.101$ mas on sky. The derived shift of 57.3 nm agrees with the result of Breckinridge et al. (2015, Table 2), who obtained for the same λ , θ_0 and mirror surface a focal point shift of $\Theta_{\perp} - \Theta_{\parallel} = 0.625$ mas ($= 3.15 \times 10^{-9}$ rad) for a telescope with $f = 19.2$ m. This is essentially the same shift $\Delta_{\perp} - \Delta_{\parallel} = 60.5$ nm as calculated for the VLT, considering that the used $d\phi_{\perp,\parallel}/d\theta$ -values used by us could be slightly different.

The same principles for polarimetric beam shifts apply for all inclined mirror in a converging or diverging beam. This are the

Al-coated M3 mirror of the telescope, the Al-coated 45° pupil tip-tilt mirror (PTTM), and the image derotator mirrors. The beam-shift introduced by the PTTM is essentially the same as for M3, except for the different mirror orientation. Our measurements show that the derotator is the dominant component for the beam shift in the *I*- and *R*-band range, while the shift in the *V*-band is comparable to the M3 mirror. The strong effect from the derotator is not surprising, because it consists of three mirrors, two 55°-mirrors and one 20°-mirror and the shifts of the two 55°-mirrors add up. They have overcoated silver surfaces and the strong wavelength dependence for the beam shift is probably caused by this type of reflecting surface, for which we do not know the $d\phi/d\theta$ phase shift properties.

5.4.2. Correction of the polarimetric beam shift

The SPHERE/ZIMPOL beam shifts are the results of a complex combination of several contributing components, mainly the inclined M3 mirror of the VLT, the 45° PTTM mirror, and the three mirrors in the image derotator. Moreover, the half wave plates HWP1, HWP2 and HWPZ rotate the polarization angle of the shifted components at different locations along the light paths. Several of these components rotate during the observations and therefore each exposure requires an “individual” correction which is only valid for a given sky position and instrument configuration. In particular, the beam shifts for the four exposures of a polarimetric cycle Q^+ , Q^- , U^+ and U^- are all different (see Q^+ and Q^- in Fig. 26). Another significant complication is that the beamshift from the derotator is strongly wavelength dependent with a large, ≈ 1 mas shift, in the *I*-band, about 0.5 mas in the *R*-band and less in the *V*-band. Because of this complexity, there exists up to now no instrument model for the correction of the differential beam shifts.

However, a beamshift correction can be applied to the science data, if the offset between the science images in the odd-row and even-row subframes I_o and I_e can be determined, so that the two frames can be accurately aligned before the polarimetric combination of the frames is carried out (see Fig. 26).

It is more difficult to recenter frames without well defined intensity peaks, e.g. frames with low Strehl ratio, with saturated PSF, or coronagraphic images. For these cases, one can use beamshift corrections derived from short polarimetric cycles of well defined stellar PSFs, taken with the same (or similar) filter, the same polarimetric configuration and telescope orientation. Because the beamshift changes only slowly with parallactic angle and altitude, one can take such beam shift calibrations just before or/and after the science observation, using the PSFs of the same star, or another star with similar pointing directions (parallactic angle and altitude) $|\Delta p|$ and $|\Delta a| \lesssim 5^\circ$.

An example for a beamshift correction for a coronagraphic image is shown in Fig. 28, where residuals in the uncorrected differential polarization image is at the level of up to $\approx 1\%$ in Q/I or U/I near the coronagraphic mask. These data are corrected with the non-coronagraphic PSF measurements of the same star (Fig. 26) taken 10 min later. For this, the star was just offset from the coronagraphic mask and observed with a short integration and a ND-filter. This calibration reduces the residuals in the polarimetric image significantly, for example the standard deviation in the box at the bottom of the frames in Fig. 28 is 9.3 ct in the uncorrected frame and 4.4 ct in the corrected frame.

The residual noise is not completely removed by the beam shift correction as can be seen for the strong “s” speckles. The positive/negative ring feature at the edge of the coronagraphic focal plane stop is even enhanced and new spurious

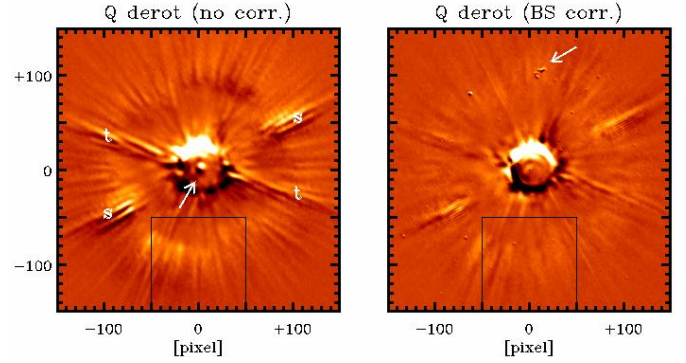


Fig. 28. Beam shift effect for α Cen B in the VBB filter for a coronagraphic (CLC-MT-WF) Stokes Q frame (*left*) and the beam shift corrected frame (*right*) for essentially the same instrument configuration as the stellar PSF in Fig. 26. The arrow in the *left panel* points to the PSF peak transmitted through the mask. PSF residual features are marked in the *left panel* with “t” and “s” according to Fig. 8. In the *right panel* the arrow points to one of several spots from the camera, which show up because of the applied beam-shift correction. The squares at the bottom mark the area for the reported $\sigma(Q)$.

positive/negative spots are introduced, as indicated by the arrow in the right panel of Fig. 28. These are intensity features originating from components located after the inclined mirrors. For example, the coronagraph, the deformable mirror, the poorly corrected bad pixels, or dust on the micro-lens array of the ZIMPOL detector introduce spurious positive/negative polarimetric signals if a beam-shift correction is applied. Some of these new problems can be solved with detector dithering, but it is still unclear how some of these spurious features can be removed again.

The beamshift can also be measured in high quality coronagraphic images, if the focal plane mask CLC-MT-WF is used. This mask is by design slightly transparent and therefore the same polarization pattern is visible in Fig. 28 (left) for the attenuated star marked with an arrow, as for the stellar PSF shown in Fig. 26 (Q , derot, no.corr.). Beamshift corrections based on the transmitted PSF using the CLC-MT-WF masks give good results, if the Strehl ratio for the observations is high and if the star is well centered on the mask. Of course, frame selection is important because a few good frames are sufficient to define the beamshift correction for many exposures of the same target taken before and afterwards.

5.5. Polarized PSF

The quality of the ZIMPOL polarimetric imaging can be assessed with an unpolarized or polarized stellar PSF without circumstellar emission. Such an object should show over the whole image plane a constant fractional polarization. Figure 29 shows the Stokes fluxes Q and U for the *V*-band of HD 183143 from the same observations used for the characterization of the intensity PSF in Fig. 8. The PSF in Q is just a faint replica of the intensity PSF, with central PSF peak, and speckle ring because the star has a high interstellar Q/I -polarization of about 5%. In U , only a weak negative peak is visible because of the small $U/I \approx -0.5\%$ telescope polarization. These polarimetric PSFs are corrected for the beam-shift effect and therefore they show no positive/negative central features for $r < 20$ pix. Outside $r > 20$ pix, no difference is visible between beam-shift corrected and not corrected profiles. The displayed PSFs were also not polarimetrically calibrated, because this has no impact on the polarization structure of the PSF.

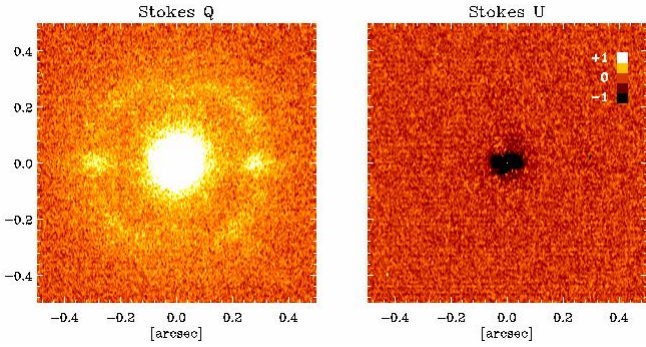


Fig. 29. Stokes Q and U images for the V-band filter of the PSF standard HD 183143. These are the polarization images corresponding to the intensity PSF shown in Fig. 8.

Figure 30 shows the corresponding mean radial $Q(r)$ and the azimuthal profile $Q(\phi, 80)$ for $r = 80$ pix through the speckle ring and the same for Stokes U . The lower panels show the corresponding fractional polarization signal, which are essentially constant in the radial and azimuthal profiles without instrumental structures in $Q(x, y)/I(x, y)$ and $U(x, y)/I(x, y)$ despite the large dynamic range with >3000 ct pix $^{-1}$ for the PSF peak and only a few counts per pix and frame further out.

This polarimetric fidelity is a particular advantage of the ZIMPOL technique which registers the opposite polarization modes I_{\perp} and I_{\parallel} with the same pixels. The differential polarimetric signal is therefore essentially independent of the exact flatfielding factors a^{ff}

$$a_{\perp}^{\text{ff}} I_{\perp} - a_{\parallel}^{\text{ff}} I_{\parallel} = a^{\text{ff}} (I_{\perp} - I_{\parallel})$$

or bias level subtraction values c^{bias}

$$(I_{\perp} - c_{\perp}^{\text{bias}}) - (I_{\parallel} - c_{\parallel}^{\text{bias}}) = I_{\perp} - I_{\parallel}$$

because the flat-fielding factors $a_{\perp}^{\text{ff}} = a_{\parallel}^{\text{ff}} = a^{\text{ff}}$ or the bias levels are $c_{\perp}^{\text{bias}} = c_{\parallel}^{\text{bias}} = c^{\text{bias}}$ are very close to identical for the two modes. This beneficial property of ZIMPOL is very useful for the analysis of polarization signals from circumstellar sources.

5.6. R Aqr: an example for circumstellar polarization measurements

We used R Aqr as test source for polarimetric imaging during the SPHERE/ZIMPOL commissioning. This object is bright, $m_I = 4.4^m$ at the time of our observations, and it showed in previous studies with aperture polarimetry strong, and highly variable, linear polarization (e.g. [Serkowski & Shawl 2001](#); [Joshi et al. 2012](#); [Aspin et al. 1985](#)). R Aqr is a nearby $d = 220$ pc symbiotic binary with a Mira variable undergoing heavy mass loss and binary interactions ([Schmid et al. 2017](#), and references therein).

Polarimetric data for R Aqr were taken in many different filters ([Schmid et al. 2017](#)), but we focus here on the I-band data taken obtained three different instrument modes:

- (i) in fast modulation using the 20 nm narrow-band Cnt820 filter for the PSF peak (hereafter called “nb”-image),
- (ii) fast polarimetry in the 150 nm wide broad-band I_PRIM filter where the PSF peak saturated (“sat”-image), and
- (iii) deep I_PRIM, slow-modulation polarimetry in coronagraphic mode (“coro”-image) for the “outer” regions.

The parameters of the different observations are summarized in Table 13, and the Stokes Q and U images are displayed in

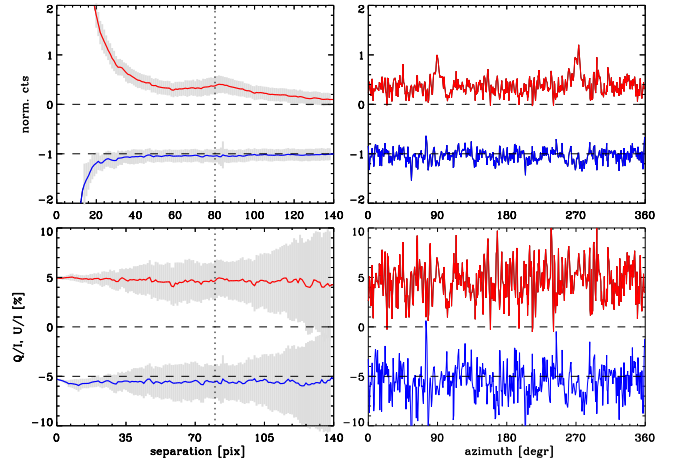


Fig. 30. HD 183143 mean radial V-band profiles (left) for the Stokes flux $Q(r)$ and $U(r)$ (top) and the fractional polarization $Q(r)/I(r)$ and $U(r)/I(r)$ (bottom) and the corresponding azimuthal profiles $Q(80, \phi)$, $U(80, \phi)$, and $Q(80, \phi)/I(80, \phi)$, $U(80, \phi)/I(80, \phi)$ (left). The U -data are shifted downwards in for better visibility and the dashed lines indicate the offset.

Fig. 31, and Table 7 lists atmospheric and PSF parameters for the I_{nb} image, which are representative for all R Aqr data.

5.6.1. Data reduction

The data were first reduced in a standard way, with an overscan bias subtraction, flatfielding, polarimetric signal extraction and combination. Already these basic steps allow a qualitative analysis of all extended polarization features described below.

In a second step, the reduction was rerun, but with applying a polarimetric beam shift correction before the combination of the polarization frames. The beam shift correction was derived from the unsaturated “nb”-data and also applied to the saturated and coronagraphic I_PRIM filter data. Applying the beam shift correction reveals also a Q - and U -quadrant pattern for the PSF-peak described below, and it reduces spurious polarization residuals at the position of strong speckles.

For an accurate quantitative analysis we correct our data with an image rotation of $\theta_0 = 2^\circ$ in clockwise direction to account for the astrometric offset from the North direction according to Eq. (2). Then we apply the polarimetric calibrations, deriving first Q_{c1}, U_{c1} (Eq. (7)) using the modulation-demodulation efficiencies ϵ_{mod} (Table 5), the corrections for the telescope polarization $p_{\text{tel}} = 0.4\%$, $\delta_{\text{tel}} = 68^\circ$ from Table 12, which yield for the parallactic angle of the observations ($\theta_{\text{para}} \approx -114^\circ$ to -122°) roughly $Q_{c3}/I \approx Q_{c1}/I$ and $U_{c3}/I \approx U_{c1}/I + 0.004$ (Eqs. (23) and (24) with $\epsilon_{\text{opt}} = 1$). As last step we apply a polarization angle offset correction of 6° according to Eqs. (25) and (26). Both, the astrometric correction of 2° and the polarimetric correction of 6° rotate the polarimetric Q - and U -quadrant pattern in clockwise directions so that the slightly tilted patterns from the basic reduction get an orientation which is essentially undistinguishable from the expected up-down/left-right Q -pattern and the corresponding diagonal $\pm 45^\circ$ U -pattern shown in Fig. 31.

Despite all these corrections, there remain ambiguities in the measured circumstellar polarization of R Aqr because of two effects. The limited resolution produces polarimetric cancellation between the $+Q$ and $-Q$ or the $+U$ and $-U$ regions (see e.g. [Schmid et al. 2006b](#)), and the unresolved emission

Table 13. Polarimetric test data for R Aqr from 2014-10-11 used in this work.

Parameter	Image		
	“nb”	“sat”	“coro”
Data sets ^a	0047-50	0059-62	0071-74
Filter	Cnt820	I_PRIM	I_PRIM
Coronagraph	–	–	CLC-MT-WF
exp. $n_{\text{DIT}} \times t_{\text{DIT}}$	10×1.2 s	10×1.2 s	10×20 s
QU-cycles	1	1	1
t_{total}	48 s	48 s	800 s
Modulation	fast	fast	slow
ct frame ⁻¹	$\approx 4.2 \times 10^6$	$\approx 1.5 \times 10^7$	$\approx 2.1 \times 10^8$

Notes. ^(a) Identifications corresponds to the fits-file header keyword “origfile” without prefix “SPHERE_ZIMPOL_OBS284”.

of the star is also intrinsically polarized and contributes to the measured polarization signal as can be inferred from the available multi-wavelength polarimetry taken during the same night. A more detailed analysis would be required to disentangle the intrinsic polarization of the central star from the circumstellar polarization signal. This is of much scientific interest, but must be deferred to a future paper focussing on the mass loss of R Aqr. The scope of this section are the measuring capabilities of SPHERE/ZIMPOL for high performance polarimetry and therefore we just analyze the calibrated measurements.

All data are count normalized ct_{n6} as in previous sections by setting the total counts of the star within an aperture diameter of $3''$ to 10^6 counts. For the saturated and coronagraphic images, where the PSF peak counts are not available, the halo-flux was adjusted to the normalized, unsaturated “nb”-image for r in the range $100 \text{ pix} < r < 250 \text{ pix}$. This procedure assumes, that the PSF halo flux remained unchanged and provides a good relative calibration for the three images.

5.6.2. Description of the Stokes Q and U images

The polarimetric data show the typical Stokes Q and Stokes U quadrant pattern of a circumstellar scattering region. The distribution of the scattering dust is a spherical and clumpy causing geometric features in Q and U which deviate clearly from a symmetric, smooth quadrant structure.

Polarization of the PSF peak. The “nb”-images for Q and U in Fig. 31 show the polarization in the PSF peak of the mira variable. Clear Q and U quadrant patterns are visible within $r \lesssim 15 \text{ pix}$ with maxima and minima located at a separation of about $r \approx 5 \text{ pixels}$ (18 mas or $\approx 3.6 \text{ AU}$) from the intensity peak center.

This polarization originates from scatterings in immediate surroundings of the central star. For an unresolved, strictly centro-symmetric scattering case the $+Q$, $-Q$ or $+U$, $-U$ components would just cancel, and such a zero is indeed seen in the center. The radius of R Aqr measured by interferometry is about 7–8 mas (e.g. Ragland et al. 2008) or about 2 pixels, thus the peak intensities in the Q and U parameters originates from within 1–3 stellar radii. The measurements at small separations depend strongly on the self-cancellation because the intrinsic positive and negative regions of $+Q$, $-Q$ or $+U$, $-U$ overlap substantially when convolved with the instrument PSF. Therefore, the fractional polarization inside 5 pix reaches extreme values of only Q/I , $U/I \approx \pm 0.25\%$, lower than $\approx \pm 1.0\%$ in the surrounding annuli $r = 5 - 10 \text{ pix}$, or $\approx \pm 1.5\%$ for $r = 10 - 30 \text{ pix}$. The intrinsic value for this circumstellar polarization is certainly

much larger, but hard to quantify without a detailed simulations of the signal convolution with the instrument PSF.

Polarimetry for $0.03'' < \rho \lesssim 0.20''$. The “sat”-images taken with the 150 nm broad-band filter I_PRIM yielded about four times higher photon counts (for the same exposure time) than the “nb”-image, roughly as expected considering the larger filter width but also the much lower stellar flux in the 750–800 nm region. Several pixels in the PSF peak are saturated and it is difficult to measure the beamshift. Therefore we applied the same beamshift correction as for the unsaturated “nb”-image.

The “sat”-images are ideal for polarimetric measurements of the separation range $30 \text{ mas} < \rho < 200 \text{ mas}$ filling the gap between the saturated peak and the inner working angle of the coronagraphic data. In the “sat”-data of R Aqr (Fig. 31), the polarized intensity Q from the circumstellar dust scattering is stronger on the East-side of the Mira variable than on the West side, most likely because of the hot companion located 45 mas to the West of the mira (Schmid et al. 2017).

Sensitive polarimetric observations in the radial range $30 \text{ mas} < \rho < 200 \text{ mas}$ are demanding because of the huge intensity gradient near the PSF peak with a flux ratio $f(0)/f(\rho) \approx 1000$ for $\rho = 0.20''$ (55 pix). Photon noise limited observations are achievable for the separation range $\rho \approx 0.07'' - 0.20''$ with exposures where the PSF-peak is just at the saturation limit or in saturation by a factor of a few. For lower illumination the read-out noise can dominate already around $0.1''$. For strong saturation of more than a factor of >5 the charges start to “bleed” into neighboring pixels mainly along the detector column direction and this affects the inner working angle of the observation.

Coronagraphic polarimetry for $r \gtrsim 0.1''$. The small bottom panels give the center of the I_PRIM-band “coro”-image. Clearly visible is the attenuation of the mask CLC-MT-WF, which has a spot radius of $\rho = 77 \text{ mas}$. The immediate surroundings of the coronagraph show a continuation of the structure seen in the non-coronagraphic images. The two large panels in Fig. 31 are based on the same “coro”-images as the small bottom panels, but the images are displayed with plotting and color scales emphasizing the weak polarization intensities at larger separation.

The integration time for the “coro”-images is 16.7 times longer than for the “sat”-images. In addition, the “coro”-images are much more sensitive because they were taken with the low gain $1.5 \text{ e}^- \text{ ct}^{-1}$ slow modulation mode with a low read-out noise. In slow modulation the spurious features from pixels with reduced charge transfer efficiency are weaker. Therefore, this mode is well suited for high precision polarimetry with long integrations outside the speckle ring $\rho > 0.6''$ where the temporal variations in the PSF structure are small. Some quasi-static speckle features are visible in Fig. 31 and they are marked according to Sect. 3.1 (Fig. 8).

For R Aqr, the high sensitivity of the Q_{coro} -, U_{coro} -frames reveal well defined polarization features from individual dust clouds at separations of about 120 pix ($\approx 430 \text{ mas}$) in the North and at about 80 pix (290 mas) in the southwest, as well as other fainter clouds. In addition, there are many extended structures and clear asymmetries in the distribution of the Q and U signal apparent out to separations of about 150 pix (600 mas).

Polarization signal at separations $\gtrsim 1$ arcsec. The detection limits for extended polarimetric emission can be pushed further by averaging the signal in larger measuring areas. Figure 32 shows the coronagraphic R Aqr data, but binned by $10 \times 10 \text{ pixels}$ and the color scale sharpened to $\text{ct}_{n6} \pm 0.001$, by a factor of 50 when compared to the large frames in Fig. 31. Both, the Q - and U -quadrant patterns extend now to the edge of the detector

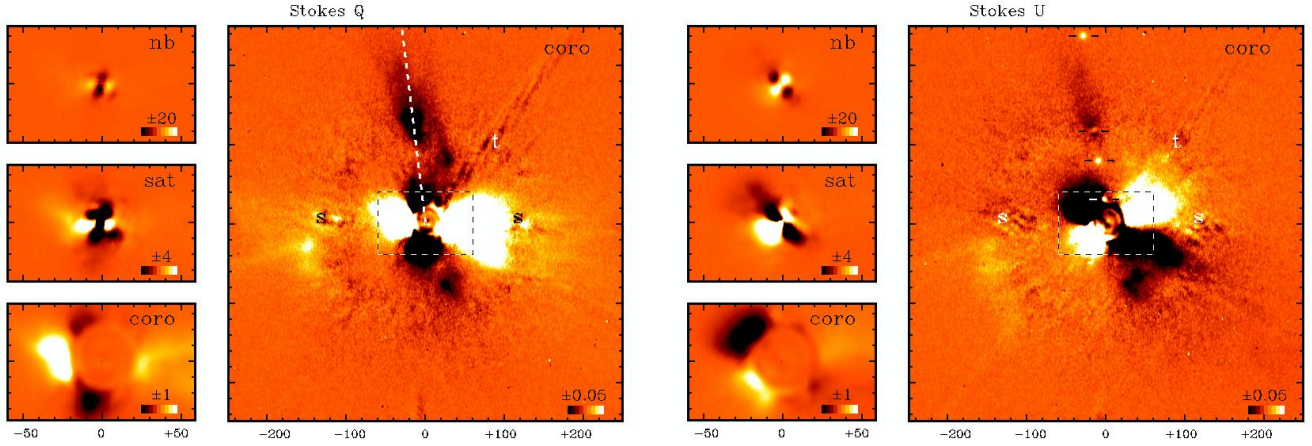


Fig. 31. R Aqr I -band Stokes Q (left) and U (right) signal measured for the unsaturated PSF in the narrow-band (nb) Cnt820 filter (upper left), for the saturated broad band I_PRIM filter (middle left), and deep coronagraphic observations for the I_PRIM filter and slow polarimetry mode (lower left and large frame). The cut for the count profiles of Fig. 33 is shown in the large Q -frame. Units are in pixels of 3.6 mas.

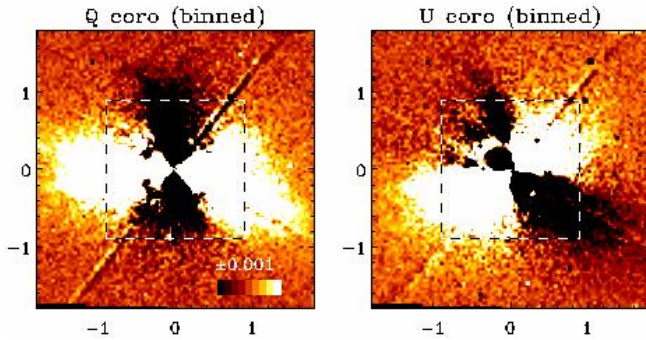


Fig. 32. Binned R Aqr I -band Stokes Q (left) and U (right) map extending over the whole detector of $3.6'' \times 3.6''$ detector area. The dashed boxes are the $1.8'' \times 1.8''$ areas shown in the large panels of Fig. 31.

at a separation of $\rho = 1.8''$. At this level of sensitivity the correction for field dependent instrumental polarization effects and the intrinsic polarization of the central star and its light halo become important issues for the accurate measurement of the “large” scale polarization signal.

SPHERE/ZIMPOL allows for polarimetric observations with field angle offsets or polarization angle offset, which are both powerful methods to disentangle instrumental effects from weak but real sky signals.

5.6.3. Quantitative analysis for a radial cut

This section gives a quantitative analysis for the R Aqr polarization signal along the dashed line plotted in the large Q_{coro} -image (Fig. 31) through the strong dust feature in the North. In the corresponding U_{coro} -frame, we inserted along the same direction artificial point signals, marked with horizontal dashes, for the evaluation of the detection limits of faint, polarized point sources.

Measured surface brightness and sensitivity limit. Figure 33 shows the radial cuts $I(r, 7^\circ)$ and $Q(r, 7^\circ)$ for the “nb”-, “sat”- and “coro”-images. For this 1-dim. profile extraction the reduced images were rotated by 7° , so that the cuts are simple mean profiles of 5 vertical columns from the central source at $r = 0$ to the upper edge at $r = 500$ pix. This cut through the northern dust cloud at $r \approx 120$ pix avoids the strong vertical frame transfer trail in the non-coronagraphic images. The cloud, is not visible

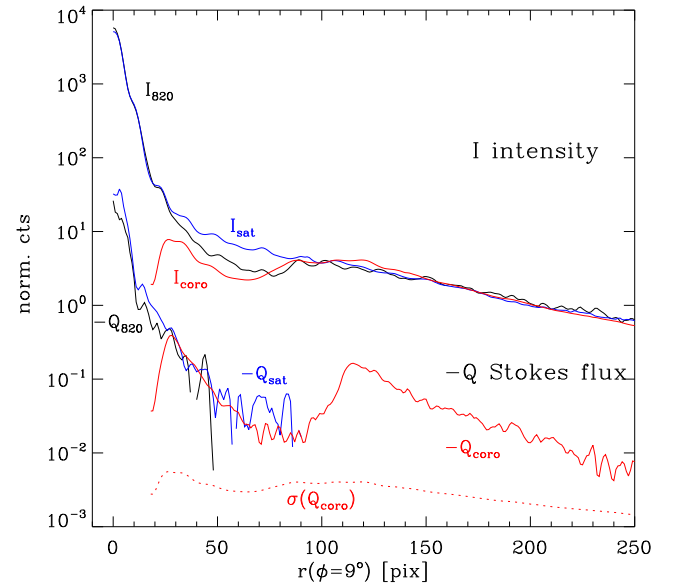


Fig. 33. Radial profiles for R Aqr for the $\phi = 7^\circ$ -direction through the bright scattering clouds in the north as indicated in Fig. 31.

in the intensity profile, but appears as very strong, high signal-to-noise polarization source in polarimetric differential imaging. The profiles in Fig. 33 are given in flux normalized counts ct_{nb} like in Figs. 8 and 13 and the dotted curve is the $1\text{-}\sigma$ photon noise limit $\sigma(Q_{\text{coro}})$ for the “coro”-profile.

Table 14 lists for selected areas along the profile the measured ct_{nb} -values for $I(r)$ and $Q(r)$, the fractional polarization $Q(r)/I(r)$, and the corresponding surface brightness contrast $C_{\text{PSF}}(r)$ for the intensity and C_{SB} for the polarization in magnitudes. Note, that the sign of the Q -Stokes flux signal is negative in the North of the central source.

The three intensity profiles I_{nb} , I_{sat} , and I_{coro} (Fig. 33 and Table 14) show quite some differences at small separations which reflect most likely the atmospheric and AO variations between the I_{nb} and I_{sat} frames, and the suppression of the PSF diffraction rings for I_{coro} . Despite this, the three Q -profiles agree very well at $r = 30$ pix and for Q_{sat} and Q_{coro} also at 80 pix (Q_{nb} (80 pix) is dominated by read-out noise). This confirms the finding from Fig. 31, that the “nb”-, “sat”-, and “coro”-frames

Table 14. Normalized mean counts ct_{n6} for the PSF surface brightness of R Aqr and the polarized surface brightness of the circumstellar region along the position angle $\phi = 9^\circ$ for the frames for the intensity I_{nb} , I_{sat} , and I_{coro} and the polarized flux Q_{nb} , Q_{sat} , and Q_{coro} .

Parameter	$\rho ["] =$	0	0.018	0.108	0.288	0.432	0.864	1.728
	$r [\text{pix}] =$	0	5	30	80	120	240	480
	area [pix]	1×1	1×5	10×10	10×10	10×10	10×10	20×20
Intensity								
$I_{nb}(r)$	ct_{n6}	5775	1846	14.9	2.9 ::			
$I_{sat}(r)$	ct_{n6}	5116 ^a	1823	18.7	4.7	3.2	0.67 ::	
$I_{coro}(r)$	ct_{n6}	15.4 ^b	1.60 ^b	7.13	3.39	3.82	0.61	0.073
Polarized flux								
$-Q_{nb}(r)$	ct_{n6}	26.2	12.1	0.24	0.013::			
$-Q_{sat}(r)$	ct_{n6}	32.3 ^a	21.1	0.368	0.028	0.086	5.4×10^{-3}	
$-Q_{coro}(r)$	ct_{n6}	0.025 ^b	0.0292 ^b	0.319	0.0216	0.126	7.4×10^{-3}	0.14×10^{-3}
Fractional polarization								
$-Q(r)/I(r)$		0.45%	1.16%	1.98%	0.64%	3.3%	1.2%	0.19%
Surface brightness contrast [$\Delta\text{mag arcsec}^{-2}$]								
$C_{SB}(r)$ ^c	mag	-6.6	-5.4	0.6	1.5	1.3	3.3	5.6
$C_{SBpol}(r)$ (R Aqr)	mag	-0.8	-0.5	4.0	6.9	5.0	8.1	12.4
Artificial point source contrast [Δmag]								
C_{pol} ^d (b,c,d,e)	mag			10.8	12.5	12.5	12.5	
$C_{pol}(r)$ 5σ -limit	mag			8.8	12.6	13.0	14.9	15.6

Notes. ^(a) Saturated PSF peak; ^(b) coronagraphically attenuated PSF peak; ^(c) surface brightness contrast $C_{SB} = SB - m_{star}$; ^(d) polarized flux point source contrast $C_{pol} = m_{pol} - m_{star}$.

are matching very well and provide a continuous mapping of the differential polarization signal from the center $r = 0$ to large separations $r > 250$ pix ($\rho > 0.9''$).

Table 14 lists in italic letters the $I(r)$ - and $Q(r)$ -values with the highest signal-to-noise, which are not affected by saturation or attenuation by the coronagraph. The polarized surface brightness of the circumstellar dust is about 50–500 times lower than the intensity of the stellar PSF as follows from the fractional polarization $Q(r)/I(r)$. This ratio depends on the PSF and therefore the variable AO performance and is not very useful for the characterization of the circumstellar scattering.

The polarized surface brightness contrast C_{SBpol} is a better quantity to describe the polarized radiation from the dust (Sect. 5.1). For a region north of the central light source we can approximate $C_{SBpol}(r) \approx -Q(r)/I_{star}$ where I_{star} is the total stellar intensity as measured in an aperture of $3''$ -diameter. The obtained values range from $SB_{pol} - m_{star} = 4.0$ to 12.4 mag arcsec⁻² for the separation range from $\rho = 0.11''$ to $1.73''$ (Table 14). This surface brightness in polarized flux is up to 19^m fainter than the surface brightness of the PSF intensity peak $C_{SB}(0) = -6.6^m$.

The R Aqr “coro”-images presented here are not really deep data, because they consist only of $n_{DIT} = 40$ frames or $t_{total} = 400$ s of integration for Q and the same for U . A comparison of R Aqr with other SPHERE/ZIMPOL polarimetric data in the literature shows that C_{SBpol} is about 1–2 mag higher (relative emission Q_{cs}/I_{star} , U_{cs}/I_{star} fainter) than the bright rims of bright proto-planetary disks, like HD 135344B with $C_{SBpol} \approx 5$ mag arcsec⁻² at $\rho = 0.2''$ (Stolker et al. 2016), or HD 142527 with ≈ 7 mag arcsec⁻² at $\rho = 0.9''$ (Avenhaus et al. 2017). Compared to these disk systems, the R Aqr central star is a bright source and therefore a comparable or better contrast is achieved with a short integration time. An about 2 mag higher contrast (fainter signals) of $C_{SBpol} \approx 7.6$ mag arcsec⁻² at $\rho = 0.3''$ or 9.5 mag arcsec⁻² at $\rho = 1.2''$ is measured for the debris disk HIP 79977 (Engler et al. 2017).

Detection limits for point sources. For the determination of the point source contrast limit, we use the U -image, which serves as low background observation for the $\phi = 7^\circ$ profile direction. We insert in the U -frames artificial point sources at $r = 30, 80, 120, 240,$ and 480 pixels and the U -polarization signals shown in Fig. 31 are $ct_{n6} = 0.058$ ct pix⁻¹ corresponding to a polarization contrast of $C_{pol} = f_{pol}/f_{star} = 10^{-5}$ ($\Delta m = 12.5^m$) for $r = 80, 120$ and 240 pix and $ct_{n6} = 0.29$ ct pix⁻¹ at $r = 30$ (see Table 14).

The 5σ contrast limits $C_{pol}(r) = U_{5\sigma}(r)/I_{star}$ for polarized point sources are then derived by measuring the extracted signal similar to the measurements of α Hya B in Sect. 4.3 for artificial point sources with a range of U -fluxes. This yields the 5σ limits of $\Delta m \approx 12.6^m, 13.0^m$ or 14.9^m at separations of $0.29'', 0.43'',$ or $0.86'',$ respectively (Table 14).

These are contrast limits comparable to the limits reported by van Holstein et al. (2010) for polarimetric observations of the HR 8799 planets in the near-IR with SPHERE/IRDIS. For separations $\rho \gtrsim 0.6''$ the ZIMPOL and IRDIS polarimetric modes are for bright targets essentially photon noise limited. Thus, deeper polarimetric contrast limits can be achieved, if more photons are collected with longer integrations or with observations of brighter targets. At small separations $\rho \lesssim 0.6''$, there is in the R Aqr polarimetry data presented here, some residual speckle noise besides the photon noise, because our simple test data are not optimized for deep contrast limits. ZIMPOL was designed for the photon noise limited search of polarized light from extrasolar planets around very bright stars $\lesssim 3^m$ based on a large number of well illuminated frames $n_{DIT} > 5000$ and long total integration times $t_{total} > 3$ h (Schmid et al. 2006a; Thalmann et al. 2008). Thus, the real polarized point source contrast limit of SPHERE/ZIMPOL can only be demonstrated with such long integration of very bright stars using coronagraphy and fast modulation polarimetry and more elaborate observing strategies than the simple “one HWP2-cycle” test used for our R Aqr.

A non-polarimetric ZIMPOL point source observation using angular differential imaging (ADI) of PZ Tel A and B is

described in Maire et al. (2016a). This system with a separation of $\rho = 0.48''$ has in the R_PRIM band a contrast of $\Delta\text{mag} = 9.7^m$. The companion is detected with 30 min of integration in one ZIMPOL arm, with only 14° of field rotation and under mediocre $>1.1''$ seeing conditions. Companions with much higher contrast of at least $\Delta\text{mag} \approx 12.5^m$ should be observable with ZIMPOL ADI if data are taken under better conditions and a better observing strategy.

6. Discussion

This paper presents a detailed description of the SPHERE/ZIMPOL instrument to support and promote scientific investigations based on new or archival observations. The provided information should also be helpful to optimize observing and data reduction strategies, for an evaluation of the performance of this instrument for possible upgrades (e.g. Lovis et al. 2017), or the design of more advanced systems for future telescopes like the ELT (Kasper et al. 2013; Keller et al. 2010).

High contrast and high resolution observations from the ground require the combination of an adaptive optics system with coronagraphy, and a differential imager for speckle noise suppression. All these methods are tricky, because the resulting performance depends on the target brightness, the atmosphere, the selection of the coronagraph, the mode of the differential imager, and on the appropriate observing strategy. It is not possible to describe such a complex system and its performance in a single paper, or a compact user manual. This paper provides a comprehensive hardware description, and highlight three important aspects, which are particularly special for the SPHERE/ZIMPOL instrument when compared to other AO-imaging systems: (i) the characterization of the PSF-properties in the visual provided by the SPHERE AO system and the VLT telescope, (ii) the performance of the visual coronagraph, and (iii) the polarimetric measuring strategy and data characteristics of the ZIMPOL system.

More technical information about ZIMPOL will become available in the future: a paper on the astrometric calibration is in preparation, and a description of photometric parameters is planned. Schmid et al. (2017) describe many technical aspects on the H α imaging and absolute photometric measurements in several filters. Further, we expect that useful performance characteristics of SPHERE/ZIMPOL can be extracted from science papers, which aim for accurate measurements or push the performance of this instrument to the limits.

6.1. Key performance properties of ZIMPOL

SPHERE/VLT is one of the new generation extreme AO-systems available at large telescopes. The quality of the obtained PSFs depend strongly on the AO-system, the atmospheric conditions and the guide star magnitude m_R and Table 7 characterizes the visible performance of the AO system for several typical cases using simple measuring parameters, e.g. the normalized PSF peak flux $\text{ct}_{n6}(0)$. Good corrections with $\text{ct}_{n6}(0)/10^6 > 0.3\%$ (Strehl ratio $\gtrsim 15\%$ in the R-band) are achieved for stars down to $m_R \approx 8^m$ with an atmospheric seeing of $\approx 1''$. For bright stars $m_R < 7^m$ and good seeing conditions $<0.8''$ the relative peak flux is twice as good $\text{ct}_{n6}(0)/10^6 > 0.6\%$ and this corresponds to Strehl ratios of $\approx 30\text{--}50\%$ in the R-band (see also Fusco et al. 2016). This provides for SPHERE/ZIMPOL a point source contrast performance of $\Delta m \approx 12.5^m$ outside $0.15''$ for the polarized flux (Table 14). The existing ADI-data of the PZ Tel binary Maire et al. (2016a) indicate, that similar contrasts

performance are also possible for the intensity signal of a point source. For extended polarized emission, the system reaches outside of $0.15''$ surface brightness contrast limits better than $C_{\text{SBpol}} > 7.5^m \text{ arcsec}^{-2}$.

The most outstanding property of SPHERE/ZIMPOL is the spatial resolution of up to 20 mas surpassing all other imaging instruments available at the VLT (de Zeeuw 2016). This limit can even be improved with sparse aperture masking, which is one of the most recent upgrades of the SPHERE/ZIMPOL system (Cheetham et al. 2016). Observations with even higher resolution requires currently interferometric observations.

Visual extreme AO-systems are also available at other observatories, e.g. the pioneering MagAO-system at the Magellan telescope (Close et al. 2013), or SCEXAO at the Subaru telescope (Jovanovic et al. 2015). Scientifically important features shared by all these visible AO systems is the access to the strong H α emission line, and the extension of high resolution observations from the traditional near/mid-IR to the visible wavelength range (see Close 2016). There will be some healthy competition between these systems, but much more important is the mutual benefit in establishing common calibration targets, improving and checking measuring strategies and data reduction, and enhancing the science return thanks to complementary performance characteristics.

Many properties of the ZIMPOL system are quite typical for high resolution imagers using AO and they are not repeated here. We list here the special features of ZIMPOL:

- a small detector pixel scale of $3.6 \text{ mas} \times 3.6 \text{ mas}$, giving $77160 \text{ pix arcsec}^{-2}$ for each detector and a high full well photo-electron capacity of $7 \times 10^5 \text{ e}^- \text{ pix}^{-1}$, allowing for efficient high contrast observations of the circumstellar regions of bright stars $m_R < 8^m$ in broad band filters,
- dual beam imaging and polarimetry for simultaneous observation with two cameras with many different options for the combination of filter bands, for example the combination of 1 nm or 5 nm H α filters with a H α continuum filter for spectral differential imaging. Alternatively, also narrow band filters can be combined with broad band filters for simultaneous, and therefore accurate flux measurements of the bright component in a high contrast system. For example, a bright star can be observed with the narrow Cnt820 or Cnt_Ha filters in one arm, and the faint companion or circumstellar features in the second arm with the corresponding broad band filter I_PRIM or R_PRIM, respectively,
- a high resolution imaging polarimeter based on a fast modulation-demodulation technique for speckle noise suppression allowing high precision, $\Delta p \lesssim 10^{-4}$, broad-band polarimetry,
- an innovative concept for the compensation and control of the instrument polarization effects providing absolutely calibrated linear polarization measurements with an accuracy of about $\pm 0.1\%$ for the relative Stokes parameters Q/I and U/I , despite the fact that SPHERE/ZIMPOL is a polarimetrically complex instrument at the Nasmyth focus.
- the status of SPHERE/ZIMPOL as an ESO/VLT facility instrument, which ensures a well monitored and characterized system, steady improvements of the instrument operation, high standards for the execution of the observations and data calibration, a well established and user-friendly data archiving, and hopefully a long life-time. Another huge benefit is the large ESO user community using this system for a wide range of science targets with innovative observing strategies.

6.2. Possible instrument upgrades

Some evolution of the ZIMPOL system capabilities can be expected in the near future, because they can be realized without much effort. Very desirable would be the availability of the ZIMPOL off-axis fields shown in Fig. 3, which are currently not offered as user mode. This would provide the possibility to extend the field of view for more extended objects to a diameter of 8", matching better the 11" × 12.5" field offered by the infrared channel SPHERE/IRDIS.

A very useful upgrade would be the availability of a low read-out noise mode for imaging, equivalent to the slow modulation polarimetric mode with low detector gain. Especially, low flux measurements taken in narrow band and line filters, as well as observations in the off-axis fields outside the light halo of the bright central star would profit because they are often read-out noise limited. Just taking long integrations >5 min with a running AO system is critical because a few seconds of strongly reduced AO-performance or even an AO open loop, caused for example by a particularly bad atmospheric turbulence event, can degrade an entire long integration with an enhanced background of light from the central star. Another problem of long integrations are small pointing drifts of ≥ 10 mas which cause image smearing and this would be avoidable with shorter integrations and a realignment of individual frames in the data reduction.

Another type of quite easy instrument upgrades are new filters or coronagraphic masks in the exchange wheels of ZIMPOL or the visual coronagraph, respectively. New science cases may emerge, which call for filter changes, or better coronagraphic concepts could be implemented (e.g. Patapis et al. 2018).

Of course, most relevant would be any upgrades to the AO system or any other effort to improve the AO performance, like the suppression of the low wind effect with changes to the telescope (Sauvage et al. 2016a). Better wavefront corrections for SPHERE based on new software or hardware would be particularly beneficial for the short-wavelength ZIMPOL subsystem where typical Strehl ratios are $\lesssim 50\%$ with quite some room for improvements.

6.3. New research opportunities offered by SPHERE/ZIMPOL

The special technical properties of SPHERE/ZIMPOL offer many new research opportunities, some are unique to this instrument and some are shared with the other visible light AO systems mentioned above. At least, the visual ZIMPOL observations are complementary to the data from the SPHERE near-IR focal plane instruments IRDIS and IFS, or other near-IR AO systems like for example Gemini/GPI (Macintosh et al. 2014) or Subaru SCExAO (Jovanovic et al. 2015), by extending the wavelength domain of high resolution and high contrast imaging towards shorter wavelengths. In the following, we provide an incomplete list of science topics where SPHERE/ZIMPOL is already providing or will provide interesting or even very important contributions in high contrast imaging. In this discussion on science opportunities one should not forget the technical requirement that SPHERE/ZIMPOL observations need a bright central star $m_R \lesssim 9^m$ for the AO wavefront sensing and that the system provides only a quite limited field of view $\rho < 4''$.

6.3.1. Search for extra-solar planets in reflected light

ZIMPOL was selected by the European Southern Observatory for the SPHERE VLT "planet finder" instrument with the mandate to explore the detection limits of high contrast polarimetric

imaging for the search of reflected light from extrasolar planets (Schmid et al. 2006a). The aim of this unique instrument is to reach a contrast limit between the polarized flux of the planet $p_{\text{pl}} \times I_{\text{pl}}$ and the total flux of a star I_{star} of

$$C_{\text{pol}} = \frac{p_{\text{pl}} \times I_{\text{pl}}}{I_{\text{star}}} = 10^{-8}$$

within an angular separation smaller than $\rho < 1''$. This limit would allow a detection of a Jupiter-sized giant planet or even terrestrial planets with a physical separation of 0.5–1 AU around one of the nearest bright stars (Thalmann et al. 2008; Milli et al. 2013). This aim defined many of the ZIMPOL design decisions and therefore this imager is tuned for the detection of very faint polarization sources near very bright stars.

The SPHERE-team carries out as part of their guaranteed time observations obtained for building the instrument, an investigation of the achievable detection limits of for the search of extra-solar planets. Very high contrast observations of a small number of targets are currently taken. The data confirm that ZIMPOL can reach at least for separations $\rho > 0.5''$ the above mentioned detection limit. The short test observations of R Aqr described in the previous section give already an impression of the high contrast performance in polarimetric imaging. SPHERE/ZIMPOL is pioneering this technique and the achievable contrast limits are certainly of interest for other high contrast search programs targeting the reflected light from extra-solar planets and for the planning of future instruments. Whether a successful detection will be possible with SPHERE/ZIMPOL depends on the presence of favorable planets within about 5 pc and further progress in the observations and data analysis.

6.3.2. Differential polarimetric imaging of circumstellar disk.

Disks around young stars are a primary science case for the SPHERE instrument and differential polarimetric imaging is a powerful technique for high contrast disk observations (e.g. Kuhn et al. 2001; Perrin et al. 2009; Quanz et al. 2011; Muto et al. 2012). The high spatial resolution and the high polarimetric sensitivity of ZIMPOL are ideal for the mapping of faint circumstellar disks in polarized light. The visual ZIMPOL data can be combined with near-IR observations, for example from SPHERE/IRDIS, to study the color dependence of the reflected light from protoplanetary disks around young stars like for example HD 135344B or TW Hya (Stolker et al. 2016; van Boekel et al. 2017).

Let us compare for this important science case the pro and cons for the ZIMPOL and IRDIS polarimetry modes for the differential polarimetric imaging of circumstellar disk, focussing on detecting a disk and mapping structural features. For fainter central stars $m_R > 8^m$ IRDIS polarimetry provides as important advantage a significantly better AO performance, because all light in the 500–900 nm range can be used for the wave front sensing. The ZIMPOL science channel shares this light with the WFS and therefore only 21% of the flux is available for the WFS, if the gray beam splitter is used, or about 80% for the dichroic beam splitter. Another advantage of IRDIS is the larger field of view of 11" × 11", about ten times larger than the 3.6" × 3.6" detector field of view of ZIMPOL, or much more efficient than using multiple field observations inside the 8" diameter instrument field of view. On the other side, the main advantages of ZIMPOL polarimetry when compared to IRDIS or other IR-polarimeters are the higher spatial resolution and the very good speckle noise suppression by the fast-modulation polarimetry

techniques as described in this paper for R Aqr. Therefore, a higher contrast can be obtained for circumstellar disk around bright stars in the separation range $\rho \approx 0.02''-0.2''$ and a good example is the detection of the inner disk of HD 142527 by Avenhaus et al. (2017). For disks around bright stars, ZIMPOL is at least competitive for the separation range $\rho \approx 0.2-2.0$ as demonstrated for the faint debris disks HIP 79977 (Engler et al. 2017), but also for the innermost regions of bright protoplanetary disks, like HD 100457 (Benisty et al. 2017). In addition, ZIMPOL provides a more advanced polarimetric concept than IRDIS or other AO-assisted polarimetric imagers, allowing an easier calibration of polarimetric data and a quantitative analysis of the polarized reflectivity of the scattering dust.

6.3.3. Mass loss from red giants

The combination of high spatial resolution and sensitive polarimetry is ideal for the mapping of the light scattering from the circumstellar dust with SPHERE/ZIMPOL (e.g. Kervella et al. 2015; Khouri et al. 2016; Ohnaka et al. 2017a). As shown in Sect. 5.6 for R Aqr, the polarized light from dust scattering can be measured over a very wide separation range, and asymmetries, clumps and their evolution can be investigated in much detail. This important information from high resolution polarimetry, which was pioneered with interferometric observations by Ireland et al. (2005), or sparse aperture masking by Norris et al. (2012), is now also available with “simple” imaging. Such observations could be particularly useful for investigations and the modeling of the complex dust formation process in pulsating AGB stars (e.g. Aronson et al. 2017; Höfner et al. 2016; Höfner 2008).

Light scattering observations are highly complementary to observations of the thermal emission of the circumstellar dust in the mid-IR with e.g. the VLTI/MIDI interferometer (Paladini et al. 2017). AO observations in the visual achieves a comparable or even better resolution than mid-IR interferometry and is therefore well suited for the mapping of the complex distribution of circumstellar dust near the mass losing star. The visible range is ideal for the small dust particles formed around mass-losing red giants because they scatter much more efficiently short wavelength light. A technical challenge for very bright red giants are detector saturation issues. Red giants are much fainter in the visual and the ZIMPOL system is designed especially for high contrast observations of very bright targets and therefore also for the investigation of the brightest, most extended, nearby red giants.

6.3.4. Emission lines in stellar jets and outflows

Stellar jets and outflows produce often H α and other emission lines from shocks or photoionized regions. ZIMPOL line filters are available for the H α 656 nm, [O I] 630 nm, and HeI/NaI 588/589 nm lines which may serve as tracer of different types of ionized or partially ionized gas.

Achieving high contrast and high resolution observations in line filters is important for stellar jets from young stars (Frank et al. 2014) to access the innermost 10 AU where the outflow is not yet significantly perturbed by the interaction with the ambient medium. This requires line observations at separations below 70 mas for sources in nearby star-forming regions. Observing the innermost flow morphology is important to pinpoint the initial ejection site of the matter, e.g. a stellar wind, an “X-wind” from the inner edge of the disk, or a disk wind, which is then further accelerated and collimated by the combined action of magnetic fields

and rotation (Ferreira et al. 2006). A first demonstration of the ZIMPOL potential on this topic is provided in Antonucci et al. (2016) with H α and [O I] observations of the young binary Z CMa. The authors could trace the collimated jet from one of the components down to ~ 70 mas from the driving source, revealing a jet wiggling on time-scales of a few years, which may be induced by a non-detected close-in companion.

For many astronomical objects countless imaging data already exists of the circumstellar line emission in the visual wavelength region taken with ground-based or space telescopes. The line observations of R Aqr provide a good example for the complementarity of emission line imaging with the SPHERE/ZIMPOL AO system (Schmid et al. 2017), with HST imaging (Melnikov et al. 2018), and with seeing limited imaging (Liimets et al. 2018).

6.3.5. Resolving the atmosphere of red giants.

The most extended red giant stars can be resolved with “simple ZIMPOL imaging” with a resolution of up to 20 mas as demonstrated for example for R Dor (Khouri et al. 2016) or α Ori (Kervella et al. 2016). “Simple imaging” because one can take many images in several filters within a few minutes, select the best data and measure wavelength dependencies. Geometric features, such as large spots or polar and equatorial zones, can be investigated and flux ratio maps can be obtained with simultaneous differential imaging, in e.g. the TiO_717 and Cnt748 band filters which sample cold and hot surfaces regions, or the N_Ha and CntHa filter pair for possible signs of shock heating. The “simple imaging” is also ideal for a monitoring program of the temporal evolution of surface features in these stars. Even better spatial resolution $\rho < 20$ mas should be achievable with sparse aperture masking or with advanced data analysis techniques. For these reasons the “simple”, ≈ 20 mas resolution, SPHERE/ZIMPOL imaging of extended red giant atmospheres provides useful complementary information with respect to the higher resolution, but much harder to obtain interferometric data (e.g. Haniff et al. 1995; van Belle et al. 1996; Ohnaka et al. 2017b).

6.3.6. Close binary stars.

For very close binary stars, the ≈ 20 mas spatial resolution of SPHERE/ZIMPOL is of course very useful for orbit determinations and the photometry of the individual components (e.g. Janson et al. 2018). A particular niche for the visual ZIMPOL instrument, when compared to near-IR AO instruments, are faint, hot companions to red stars, like white dwarfs companions to Ba-star, or H α emitting active components to M-giants like the symbiotic system R Aqr shown in Fig. 6 (see also Schmid et al. 2017). The relative position between roughly equal flux ($|\log(f_1/f_2)| \lesssim 1$) hot and cold binary components can certainly be determined for separations of ≈ 10 mas or even smaller with simultaneous measurements of the combined binary PSF in a visual and a red filter. Photocenter differences between two bands might even be measurable at the milli-arcsec level, if other stars in the field or the features of a coronagraphic mask can be used as relative astrometric reference.

6.3.7. Solar system objects.

The SPHERE AO system is capable to lock on moving solar system objects if they are bright enough $m_R \lesssim 10^m$ and not too extended $\lesssim 2''$. This was demonstrated during the SPHERE

commissioning for Titan³ which has a diameter of $\rho = 0.8''$ and even Neptune with $\rho = 2.4''$ (Fusco et al. 2016). Thus, many bright asteroids, the Galilean moons, and Saturn's moon Titan can be imaged in the visual. Sizes, shapes and surface structures can be investigated in much detail (Vernazza et al. 2008), and with enhanced resolution when compared to the near-IR range (e.g. Marchis et al. 2006), including the polarimetric properties of the reflecting terrains.

6.4. Conclusions

SPHERE/ZIMPOL is a very versatile adaptive optics instrument and we therefore expect many exciting new scientific results from this instrument. The above listed technical performances, upgrade options, and science topics give only a few examples of possible observational projects with this instrument.

Observational results based on adaptive optics profit a lot from the much enhanced spatial resolution and this provides since many years a continuous string of new detections (see Davies & Kasper 2012). The description of SPHERE/ZIMPOL given in this paper should help to define the best observing strategy for reaching deeper detection limits for new discoveries with AO observations at very high spatial resolution in the visual, using polarimetric imaging, angular or differential imaging with broad band, narrow band, or line filters.

On the other side, accurate quantitative measurements with AO systems are often difficult, because of the strongly variable atmospheric conditions and the resulting system performance. Particularly problematic is the photometry for very faint companions or extended circumstellar features for which simultaneous or quasi-simultaneous differential measurements are impossible. This makes the accurate characterization of high contrast objects in different wavelength bands, taken often with different instruments and usually under different atmospheric conditions very difficult and often uncertain. A lot of effort is required to describe AO observations accurately and in a reproducible way but this is required for a detailed characterization of high contrast objects. This paper provides therefore a lot of technical information for the accurate characterization and calibration of SPHERE/ZIMPOL measurements.

Acknowledgements. HMS thanks Wolfgang Löffler, Universiteit Leiden, for very helpful discussions and comments about the Goos-Hähnchen shift and related effects. SPHERE is an instrument designed and built by a consortium consisting of IPAG (Grenoble, France), MPIA (Heidelberg, Germany), LAM (Marseille, France), LESIA (Paris, France), Laboratoire Lagrange (Nice, France), INAF – Osservatorio di Padova (Italy), Observatoire de Genève (Switzerland), ETH Zurich (Switzerland), NOVA (Netherlands), ONERA (France) and ASTRON (Netherlands), in collaboration with ESO. SPHERE was funded by ESO, with additional contributions from CNRS (France), MPIA (Germany), INAF (Italy), FINES (Switzerland) and NOVA (Netherlands). SPHERE also received funding from the European Commission Sixth and Seventh Framework Programmes as part of the Optical Infrared Coordination Network for Astronomy (OPTICON) under grant number RII3-Ct-2004-001566 for FP6 (2004–2008), grant number 226604 for FP7 (2009–2012) and grant number 312430 for FP7 (2013–2016). HMS, SH and NE acknowledge financial support from SNSF through grant 200020_162630. Part of this work has been carried out within the framework of the National Centre for Competence in Research PlanetS supported by the Swiss National Science Foundation. H.A. and S.P.Q. acknowledge the financial support of the SNSF.

References

Aiello, A., Merano, M., & Woerdman, J. P. 2009, *Phys. Rev. A*, **80**, 061801
Akiyama, E., Muto, T., Kusakabe, N., et al. 2015, *ApJ*, **802**, L17

³ ESO press release www.eso.org/public/news/eso1417

- Amara, A., & Quanz, S. P. 2012, *MNRAS*, **427**, 948
Antoniucci, S., Podio, L., Nisini, B., et al. 2016, *A&A*, **593**, L13
Appenzeller, I. 1968, *ApJ*, **151**, 907
Aronson, E., Bladh, S., & Höfner, S. 2017, *A&A*, **603**, A116
Artmann, K. 1948, *Ann. Phys.*, **437**, 87
Aspin, C., Schwarz, H. E., McLean, I. S., & Boyle, R. P. 1985, *A&A*, **149**, L21
Avenhaus, H., Quanz, S. P., Schmid, H. M., et al. 2014, *ApJ*, **781**, 87
Avenhaus, H., Quanz, S. P., Schmid, H. M., et al. 2017, *AJ*, **154**, 33
Bailey, J., & Hough, J. H. 1982, *PASP*, **94**, 618
Bastien, P., Drissen, L., Menard, F., et al. 1988, *AJ*, **95**, 900
Bastien, P., Vernet, E., Drissen, L., et al. 2007, in *The Future of Photometric, Spectrophotometric and Polarimetric Standardization*, ed. C. Sterken, *ASP Conf. Ser.*, **364**, 529
Bazzon, A., Gisler, D., Roelfsema, R., et al. 2012, in *Ground-based and Airborne Instrumentation for Astronomy IV*, *Proc. SPIE*, **8446**, 93
Bellini, A., Anderson, J., van der Marel, R. P., et al. 2014, *ApJ*, **797**, 115
Benisty, M., Stolker, T., Pohl, A., et al. 2017, *A&A*, **597**, A42
Beuzit, J.-L., Feldt, M., Dohlen, K., et al. 2008, in *Ground-based and Airborne Instrumentation for Astronomy II*, *Proc. SPIE*, **7014**, 18
Bliokh, K. Y., & Aiello, A. 2013, *J. Opt.*, **15**, 014001
Boccaletti, A., Abe, L., Baudrand, J., et al. 2008, in *Adaptive Optics Systems*, *Proc. SPIE*, **7015**, 70151B
Bonnefoy, M., Zurlo, A., Baudino, J. L., et al. 2016, *A&A*, **587**, A58
Born, M., & Wolf, E. 1999, in *Principles of Optics* (Cambridge: Cambridge University Press)
Brandner, W., & Hormuth, F. 2016, in *Astronomy at High Angular Resolution*, eds. H. M. J. Boffin, G. Hussain, J.-P. Berger, & L. Schmidtobreich, *Astrophysics and Space Science Library*, **439**, 1
Breckinridge, J. B., Lam, W. S. T., & Chipman, R. A. 2015, *PASP*, **127**, 445
Cheetham, A. C., Girard, J., Lacour, S., et al. 2016, in *Optical and Infrared Interferometry and Imaging V*, *Proc. SPIE*, **9907**, 99072T
Clarke, D., Stewart, B. G., Schwarz, H. E., & Brooks, A. 1983, *A&A*, **126**, 260
Claudi, R. U., Turatto, M., Gratton, R. G., et al. 2008, in *Ground-based and Airborne Instrumentation for Astronomy II*, *Proc. SPIE*, **7014**, 70143E
Close, L. M. 2016, in *Adaptive Optics Systems V*, *Proc. SPIE*, **9909**, 99091E
Close, L. M., Males, J. R., Morzinski, K., et al. 2013, *ApJ*, **774**, 94
Collett, E. 1992, *Polarized Light: Fundamentals and Applications* (New York: Dekker)
Cox, L. J. 1976, *MNRAS*, **176**, 525
Davies, R., & Kasper, M. 2012, *ARA&A*, **50**, 305
de Juan Ovelar, M., Diamantopoulou, S., Roelfsema, R., et al. 2012, in *Modeling, Systems Engineering, and Project Management for Astronomy V*, *Proc. SPIE*, **8449**, 844912
de Zeeuw, T. 2016, *The Messenger*, **166**, 2
Dixon, W. V. D., Davidsen, A. F., & Ferguson, H. C. 1995, *ApJ*, **454**, L47
Dohlen, K., Langlois, M., Saisse, M., et al. 2008, in *Ground-based and Airborne Instrumentation for Astronomy II*, *Proc. SPIE*, **7014**, 70143L
Dohlen, K., Vigan, A., Mouillet, D., et al. 2016, in *Ground-based and Airborne Instrumentation for Astronomy VI*, *Proc. SPIE*, **9908**, 99083D
Engler, N., Schmid, H. M., Thalmann, C., et al. 2017, *A&A*, **607**, A90
Ferreira, J., Dougados, C., & Cabrit, S. 2006, *A&A*, **453**, 785
Frank, A., Ray, T. P., Cabrit, S., et al. 2014, *Protostars Planets VI*, 451
Fusco, T., Sauvage, J.-F., Petit, C., et al. 2014, in *Adaptive Optics Systems IV*, *Proc. SPIE*, **9148**, 1
Fusco, T., Sauvage, J.-F., Mouillet, D., et al. 2016, in *Adaptive Optics Systems V*, *Proc. SPIE*, **9909**, 99090U
Gandorfer, A. M. 1999, *Opt. Eng.*, **38**, 1402
Gandorfer, A. M., & Povel, H. P. 1997, *A&A*, **328**, 381
Garufi, A., Quanz, S. P., Schmid, H. M., et al. 2016, *A&A*, **588**, A8
Gisler, D., Feller, A., & Gandorfer, A. M. 2003, in *Polarimetry in Astronomy*, *Proc. SPIE*, **4843**, 45
Gisler, D., Schmid, H. M., Thalmann, C., et al. 2004, in *Ground-based Instrumentation for Astronomy*, *Proc. SPIE*, **5492**, 463
Goos, F., & Hänchen, H. 1947, *Annal. Phys.*, **436**, 333
Haniff, C. A., Scholz, M., & Tuthill, P. G. 1995, *MNRAS*, **276**, 640
Höfner, S. 2008, *A&A*, **491**, L1
Höfner, S., Bladh, S., Aringer, B., & Ahuja, R. 2016, *A&A*, **594**, A108
Hsu, J.-C., & Breger, M. 1982, *ApJ*, **262**, 732
Ireland, M. J., Tuthill, P. G., Davis, J., & Tango, W. 2005, *MNRAS*, **361**, 337
Janson, M., Durkan, S., Bonnefoy, M., et al. 2018, *A&A*, submitted
Joos, F. 2007, PhD Thesis, ETH Zurich
Joshi, U. C., Ganesh, S., & Baliyan, K. S. 2012, in *Stellar Polarimetry: from Birth to Death*, *AIP Conference Proceedings*, **1429**, 222
Jovanovic, N., Martinache, F., Guyon, O., et al. 2015, *PASP*, **127**, 890
Kasper, M., Beuzit, J.-L., Feldt, M., et al. 2012, *The Messenger*, **149**, 17
Kasper, M., Kasper, M., & Mawet, D. 2013, in *Proceedings of the Third AO4ELT Conference*, **8**
Keller, C. U., Schmid, H. M., Venema, L. B., et al. 2010, in *Ground-based and Airborne Instrumentation for Astronomy III*, *Proc. SPIE*, **7735**, 77356G
Kemp, J. C., & Barbour, M. S. 1981, *PASP*, **93**, 521

- Kervella, P., Domiciano de Souza, A., & Bendjoya, P. 2008, *A&A*, **484**, L13
- Kervella, P., Montargès, M., Lagadec, E., et al. 2015, *A&A*, **578**, A77
- Kervella, P., Lagadec, E., Montargès, M., et al. 2016, *A&A*, **585**, A28
- Khouri, T., Maercker, M., Waters, L. B. F. M., et al. 2016, *A&A*, **591**, A70
- Kuhn, J. R., Potter, D., & Parise, B. 2001, *ApJ*, **553**, L189
- Lafrenière, D., Marois, C., Doyon, R., Nadeau, D., & Artigau, É. 2007, *ApJ*, **660**, 770
- Langlois, M., Dohlen, K., Vigan, A., et al. 2014, in Ground-based and Airborne Instrumentation for Astronomy V, *Proc. SPIE*, **9147**, 91471R
- Law, N. M., Mackay, C. D., Dekany, R. G., et al. 2009, *ApJ*, **692**, 924
- Liimets, T., Corradi, R. L. M., Jones, D., et al. 2018, *A&A*, **612**, A118
- Lovis, C., Snellen, I., Mouillet, D., et al. 2017, *A&A*, **599**, A16
- Macintosh, B., Graham, J. R., Ingraham, P., et al. 2014, *Proc. Nat. Acad. Sci.*, **111**, 12661
- Maire, A.-L., Bonnefoy, M., Ginski, C., et al. 2016a, *A&A*, **587**, A56
- Maire, A.-L., Langlois, M., Dohlen, K., et al. 2016b, in Ground-based and Airborne Instrumentation for Astronomy VI, *Proc. SPIE*, **9908**, 990834
- Malbet, F. 1996, *A&AS*, **115**, 161
- Marchis, F., Kaasalainen, M., Hom, E. F. Y., et al. 2006, *Icarus*, **185**, 39
- Marois, C., Lafrenière, D., Doyon, R., Macintosh, B., & Nadeau, D. 2006, *ApJ*, **641**, 556
- Martinez Pillet, V., & Sanchez Almeida, J. 1991, *A&A*, **252**, 861
- McLaughlin, D. E., Anderson, J., Meylan, G., et al. 2006, *ApJS*, **166**, 249
- Melnikov, S., Stute, M., & Eisloffel, J. 2018, *A&A*, **612**, A77
- Milli, J., Mouillet, D., Mawet, D., et al. 2013, *A&A*, **556**, A64
- Milli, J., Mouillet, D., Fusco, T., et al. 2017, *Adapt. Opt. Extremely Large Tel.*, DOI 10.26698/AO4ELT5.0034
- Momany, Y., Saviane, I., Smette, A., et al. 2012, *A&A*, **537**, A2
- Muto, T., Grady, C. A., Hashimoto, J., et al. 2012, *ApJ*, **748**, L22
- Norris, B. R. M., Tuthill, P. G., Ireland, M. J., et al. 2012, *Nature*, **484**, 220
- Ohnaka, K., Weigelt, G., & Hofmann, K.-H. 2017a, *A&A*, **597**, A20
- Ohnaka, K., Weigelt, G., & Hofmann, K.-H. 2017b, *Nature*, **548**, 310
- Paladini, C., Klotz, D., Sacuto, S., et al. 2017, *A&A*, **600**, A136
- Patapis, P., Kühn, J., & Schmid, H. M. 2018, in Advances in Optical and Mechanical Technologies for Telescopes and Instrumentation III, *Proc. SPIE*, **10706**, 107065J
- Perrin, M. D., Schneider, G., Duchene, G., et al. 2009, *ApJ*, **707**, L132
- Perrin, M. D., Duchene, G., Millar-Blanchaer, M., et al. 2015, *ApJ*, **799**, 182
- Povel, H.-P. 1995, *Opt. Eng.*, **34**, 1870
- Povel, H., Aebersold, H., & Stenflo, J. O. 1990, *Appl. Opt.*, **29**, 1186
- Pragt, J., Roelfsema, R., Gisler, D., et al. 2012, in Ground-based and Airborne Instrumentation for Astronomy IV, *Proc. SPIE*, **8446**, 844697
- Quanz, S. P., Schmid, H. M., Geissler, K., et al. 2011, *ApJ*, **738**, 23
- Ragland, S., Le Coroller, H., Pluzhnik, E., et al. 2008, *ApJ*, **679**, 746
- Rapson, V. A., Kastner, J. H., Millar-Blanchaer, M. A., & Dong, R. 2015, *ApJ*, **815**, L26
- Riaud, P., Boccaletti, A., Baudrand, J., & Rouan, D. 2003, *PASP*, **115**, 712
- Roelfsema, R., Schmid, H. M., Pragt, J., et al. 2010, in Ground-based and Airborne Instrumentation for Astronomy III, *Proc. SPIE*, **7735**, 4
- Roelfsema, R., Gisler, D., Pragt, J., et al. 2011, in Techniques and Instrumentation for Detection of Exoplanets V, *Proc. SPIE*, **8151**, 81510N
- Roelfsema, R., Bazzon, A., Schmid, H. M., et al. 2014, in Ground-based and Airborne Instrumentation for Astronomy V, *Proc. SPIE*, **9147**, 91473W
- Roelfsema, R., Bazzon, A., Schmid, H. M., et al. 2016, in Adaptive Optics Systems V, *Proc. SPIE*, **9909**, 990927
- Rouan, D., Riaud, P., Boccaletti, A., Clénet, Y., & Labeyrie, A. 2000, *PASP*, **112**, 1479
- Sauvage, J.-F., Fusco, T., Rousset, G., & Petit, C. 2007, *J. Opt. Soc. Am. A*, **24**, 2334
- Sauvage, J.-F., Fusco, T., Lamb, M., et al. 2016a, in Adaptive Optics Systems V, *Proc. SPIE*, **9909**, 990916
- Sauvage, J.-F., Fusco, T., Petit, C., et al. 2016b, *J. Astron. Tel., Instrum. Syst.*, **2**, 025003
- Scarrott, S. M., Warren-Smith, R. F., Pallister, W. S., Axon, D. J., & Bingham, R. G. 1983, *MNRAS*, **204**, 1163
- Schiavon, R. P., Dalessandro, E., Sohn, S. T., et al. 2012, *AJ*, **143**, 121
- Schmid, H. M., Beuzit, J.-L., Feldt, M., et al. 2006a, in Direct Imaging of Exoplanets: Science & Techniques, eds. C. Aime, & F. Vakili, *IAU Colloq.*, **200**, 165
- Schmid, H. M., Joos, F., & Tschan, D. 2006b, *A&A*, **452**, 657
- Schmid, H.-M., Downing, M., Roelfsema, R., et al. 2012, in Ground-based and Airborne Instrumentation for Astronomy IV, *Proc. SPIE*, **8446**, 8
- Schmid, H. M., Bazzon, A., Milli, J., et al. 2017, *A&A*, **602**, A53
- Schneider, G., & Silverstone, M. D. 2003, in High-Contrast Imaging for Exoplanet Detection, eds. A. B. Schultz, *Proc. SPIE*, **4860**, 1
- Serkowski, K. 1974, in Planets, Stars, and Nebulae: Studied with Photopolarimetry, ed. T. Gehrels, *IAU Colloq.*, **23**, 135
- Serkowski, K., & Shawl, S. J. 2001, *AJ*, **122**, 2017
- Serkowski, K., Mathewson, D. S., & Ford, V. L. 1975, *ApJ*, **196**, 261
- Sivaramakrishnan, A., Koresko, C. D., Makidon, R. B., Berkefeld, T., & Kuchner, M. J. 2001, *ApJ*, **552**, 397
- Soummer, R., Pueyo, L., & Larkin, J. 2012, *ApJ*, **755**, L28
- Stenflo, J. O. 1996, *Nature*, **382**, 588
- Stenflo, J. O., & Keller, C. U. 1997, *A&A*, **321**, 927
- Stolker, T., Dominik, C., Avenhaus, H., et al. 2016, *A&A*, **595**, A113
- Thalmann, C., Schmid, H. M., Boccaletti, A., et al. 2008, in Ground-based and Airborne Instrumentation for Astronomy II, *Proc. SPIE*, **7014**, 3
- Thalmann, C., Mulders, G. D., Janson, M., et al. 2015, *ApJ*, **808**, L41
- Tinbergen, J. 1979, *A&AS*, **35**, 325
- Tinbergen, J. 2007, *PASP*, **119**, 1371
- van Belle, G. T., Dyck, H. M., Benson, J. A., & Lacasse, M. G. 1996, *AJ*, **112**, 2147
- van Boekel, R., Henning, T., Menu, J., et al. 2017, *ApJ*, **837**, 132
- van Holstein, R. G., Snik, F., Girard, J. H., et al. 2010, in Techniques and Instrumentation for Detection of Exoplanets VIII, *Proc. SPIE*, **10400**, 1040015
- Vernazza, P., Marchis, F., Carry, B., Marsset, M., & Hanus, J. 2008, in *European Planetary Science Congress (EPSC2017)*, 11
- Vigan, A., Langlois, M., Dohlen, K., et al. 2014, in Ground-based and Airborne Instrumentation for Astronomy V, *Proc. SPIE*, **9147**, 91474T
- Vigan, A., Bonnefoy, M., Ginski, C., et al. 2016, *A&A*, **587**, A55
- Whittet, D. C. B., Martin, P. G., Hough, J. H., et al. 1992, *ApJ*, **386**, 562
- Wildi, F., Mouillet, D., Beuzit, J.-L., et al. 2009, in Techniques and Instrumentation for Detection of Exoplanets IV, *Proc. SPIE*, **7440**, 74400Q
- Wildi, F. P., Michaud, B., Crausaz, M., et al. 2010, in Ground-based and Airborne Instrumentation for Astronomy III, *Proc. SPIE*, **7735**, 77352V
- Zurlo, A., Vigan, A., Galicher, R., et al. 2016, *A&A*, **587**, A57

- ¹ ETH Zurich, Institute for Particle Physics and Astrophysics, Wolfgang-Pauli-Strasse 27, 8093 Zurich, Switzerland
- ² NOVA Optical Infrared Instrumentation Group at ASTRON, Oude Hoogeveensedijk 4, 7991 PD Dwingeloo, The Netherlands
- ³ Université Grenoble Alpes, IPAG, 38000 Grenoble, France
- ⁴ CNRS, IPAG, 38000 Grenoble, France
- ⁵ European Southern Observatory, Alonso de Cordova 3107, Casilla 19001 Vitacura, Santiago 19, Chile
- ⁶ Istituto Ricerche Solari Locarno, Via Patocchi 57, 6605 Locarno Monti, Switzerland
- ⁷ Kiopenheuer-Institut für Sonnenphysik, Schneckstr. 6, 79104 Freiburg, Germany
- ⁸ Anton Pannekoek Astronomical Institute, University of Amsterdam, PO Box 94249, 1090 GE Amsterdam, The Netherlands
- ⁹ LESIA, CNRS, Observatoire de Paris, Université Paris Diderot, UPMC, 5 place J. Janssen, 92190 Meudon, France
- ¹⁰ Leiden Observatory, Leiden University, PO Box 9513, 2300 RA Leiden, The Netherlands
- ¹¹ Laboratoire Lagrange, UMR7293, Université de Nice Sophia-Antipolis, CNRS, Observatoire de la Côte d'Azur, Boulevard de l'Observatoire, 06304 Nice, Cedex 4, France
- ¹² INAF – Osservatorio Astronomico di Roma, via Frascati 33, 00087 Monte Porzio Catone, Italy
- ¹³ Max-Planck-Institut für Astronomie, Königstuhl 17, 69117 Heidelberg, Germany
- ¹⁴ INAF – Osservatorio Astronomico di Padova, Vicolo dell'Osservatorio 5, 35122 Padova, Italy
- ¹⁵ Aix Marseille Université, CNRS, CNES, LAM (Laboratoire d'Astrophysique de Marseille) UMR 7326, 13388 Marseille, France
- ¹⁶ Unidad Mixta Internacional Franco-Chilena de Astronomia, CNRS/INSU UMI 3386 and Departamento de Astronomia, Universidad de Chile, Casilla 36-D, Santiago, Chile
- ¹⁷ European Southern Observatory, Karl Schwarzschild St, 2, 85748 Garching, Germany
- ¹⁸ ONERA, The French Aerospace Lab BP72, 29 avenue de la Division Leclerc, 92322 Châtillon Cedex, France
- ¹⁹ Centre de Recherche Astrophysique de Lyon, CNRS/ENSL Université Lyon 1, 9 av. Ch. André, 69561 Saint-Genis-Laval, France
- ²⁰ INAF – Osservatorio Astrofisico di Arcetri, Largo E. Fermi 5, 50125 Firenze, Italy
- ²¹ Geneva Observatory, University of Geneva, Chemin des Maillettes 51, 1290 Versoix, Switzerland